Advanced Drug Delivery Reviews 192 (2023) 114621

Contents lists available at ScienceDirect

Advanced Drug Delivery Reviews

journal homepage: www.elsevier.com/locate/adr

Image-guided drug delivery in nanosystem-based cancer therapies

Marjolein I. Priester [a,b], Timo L.M. ten Hagen [a,c,*]

[a] Precision Medicine in Oncology (PrMiO), Department of Pathology, Erasmus MC Cancer Institute, Erasmus MC, Rotterdam, The Netherlands
[b] Department of Radiotherapy, Erasmus MC Cancer Institute, Erasmus MC, Rotterdam, The Netherlands
[c] Nanomedicine Innovation Center Erasmus (NICE), Erasmus MC, Rotterdam, The Netherlands

ARTICLE INFO

Article history:
Received 19 July 2022
Revised 18 October 2022
Accepted 13 November 2022
Available online 17 November 2022

Keywords:
Cancer
Drug delivery
Imaging
Nanomedicine
Theranostics

ABSTRACT

The past decades have shown significant advancements in the development of solid tumor treatment. For instance, implementation of nanosystems for drug delivery has led to a reduction in side effects and improved delivery to the tumor region. However, clinical translation has faced challenges, as tumor drug levels are still considered to be inadequate. Interdisciplinary research has resulted in the development of more advanced drug delivery systems. These are coined "smart" due to the ability to be followed and actively manipulated in order to have better control over local drug release. Therefore, image-guided drug delivery can be a powerful strategy to improve drug activity at the target site. Being able to visualize the inflow of the administered smart nanosystem within the tumor gives the potential to determine the right moment to apply the facilitator to initiate drug release. Here we provide an overview of available nanosystems, imaging moieties, and imaging techniques. We discuss preclinical application of these smart drug delivery systems, the strength of image-guided drug delivery, and the future of personalized treatment.

Contents

---

[*] Corresponding author at: Department of Pathology, Erasmus MC, Rotterdam, The Netherlands.
E-mail address: t.l.m.tenhagen@erasmusmc.nl (T.L.M. ten Hagen).

https://doi.org/10.1016/j.addr.2022.114621
0169-409X/

1. Introduction

Drug delivery in tumors is hampered by a number of factors, which are related to drug type, drug administration procedure, tumor type and -pathophysiology, patient health condition, and treatment conditions [1]. A dominant aspect in failure of chemotherapy, next to (acquired) drug resistance, is insufficient drug levels at the target site. Also, systemic administration of chemotherapeutics is associated with severe toxicities. The dose-limiting nature of these side effects precludes administration of higher doses per time point and also halts continuation of treatment. In case of disease recurrence, retreatment is often not an option. This is not only due to acquired drug resistance, but also owing to side effects and damage done to healthy tissues. Therefore, it is crucial to i) improve drug delivery to the tumor microenvironment, ii) enable intra-tumoral accumulation of the active drug, and iii) minimize exposure to sensitive tissues. Manners to improve drug delivery are (nano) formulations, loco-regional delivery, co-administration, or application of facilitators.

In this paper, we review in particular the use of imaging as a means to improve drug delivery by increasing availability of the active compound at the target, i.e. in the tumor cells. In such setting, imaging could be used to steer the therapeutic nanoparticle to the tumor or to guide an external trigger, a facilitator, to induce the nanoparticles to release their cargo. In this review, we refer to facilitators as agents or treatments that improve delivery of the chemotherapeutic, and not per se ways to improve activity of the drug. Currently, a plethora of imaging methods are available to monitor drug pharmacokinetics, biodistribution, and drug accumulation at the target site in real-time as we discuss below. These imaging methods are used with the idea to improve treatment outcome, which is often coined as image-guided drug delivery. However, the true meaning of image-guided drug delivery (IGDD) needs to be defined properly to match the true setting and intend.

Here, we will focus on (pre)clinical studies on image-guided drug delivery employing nanomedicine for oncological treatment. The selection is limited to the eight most reported nanocarriers as reported by Hossen et al: i) dendrimers, ii) micelles, iii) liposomes, iv) carbon nanotubes, v) superparamagnetic iron oxide nanoparticles, vi) gold nanoparticles, vii) mesoporous silica nanoparticles, and viii) quantum dots [2]. Therefore, other structures used for drug delivery, such as nanobubbles [3], labelled small molecules [4], proteins [5], RNA [6], oligonucleotides [7], and antibodies [8], were not considered in this review.

2. Definitions

2.1. Image-guided drug delivery

The definition of image-guided drug delivery needs attention, as throughout the literature this is interpreted differently. Numerous publications refer to IGDD as a combination of drug targeting, either active or passive, and imaging. In these instances imaging is used to observe accumulation at the target site during and after treatment. While information is obtained on, for instance, local drug delivery levels and therefore possible outcome, imaging is not used to directly manipulate drug delivery. On the other hand, we and others use imaging in IGDD as a manner to actively improve local accumulation of chemotherapeutics, or induce bioavailability of the nanoparticle associated compound, by combining imaging of the drug or carrier with a procedure that is intended to promote local drug build-up. In such settings, imaging helps to orchestrate a combination of observations; first, determination of the right moment (e.g. when maximum level of drug accumulation can be reached), and second, application of the facilitating treatment with the intend to improve tumor drug levels in a spatiotemporal controlled way. In this setting, imaging is used to actively manipulate drug delivery - and is not used solely to passively monitor the kinetics of the drug - and as such can be truly classified as image-guided drug delivery.

It is important to highlight that IGDD can either be at tissue level, i.e. intended to improve accumulation of the active compound in the tumor micro-environment (TME), or at a cellular level. The latter could also be referred to as Image Guided Drug Release (IGDR) when for instance forcing intracellular dissociation of a drug from the nanocarrier, thus facilitating the possibility of drug interaction with the intracellular target. For instance, He et al. designed a hybrid nanosystem based on a gold nanocage (AuNC) containing doxorubicin (DOX), which is made smart with the use of a thermosensitive liposome-based coating [9]. Therefore, this Lipos-AuNC-DOX complex will respond to the application of mild hyperthermia at 41 °C. Triggered release was induced 24 h after intravenous (i.v.) injection to release encapsulated doxorubicin from the nanoparticles. In this case, it is important to understand that at that specific time point these nanoparticles have been circulating throughout the entire body and have already been taken up by tumor cells. The subsequent application of near-infrared light (NIR) to induce heat and trigger release facilitates the transfer of doxorubicin from the lysosomes to the nucleus, excellently demonstrating the benefit of this approach. This strategy, while it cannot be considered to be true image-guided drug delivery, is a perfect example of image-guided drug release.

In a similar manner, Li et al. targeted tumor cells with AS1411 aptamer-decorated DNA gold nanoparticles [10]. Through a distinct pathway, the conjugated gold nanostars interact with flap endonuclease 1 (FEN1), resulting in fluorescent signals. The detection of these signals is the cue to initiate doxorubicin release through NIR laser irradiation. As FEN1 is overexpressed in tumors, the nanosystems presented here can be used for both diagnosis and IGDR.

2.2. Nanosystem formulations

Nanosystems (or nanocarriers) are structures with a diameter within one to several hundred nanometers, which can be used for drug delivery and diagnostic purposes. Encapsulation of therapeutics or other agents within a nanosystem ensures an improved efficacy due to i) a decrease in the volume of distribution, ii) prolonged circulation and/or retention at the target site, iii) synergy between co-encapsulated compounds, or iv) interaction with specific conditions or activities within the tumor-micro environment [11].

It is evident that encapsulation of a compound within a nanosystem has a tremendous impact on compound pharmacokinetics and biodistribution. Not only does this improve stability of the associated compound in systemic circulation by preventing degradation, but also the likelihood that both compound and nanosystem will end up together at the target site. Undoubtedly, the stability of the nanoparticle as well as the nanoparticle elements within the formulation, i.e. building blocks, needs to be considered. The aspect of delivery of content to the target site with a stable nanosystem also benefits co-delivery of compounds or combination treatment. The use of a stable formulation does not only guarantee synergy, as it ensures delivery of multiple agents at the same site at the same time, co-formulation also enables more precise creation of the optimal drug ratio and dosage for maximum therapeutic effect.

Lastly, nanosystems can facilitate delivery of different compounds at the same time, of which one has a direct activity and the other can be activated at the target site through an external trigger. When through imaging the delivery of the nanosystem or compound can be monitored, the facilitator as well as another external trigger can be applied at the right moment. An example is for instance the combination of a nanosystem carrying both a chemotherapeutic drug that is released by NIR radiation, through so-called photothermal therapy (PTT), while at the same time photodynamic therapy (PDT) is conducted. It can be envisioned that causing intratumoral heat, while causing a local rise in available chemotherapeutic combined with induction of oxygen radicals, could provide an excellent synergistic anti-tumor effect as we will describe below. For all these functionalities, the possibility to follow, track, steer, trigger, activate, or manipulate are desirable to optimize drug availability and activity, which underscores the importance of IGDD. Important is that to obtain these functionalities, a vast number of nanosystems are studied. Taken together, the plethora of conventional nanocarriers available are able to encapsulate a range of moieties. However, administration leads to non-specific biodistribution and uncontrollable drug release. Further modification and functionalization of nanosystems as we discuss here results in so-called smart drug delivery systems (SDDS).

2.3. Smart drug delivery systems

While "smart" can be considered an arbitrary term, it has frequently been used in literature regarding development of novel cancer treatments. We, as published before, see SDDS as advanced nanoparticles which can be controlled to alter their release behavior [8,11]. For instance, SDDS can be designed to be sensitive to tumor-specific characteristics, such as presence of an acidic pH, enzymes, or hypoxia. Exogeneous triggers may be based on exposure of the target tissue to physical stimuli, such as light, ultrasound, electromagnetic waves, or mild hyperthermia. While both strategies are suitable to exploit the TME for triggered drug release, exogenous triggers tend to achieve a more precise and controlled release, as endogenous triggers may also be present in healthy tissues due to diminutive differences in tissue characteristics [11,12]. More so, external triggers can be used to actually determine when in tissue drugs are released or activated. Additionally, drug activation or release from nanosystems by intrinsic triggers tend to exhibit slow kinetics typically taking hours to days, while responses to external triggers may take place in seconds. Besides stimuli responsiveness, another 'smart' feature of these nanosystems is the ability to make these formulations multifunctional. In addition to the intrinsic characteristics of the nanosystems, SDDS can be endlessly manipulated and optimized due to the possibility to i) encapsulate multiple agents and ii) improve active tumor targeting by surface decoration with tumor specific moieties [8]. For smart drug delivery systems, a distinction can be made between organic, inorganic, and hybrid nanosystems, which will be discussed in section 4.

3. Imaging moieties

Imaging moieties are used in both research and clinical studies to visualize and quantify drug delivery in real-time. These exogeneous substances are able to temporarily enhance visualization to illustrate morphologies, internal structures, and physiological functions [13]. To improve delivery and monitoring, a distinction can be made between nanomaterials with intrinsic visualization properties and imaging agents, such as labels and probes (Table 2). In this section, we will primarily focus on agents that can be labeled to, or loaded in, nanosystems.

Imaging moieties can be encapsulated either solo or as co-entrapment within a nanosystem. While some agents have a sole imaging function, others are considered to be multifunctional and can be simultaneously used for triggered drug release, for instance as a photothermal (PT)- or photosensitizing (PS) agent [14,15]. In this section, various imaging moieties are discussed, being either categorized as contrast agents or radionuclides.

3.1. Contrast agents

Contrast agents (CAs) can be administered to enhance visualization by increasing the sensitivity and specificity between healthy and malignant tissue. As solid tumors present an abnormal vascular network, which exhibits increased permeability in combination with a lack of functional lymphatic drainage, accumulation of CAs may be enhanced and retention may occur for longer periods of time in comparison to healthy tissue [11,16]. With respect to image-guided drug delivery, contrast agents are used to visualize the delivery system and/or content release and could as such be used to determine nanosystem location, -retention, and drug delivery efficiency [17]. CAs can be distinguished based on the corresponding imaging modality: either optical contrast agents, such as endogenous agents and fluorescent dyes, or other CAs based on metals and heavy elements for MR or CT imaging.

3.1.1. Optical contrast agents

Fluorescence-guided drug delivery at (sub)cellular level can be provided using dyes, proteins, and autofluorescent agents (Table 2) [18]. In general, fluorescent molecules are bright, photostable, and biodegradable [18]. As the available fluorophores emit in a wide spectral range, from ultraviolet to infrared, agents can be selected depending on several factors such as target tissue and imaging method.

Fluorescent dyes produce brief, non-specific contrast suitable for in vivo real-time visualization [19]. For instance, the fluorescent agent carboxyfluorescein (CF) can be used as a model drug to monitor release from nanosystems. In contrast to legitimate drugs, CF displays no cellular uptake, which avoids changes in fluorescence due to interactions with intracellular components [1]. While some fluorescent dyes are immediately detectable after excitation, others emit no fluorescence in its native state. For instance, 5-aminolevulinic acid (5-ALA) requires metabolic processing into protoporphyrin IX, while nanosystem encapsulation of agents such as CF and Calcein induces self-quenching, which will be reversed after release into the micro-environment [12,19].

Compared to traditional fluorescent dyes, near infrared fluorophores display enhanced optical properties. Falling within a specific window (λ = 700 – 3000 nm), NIR dyes provide improved use due to a deeper penetration depth of the excitation light, high spatial precision of detection, and minimized background interference of emission signal [20,21]. Cyanine-based fluorescent dyes, such as ICG, Cy5.5, and IR780, are widely applied as diagnostic agents [20,22,23]. Indocyanine green (ICG), a dye with Food and Drug Administration (FDA) approval, is frequently used in both experimental and clinical studies. Administration of free ICG exhibits low toxicity and low tissue autofluorescence. Moreover, irradiation of ICG with NIR laser light can effectively generate heat to such extend that direct tissue damage can be obtained. However, ICG displays several disadvantages in tumor theranostics, such as short half-life, poor photostability, and limited tumor-targeting due to albumin binding [19,24]. In comparison to ICG, IR780 exhibits higher fluorescence intensity and improved stability. In addition, it also shows enhanced tumor targeting due to intrinsic specificity for certain tumor cells [21,22].

Besides fluorescent dyes, fluorescent protein are also utilized for imaging purposes (Table 2). A distinction can be made between endogenous- and exogenous sources. In preclinical studies, endogenous sources are established via three strategies: i) transgenic models expressing fluorescent reporters, ii) orthotopic implantation of fluorescent cells, or iii) targeted gene delivery [18]. In the experimental setting, transgenic mouse strains, for instance with cell- or protein-specific fluorescent labels, can be employed for image-guided drug delivery. We for instance used transgenic mice for visualization of the vascular bed, while also tumor cells can be imaged [25,26]. The relatively poor penetration of light limits the use of fluorescence to superficial observations, or requires surgical intervention to expose the region of interest. Bioluminescence provides a better signal-to-noise ratio and excitation is not needed, therefore allowing for deep-tissue imaging [27]. Visualization of tumor blood flow and extravasation can also be established via administration of exogenous agents, such as fluorescently-labeled dextrans, FITC-BSA, heparin, or Hoechst [28,29]. In order to further improve sensitivity and photostability, fluorescent proteins can either be covalently attached to a polymer or encapsulated within a nanosystem [30].

The increased interest in fluorescence imaging for diagnosis and treatment can also be attributed to the field of image-guided surgery [31]. Comparable advantages and limitations are apparent for image-guided drug delivery and image-guided surgery. For instance, it is important to consider that tissues contain a multitude of naturally present fluorophores, which could potentially interfere as background autofluorescence during optical visualization. This is especially relevant when excite fluorescence within the visible light spectrum (λ = 380 – 650 nm) [23]. Dominant absorbers such as melanin, keratin, hemoglobin, and lipids may restrict the precision of biological imaging [32,33]. Strategies to reduce background autofluorescence could be hair removal [25], the use of a special chow diet [34], or a shift of targeting to towards the near-infrared (NIR) range (λ = 750 – 3000 nm). More specific, the tissue transparency window (NIR-I, λ = 650 – 950 nm) displays excellent penetration due to weak absorption by both water and tissue within this range [35].

Autofluorescence can also be advantageous for image-guided drug delivery. For instance, anthracycline drugs such as doxorubicin can simultaneously act as a therapeutic agent and a fluorescent probe [36]. Therefore, the intrinsic fluorescence of DOX can be used to visualize drug release and -uptake in the tumor micro-environment [37,38]. Another elegant auto fluorescent chemotherapeutic is topotecan (Hycamtin®). This drug only exhibits its intrinsic fluorescence in presence of a shift in environmental pH. Therefore, an increase in fluorescence can be observed when the agent transfers from the encapsulated (pH $\sim$ 6.5, λ = 3 85 nm) to a released state (pH greater than 7.5, λ = 414 nm) [39].

Photoacoustic (PA) contrast agents can be based on both endogenous- and exogenous optical absorbers (Table 2) [40]. Innate chromophores present in human tissue, such as hemoglobin, lipid, melanin, and water, exhibit strong optical absorption at certain wavelength [40,41]. The biomolecule melanin is widely distributed throughout the body, resulting in high biocompatibility, -degradability, and -stability [42]. Incorporation of synthetic melanin analogues, such as polydopamine (PDA), into nanosystems leads to improved contrast enhancement [43,44]. However, in order to improve differentiation between endogenous absorbers, exogenous contrast agents can be administered. The strong near-infrared absorbance properties of organic dyes, such as indocyanine green and methylene blue (MB), are suitable agents for photoacoustic imaging [41].

3.1.2. Other contrast agents

Magnetic resonance imaging (MRI) contrast agents, such as transition- or lanthanide metal ions, can be categorized into T_1-weighted or T_2-weighted CAs (Table 2) [45]. The distinction is based on shortening of the longitudinal (T_1)- or the transverse (T_2) relaxation time. Therefore, administration of T_1-weighted contrast agents displays positive contrast enhancement, which results in brighter images. And, T_2-weighted CAs show negative contrast enhancement, which results in darker images [45,46]. Gadolinium (Gd)-based chelates are most frequently used for MR imaging. For instance Magnevist®, a clinical contrast agent, is metabolically inert as a metal chelate. Therefore it shows no biological interactions, but is able to induce T_1-weighted contrast enhancement. However, a relatively short circulation time and side effects, such as nephrotoxicity and deposition, have led to development of safer CA alternatives [16,46].

Computed Tomography (CT) contrast agents, also known as radiopaque elements, enhance imaging based on X-ray attenuation (Table 2) [47]. The X-ray attenuation coefficient (μ) is influenced by elemental parameters, such as atomic number (Z) and density (ρ). The majority of the CT CAs are based on heavy elements, such as iodine, bismuth, and gold [13,48]. The halogen iodine ($Z_I = 53$, $\rho_I = 4.93$ g/cm^3, $\mu_I = 1.94$ cm^2/g at 100 KeV,) and analogues, i.e. iopromide, iopamidol, iohexol, and iodixanol, are the most commonly administrated CT contrast agents [13]. However, iodine containing molecules have limited ability due to a short circulation time and low specificity [49,50]. The halogen bismuth (Bi) is a suitable alternative due its higher atomic number ($Z_{Bi} = 83$), density ($\rho_{Bi} = 9.75$ g/cm^3), and X-ray attenuation coefficient ($\mu_{Bi} = 5.74$ cm^2/g at 100 KeV) [47,51]. Bismuth agents do possess low in vivo toxicity, but like iodine, the circulation time is relatively short. Comparable to bismuth, the transition metal gold ($Z_{Au} = 79$) ($\rho_{Au} = 19.32$ g/cm^3) ($\mu_{Au} = 5.16$ cm^2/g at 100 KeV) presents improved CT contrast enhancement in comparison to iodine analogues [51]. These elements are considered to be multimodal contrast agents due to intrinsic contrast- and photothermal properties [51].

3.2. Radionuclides

Radionuclides can be used for nuclear imaging techniques, such as single photon emission computed tomography (SPECT) or positron emission tomography (PET) (Table 2). SPECT imaging is based on gamma-emitting radioisotopes, such as technetium-99 m (^{99m}TC, $t_{1/2} = 6.0$ h), indium-111 (^{111}In, $t_{1/2} = 2.8$ days), and rhenium-188 (^{188}Re, $t_{1/2} = 3.97$ h). PET imaging is dependent on positron-emitting radionuclides, such as fluorine-18 (^{18}F, $t_{1/2} = 110$ min), copper-64 (^{64}Cu, $t_{1/2} = 12.7$ h), and zirconium-89 (^{89}Zr, $t_{1/2} = 3.27$ days) [52,53].

Radionuclides are widely used in patients for diagnosis, radiotherapy, and a combination thereof. A vast number of nanomedicine formulations containing radiotracers have been synthesized and tested for biomedical use [54]. While the implementation of radionuclides has advantages over other imaging moieties, certain drawbacks need to be considered when formulating nanoparticles for use in patients. Upon systemic administration, detachment of radionuclides from the radiolabeled compound can occur due to instability, competition, or metabolic reactions [52]. Subsequent decay leads to formation of daughter nuclides, which can unwantedly be taken up by tissues and organs. In addition, emission from daughter nuclides may interfere with emission from the conjugated parent nuclide, resulting in misinterpretation of images [52]. Therefore, radiolabeled nanosystems present several benefits, such as improved sensitivity, enhanced contrast, and the ability to combine therapeutics with diagnostic agents [55]. The half-life of the selected radionuclide should match the nanosystems pharmacokinetics in order to ensure emission within the imaging window [56]. Opposed to fluorescent markers and contrast agents, radioisotopes can be detected with unlimited penetration depth. Therefore allowing for whole-body imaging in both experimental and clinical setting.

The shortcomings of administration of free contrast agents, such as limited circulation time and low tumor specificity, can be improved by encapsulation in nanosystems.

4. Nanosystems

In the past decades, a vast number of nanosystems have been developed or are currently under investigation. These systems vary in degree of complexity, from relatively straightforward nanoparticles carrying a single compound with little added functionality, to nanoparticles which enable imaging, steering, and manipulation while containing multiple compounds. It is important to realize that nanoparticles registered for clinical use mainly exhibit single and straightforward characteristics, while further development towards smart drug delivery systems is relatively slow [11].

While most nanosystems can be functionalized using various moieties, the intrinsic properties of a nanosystem are as important. More so, nanoparticles may have different functions, such as detection of a tumor, homing to a tumor, facilitation of imaging, and at the same time delivery of therapeutics. The use of nanoparticles that are equipped for both diagnosis as well as therapy is coined theranostics. Clearly, in this setting the possibility of IGDD is also desired. Various smart drug delivery systems have been designed to aid solid tumor theranostics. Nanosystems can generally be classified into three major types based on their composition, as these are made either from organic- or inorganic materials, or a combination of these two in a hybrid form.

4.1. Organic nanomaterials

Drug delivery systems composed of natural- or synthetic organic nanomaterials are interesting competitors in the field of cancer treatment. Based on biological molecules such as lipids or polymers, organic nanomaterials are considered to have a high biocompatibility and offer a wide range of possibilities. As weak non-covalent interactions between organic molecules initiate self-assembly, interference of synthetic chemistry provides the ability to personalize nanosystem design at multiple levels [57]. In this section, characteristics and functionalization of dendrimers, micelles, and liposomes will be discussed (Fig. 1).

4.1.1. Dendrimers

Dendrimers are radially symmetric, three-dimensional globular architectures with sizes ranging from 2 to 10 nm [58]. Their structure can be divided into three parts: a core, the branching dendrons, and the surface-active groups [2,48]. The size of the dendrimer is determined by the amount of so-called generations (G), the concentric shells of branching dendrons surrounding the core, which add approximately 0.7 to 1.5 nm in size per generation [59,60]. At G0 up to G3 the dendrimer is relatively small and retains the organic flexibility without great homogeneity. From the fourth generation (G4), dendrimers initiate their spherical shape, which will further develop to structured spheres at the fifth generation (G5). At that stage, it is impossible to branch out further due to a lack of space, which is dubbed the ‘starburst effect’ [58].

Various dendrimer types have been developed since the introduction by Vögtle et al. in 1978 [61]. These can be distinguished based on their synthesis method, physical structure, shape, physicochemical properties, and dendrimer chemistry [62]. Dendrimer synthesis follows either the divergent or the convergent approach [63]. Poly(amidoamine) (PAMAM) is the most common dendrimer scaffold studied for drug delivery, being hydrophilic, biocompatible, and non-immunogenic [64,65]. Other polymers frequently applied for dendrimer-based nanosystems are poly(propylene imine) (PPI) and Poly($_L$-lysine) (PLL)[63]. Although being biocom-

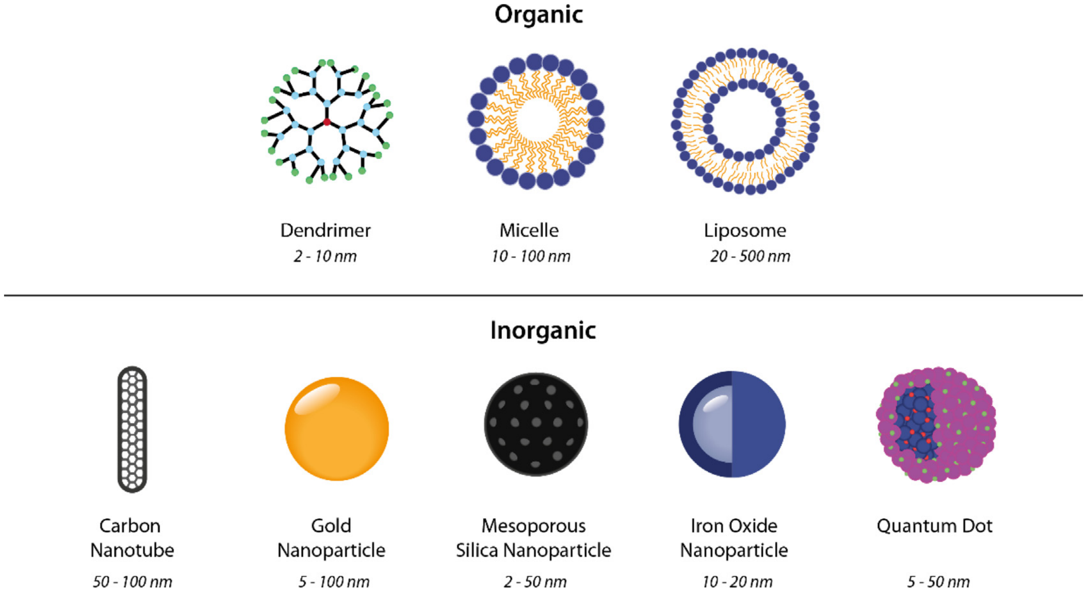

Fig. 1. Overview of the discussed nanosystems for image-guided drug delivery. A distinction can be made between organic- and inorganic nanosystems. The general size for each nanosystem is indicated.

patible, dendritic polymers such as PAMAM and PPI are non-biodegradable [65,66].

The generational architecture of a dendrimer creates a "void space", which can be used for encapsulation of a wide variety of substances based on hydrophobic- or electrostatic interactions [48,59]. The presence of a void space does not only accommodate a payload, but is also important to prevent enzymatic degradation, and is a feature to control drug release [48]. In addition, the dendrimer outer surface allows for functionalization with various ligands [48]. Surface modification of conventional dendrimers is essential, as this nanosystem is highly subjected to rapid clearance through the reticuloendothelial system (RES) and shows relatively low uptake by malignant cells [2]. Another important consideration for surface modification is the intrinsic toxicity of all dendrimer types, which is related to the core chemistry, the branched dendrimers, and the surface-active groups [65,67]. Moieties can be attached to the outer surface via covalent-, electrostatic- or hydrophobic binding [58]. While PEGylation is an effective strategy to reduce toxicity and to prolong circulation time, tumor-targeting properties can be enhanced by conjugation with tumor-specific elements such as antibodies, folic acid, or carbohydrates [65,67].

Surface engineering does not only contribute to biocompatibility and biodistribution of the dendrimer, but also enhances drug entrapment capacity and is able to facilitate imaging [67]. As dendritic polymers do not intrinsically exhibit any optical, acoustic, or magnetic signal, encapsulation of imaging moieties is indispensable [68]. Dendrimers are an excellent platform for moiety encapsulation owing to the architecture, as a large number of binding sites can be found both in the interior and periphery of the nanosystem. Dendrimers were applied early-on in vivo as a carrier for magnetic resonance imaging contrast agents [64,69].

The large number of binding sites, especially the primary amine functional groups on the outer surface, makes them an attractive platform for detaining MRI probes, such as paramagnetic ions or magnetic oxides [48,68,70]. In addition, dendrimer-based contrast agents showed increased longitudinal relaxation rates, which increased even further with a growing amount of generations present [48]. Despite the wide clinical application of gadolinium chelates, the search for safer alternatives has also influenced the development of novel dendrimer types. Functionalization of dendrimers with organic radicals, such as 2,2,5,5-tetramethylpyrrolidin-1-oxyl (PROXYL) units, results in high paramagnetic systems [62,71].

The dendrimer architecture is not limited to a single-generation structure. For instance, dendrimersomes (DSs) are a novel type of nanovesicles composed of multiple low-generation Janus dendrimers [72]. As these dendrimers are amphiphilic, this allows for self-assembly into spherical structures in the presence of an aqueous medium. The formation of dendrimersomes results in a structure with a similar size to high-generation dendrimers, but with the presence of an aqueous core similar to liposomes. This enables the delivery of a wide variety of theranostics, in combination with high stability, high mechanical strength, and increased biocompatibility [73].

Another possible dendrimer-based evolution are the core–shell tecto dendrimers (CSTDs), which are clusters composed of high-generation dendrimers as the core and low-generation dendrimers as the shell. In comparison to single high-generation dendrimers, CSTDs show similar properties but are able to overcome limitations such as restricted drug loading, cytotoxicity, and limited EPR (Enhanced Permeability and Retention)-based tumor targeting [62,74]. The core–shell architecture is associated with an increase in both size and volume, which aids EPR-based passive tumor targeting. But, the distinct architecture of the CSTDs also enhances rigidity, which in its turn positively affects the nanosystems fluorescent emission properties [75].

Another dendrimeric feature gaining attention is an emission phenomenon, called non-tradition intrinsic fluorescence (NTIF). The first cases of fluorescent PAMAM dendrimers in absence of traditional fluorophores were reported in the early 2000 s, however at the time emission intensities were rather low. More recently, alteration of the PAMAM surface chemistry has led to a significant increase (~50 fold) in NTIF emission. The emission of this strong blue fluorescence (λ_{Ex} = 365 nm; λ_{Em} = 460 nm) is still under debate, as it also has been reported in other polymers, such as PPI and PEI, and may be related to pH- or oxygen-dependent fluorescence [76,77].

4.1.2. Micelles

Micelles are spherical, self-assembling nanosystems, with typical sizes ranging from 10 to 100 nm [78]. In case of polymeric micelles, the base of the nanoparticles are amphiphilic block copolymers (BCs), which are synthetic or natural molecules with distinct hydrophilic and hydrophobic regions. Usually, these block copolymers are linear and exist in a di-block (A-B) or tri-block (A-B-A) configurations, where A represents the hydrophobic block and B the hydrophilic one [79,80]. When a solution containing these BCs reaches a maximum concentration above which aggregation occurs, also known as the critical micelle concentration, this will initiate self-assembly into micelles. The configuration, either direct or reversible, is dependent on whether the BCs are present in a hydrophilic or hydrophobic solvent [2,80].

The BCs within direct micelles are ordered in a specific orientation; when in a aqueous solution the hydrophobic tails shape the micelle core and the hydrophilic heads form the outer shell (corona) [81]. While the core can act as a drug reservoir, the corona determines the charge, hydrophilicity, and the possibility of surface modification [82]. The inclusion of certain polymers or moieties contribute to the functionalization of the micelle.

The hydrophilic segment of the polymeric micelle can be polyethylene glycol (PEG), also known as poly(ethylene oxide) (PEO), which is able to provide stealth functionality due to prevention of serum protein binding and inhibition of RES uptake [83]. Other hydrophilic polymers such as poly(*n*-vinylpyrrolidone) (PVP) or poly(*n*-isopropyl acrylamide) (pNIPAAM) can be incorporated to create stimuli-responsive micelles. The hydrophobic segment can be made up of polyethers such as poly(propylene oxide) (PPO), biodegradable poly(esters)s such as poly(lactide-*co*-glycolic acid) (PLGA), or phospholipids such as disteroyl phosphatidylethanolamine (DSPE) [82,84,85].

A well-studied combination is the tri-block copolymer consisting of the hydrophilic PEO and the hydrophobic PPO, better known under the commercial name Pluronic® polyols. These polymers, which are structured as PEO-PPO-PEO or reverse PPO-PEO-PPO, can be categorized based on their hydrophilic-lipophilic balance (HLB) and PPO chain length [79]. The PEO:PPO length relative to the HLB value affects multiple micelle characteristics such as size, drug loading, and kinetic stability [83]. Pluronic® micelles reside hydrophobic drugs in the PPO core, while the PEO chains provide a stealth corona [84]. In order to even further improve drug delivery efficacy, Pluronic® micelles can be used in conjunction with stimuli-responsive materials [83].

Besides the polymeric variant, lipid micelles have also been studied as nanosystems for drug delivery. This variant is based on the di-block configuration, being composed of a hydrophilic PEG block and a hydrophobic phospholipid residue. The shape of the micelles is dependent on the ratio between the size of the hydrophilic- and hydrophobic segment, and on the concentration of the surfactants [86]. As with all other PEGylated nanosystems, the presence of superficial PEG is associated with an increased circulation time due to diminished RES uptake [87].

As a targeting approach, micelles can be subjected to stimuli-responsive functionalization. This can be either based on the smart function of the building blocks, for instance the polymer PVP being pH-sensitive and pNIPAAM being a thermosensitive polymer [82]. On the other hand, it could also be dependent on light-sensitive cleavable moieties attached to the micellar base. Multi-stimuli-responsive micelles can be designed for even more defined controlled drug delivery and release, being dependent on a simultaneous or sequential order of triggers [78].

4.1.3. Liposomes

Liposomes are self-assembling, spherical vesicles, which are composed of phospholipids [88]. As lipids are amphiphatic, this will result in the formation of a hydrophilic aqueous core surrounded by a hydrophobic bilayer. Liposomes can be classified into three types based on the number of bilayers present and the vesicle size: multi-lamellar vesicles (MLV, greater than 500 nm), multi-vesicular vesicles (MVV, greater than 500 nm), and unilamellar vesicles (ULV). For the ULVs, a distinction can be made between the large unilamellar vesicles (LUV, greater than 100 nm) and small unilamellar vesicles (SUV, 20–100 nm) [89,90].

Liposomes can be designed in a wide variety of lipid compositions, resulting in different sizes and functionalities. For instance, incorporation of cholesterol within the lipid bilayer will alter the phase transition behavior, resulting in liposomes with higher stability and therefore attenuated drug release [88]. As seen on other organic nanosystems, incorporation of PEG is a well-studied strategy to improve the pharmacokinetics of the nanosystem. Besides PEGylation, another common alteration to the phospholipids is fluorescence labelling. The addition of fluorescent lipids, such as Lissamine Rhodamine B (Rho-PE), prior to preparation of the lipid film establishes emission from the membrane itself. Besides the intrinsic properties, both the core and the bilayer can encapsulate or incorporate imaging agents after establishment of the liposome. Lipophilic tracers, such as DiD and DiO, reside within the lipid bilayer, while hydrophilic fluorophores, such as CF and calcein, can be found within the aqueous core. As mentioned in section 3.1.1, anthracycline drugs have a dual function being both a therapeutic agent and an imaging probe due to autofluorescence.

Being a versatile drug carrier, multiple generations of liposomes have been investigated in both preclinical and clinical studies. Especially encapsulation of doxorubicin, an anthra-cycline, which is considered a suitable drug for multiple indications, has been of significant interest. The classic formulation of pegylated liposomal doxorubicin, trademarked as Doxil® or Caelyx®, was approved by the FDA in 1995 [91]. This type of liposome showed increased therapeutic efficacy in comparison to free drug administration in certain indications. Despite reaching a higher area under the curve in the vasculature, bioavailability within the tumor micro-environment was still nominal due to a combination of minimal release and limited extravasation into tumor interstitium [11].

This limitation initiated a shift towards thermosensitive liposomes (TSLs). Similar to Doxil®, this drug carrier has a PEGylated coating to ensure extended circulation time. In order to allow for local triggered drug release, low-temperature sensitive liposomes (LTSLs) such as Thermodox® were developed by tuning the phospholipid ratio within the lipid bilayer. In 1999, Needham's group established that incorporation of both PEG and lysolipids results in a substantial increase in drug release rate and magnitude upon mild heating (40–42 °C) [92]. Subsequent animal studies confirmed that this LTSL formulation led to a significant increase in tumor drug concentration after mild hyperthermia exposure in comparison to free drug or liposomal formulations containing cholesterol [93]. In addition to LTSL, another TSL formulation was developed by the Lindner group. Interchanging the formulation to one containing DPPG$_2$ will, in addition to displaying a similar release rate as found in LTSLs, extend the residence time in systemic circulation while these TSLs are not PEGylated [94].

Besides phospholipid composition, the functionalization of liposomes is also an important feature to determine when, where, and how long facilitators should be applied. One of the manners to precisely determine tumor distribution and -uptake is via implementation of dual-labelled liposomes. Incorporation of two imaging moieties, for instance an optical probe and a contrast agent, allows for imaging within a single animal using multiple approaches. An effective and frequently applied combination is near-infrared fluorescence (NIRF) with magnetic resonance imaging [46]. While both imaging modalities provide high spatial precision, there is a considerable difference between penetration depth and type of information the modalities provide. Combining two modalities results in real-time, highly informative visualization of both tumor and liposomes, which is able to confirm results through side-by-side comparison. In addition, more controlled drug delivery can be established with the application of MR-guided high-intensity focused ultrasound (HIFU) due to accurate and dynamic tumoral temperature assessment.

4.2. Inorganic nanomaterials

Over the past decades, inorganic nanomaterials have gained increased attention for biomedical applications. Commonly, inorganic nanoparticles are based on metals, metal oxides, metalloids, or semiconductors [95]. Due to its distinctive physicochemical properties, high tailorability, and high stability, inorganic nanosystems can be applied in various biomedical applications [96]. In this section, characteristics and functionalization of carbon nanotubes, superparamagnetic iron oxide nanoparticles, gold nanoparticles, mesoporous silica nanoparticles, and quantum dots will be discussed (Fig. 1).

4.2.1. Carbon nanotubes

Carbon nanomaterials are able to form various structurally different forms, such as fullerenes, nanodiamonds, nanodots, and nanotubes [97,98]. Despite the base material, being an allotrope of carbon makes carbon nanotubes (CNTs) an inorganic nanosystem. In 1992, Lijima et al. discovered CNTs as a by-product of fullerene synthesis [99]. These nanosystems, which they described as graphitic microtubules with helical structures, have a size ranging from 50 to 100 nm [2,100,101]. A distinction can be made between single-walled carbon nanotubes (SWNTs), which are single layers of graphene sheets rolled seamlessly in a hollow cylindrical shape, and multi-walled carbon nanotubes (MWNTs), which are multiple SWNTs with different diameters wrapped around each other [102]. This typical cylindrical carbon-based shape does not only provide mechanical strength, but also contributes to optical, electrical, and thermal properties [103].

The intrinsic characteristics make carbon-based nanomaterials suitable as tracers for a variety of imaging modalities [104]. In particular NIRF imaging is frequently employed with CNTs, as they commonly exhibit strong optical absorption in the first NIR window (λ = 650 – 950 nm). Single-walled carbon nanotubes also display unique intrinsic fluorescence in the second NIR window (λ = 1000 –1350 nm). Imaging within the second NIR window allows for deep imaging with a high signal-to-noise ratio, which can be attributed to minimal tissue absorption at high wavelength [57,96,105]. In addition, CNTs also exhibit stable photothermal properties, due to a high photon-to-thermal energy conversion efficiency, and excellent optical properties for photoacoustic application [104,106].

Despite originating from organic nanomaterials, physical properties of CNTs make these prone to becoming cytotoxic due to poor dispersity and aggregation [102,104]. More so, carbon-based nanosystems are known to initiate toxic effects and may be related to the development of malignancies [107,108]. A variety of functionalization strategies can be applied in order to improve both safety and efficacy [96]. A well-studied SWNT functionalization is a coating based on phospholipid–polyethylene glycol (PL-PEG) linked with arginine–glycine–aspartic acid (RGD) peptide ligands. The presence of PL-PEG improves the biocompatibility, water solubility, and circulation time, while RGD improves tumor specificity as it displays a high affinity to $\alpha_v\beta_3$ integrins, which are overexpressed in tumor neovasculature [109].

The encapsulation of anti-cancer drugs does not only improve efficacy, but can also serve as a label for image-guided drug delivery. CNTs are considered to be excellent therapeutic nanocarriers due to the chicken-wire structure of the carbon network, which provides a large surface area. However, it is important to consider that both drug adsorption and -desorption are important drug delivery issues. Several factors, such as type of CNT, surface functionalization, type and number of chemical bonds, and pH, contribute to the manner of drug delivery [96,103]. Chadar et al. have described the functionalization of this nano system specific for the delivery of doxorubicin in great detail [103].

4.2.2. Superparamagnetic iron oxide nanoparticles

Superparamagnetic iron oxide nanoparticles (SPIONs) are a type of magnetic nanoparticles. SPIONs consist of an iron oxide core, either magnetite (Fe_3O_4) or maghemite (γFe_2O_3), and a hydrophilic (polymer) surface coating [100]. In order to exhibit super *para*-magnetism, the nanoparticles should have a size between 10 and 20 nm [2,110]. SPIONs are multifunctional due to their intrinsic imaging properties as a contrast agent for both magnetic resonance- and photoacoustic imaging, and as a drug vehicle and photothermal agent for therapeutic purposes [111,112]. Placement of SPIONs in an alternating magnetic field results in build-up of magnetic energy, which is subsequently released in the form of heat.

To avoid biofouling and colloidal instability in aqueous solutions, SPIONs should be functionalized by surface coating [100,110]. The most commonly reported SPION functionalizations are based on either ligand exchange or hydrophobic interactions [113]. The ligand-exchange approach requires a functionalizing molecule with high affinity for the iron oxide surface, such as dopamine, polypyrrole (PPy)), phosphines, and amines. Other possible ligand functionalizations are of a biological nature, such as RGD, chlorotoxin, or folic acid (FA) [114]. The functionalization of SPIONs with FA has a dual function, as it can be used as both a surface coating and as a targeting agent [115]. As the ligand-receptor interaction will result in increased accumulation, this will result in improved relaxivity and therefore strong intratumoral contrast enhancement. Efficient anti-biofouling strategies could be PEGylation or the use of zwitterionic-surfactant functionalized SPIONs.

4.2.3. Gold nanoparticles

Gold nanoparticles (AuNPs) can be applied in IGDD studies due to the unique optical and photothermal properties [116,117]. These particles can be produced in different sizes and geometries, such as nanospheres, nanoshells, nanorods, nanocages, and nanostars. The wide variety in AuNP geometries is related to the synthesis method, the concentration of gold salt, and the environmental temperature and pH during synthesis [118]. While each shape exhibits different characteristics, the common denominator is the surface plasmon resonance (SPR). Upon light exposure, local surface interaction with the metal particles will either cause light re-emission or conversion into heat. AuNPs display higher absorption and scattering in comparison to the traditional interaction of for instance dyes [117,119]. The displayed SPR spectrum depends on the size, shape, composition, and functionalization of the AuNPs [120]. The wavelength range for optimal AuNP excitation lies between the window for optimal tissue penetration (NIR-I, λ = 650 – 950 nm), resulting in minimal interaction and therefore high tissue penetration [120–122].

AuNPs are considered inert and non-toxic in the biological setting, making these particles ideal for clinical application. As with most other nanosystems, tumor-specific targeting can be established through surface modification with structures such as MMP-2 and PD-L1. Combining gold-based nanosystems with photosensitive agents, such as IR820 and Ce6, induces synergistic PTT/PDT upon NIR irradiation. Initially, the gold structure will respond to irradiation through a temperature increase due to high photothermal conversion [117]. Subsequently, light-induced activation of the photosensitizer will result in local toxicity through generation of reactive singlet oxygen ($^1O_2$), a type of reactive oxygen species (ROS) [123]. Amina et al. recently discussed AuNP functionalization strategies for drug delivery in detail [118].

4.2.4. Mesoporous silica nanoparticles

Mesoporous silica nanoparticles (MSNs) are silica (SiO_2)-based vectors, characterized by the presence of mesopores. MSNs have a broad application due to their tunability, as both pore size and structural arrangement can be adjusted [124]. As defined by the International Union of Pure and Applied Chemistry (IUPAC), mesoporous materials have pores on the external surface in the range of 2–50 nm [125]. MSNs can be categorized in i) ordered mesoporous silica NPS, and ii) hollow or rattle-type mesoporous silica nanoparticles [2].

Despite the stable Si-O-Si framework, MSNs are considered to be biodegradable under physiological conditions [126]. Therefore, surface modification is required to optimize the biodegradation kinetics and prevent silica-associated toxicity [124,127]. Thi et al. discussed the stimuli-sensitive functionalization suitable for MSNs in great detail [128].

Besides conventional functionalization such as PEGylation and conjugation with tumor-targeting ligands, examples of MSN specific functionalization are metal-ion doping and pore control. In order to reinforce the MSN framework, doping with Mg^{2+} ions could be an option via the transformation into Si-O-Mg networks. Other biological elements, such as Ca and Fe, could also be incorporated to make the biodegradability dependent on the acidic tumor environment or the presence of specific proteins [126].

Control of the MSN pore volume and size is an essential requirement in order enhance the drug loading capacity and minimize drug leakage. On the one hand, mesoporous silica nanoparticles with large pores exhibit enhanced loading efficiency of large molecular weight drugs. But on the other hand, significantly large pore sizes are associated with excessively thin pore walls, and may require the inclusion of stimuli-responsive gatekeepers to prevent drug leakage from the MSN hollow interior [126].

4.2.5. Quantum dots

Quantum Dots (QDs) are semiconductor nanocrystals, which are of interest for imaging applications due to their increased photochemical stability and brightness in comparison with organic dyes [129,130]. In general, QDs consist of three parts: a core, a shell, and a capping material. The core can be composed of various semiconductor materials, for instance a combination of group II–VI elements (e.g. CdSe, CdTe) or group III–V elements (e.g. InP, InAs). To protect the core from oxidation and photobleaching, the semiconductor core is coated with a zinc sulfide (ZnS) shell [2,129,131]. The addition of a capping material does not only protect the core–shell structure, but also minimizes aggregation, and enhances bioactivity. In addition, this layer is also suitable for the embedding of contrast agents and hydrophobic drugs [100,132].

QD synthesis occurs either through the top-down- or the bottom-up method [133]. The size of the quantum dot plays an important role in the establishment of the optoelectronic properties, also known as the quantum size effect. This phenomenon is related to the inverse relationship between quantum dot size and energy band gap. In other words, increasing QD size will result in a decreasing energy band gap, and therefore initiates a redshift through an increase of the corresponding excitation/emission wavelength [132,134]. The broad optical range of fluorescence, from near ultraviolet to near infrared, makes these nanosystems highly attractive for biomedical applications. In addition, QDs are also suitable for optical multiplexing due to their broad excitation profiles and narrow, symmetric emission spectra [135].

Despite the suitable characteristics of heavy-metal QDs for theranostic purposes, research has shifted towards the development of metal-free alternatives due to intrinsic toxicity. For non-heavy metal QDs, a distinction can be made between silicon QDs and carbon-based QDs (CQDs). In the past decade, CQDs have gained increased attention due to characteristics such as low intrinsic toxicity, strong fluorescence intensity, and long photostability. Carbon-based QDs can be subdivided into three categories according to structure in graphene quantum dots (GDs), Carbon Dots (CDs), and Polymer Dots (PDs) [136].

CDs were discovered in 2004 as a by-product of SWNT synthesis by the group of Xu [137]. Unlike other carbon-based nanomaterials, these quantum-size carbon analogues have inherent aqueous solubility, and therefore do not require specific functionalization to be stable in buffers [96]. And, like their heavy-metal counterpart, CDs express good optical stability and tunability. In order to further enhance the physicochemical properties, carbon dot doping can be performed using essential physiological elements, such as Fe, Mg, and Ca, or more eco-friendly alternatives to the heavy-metals, such as Au and Ag [138]. This has even led to the development of green carbon dots, in which the structural components find their origin in natural sources, such as fruits and vegetables [139].

With a size smaller than 10 nm, QDs have the tendency to behave like nanocolloids, and therefore post-synthesis surface modification is required to improve their stability in biological environments. This can be established via either encapsulation, ligand exchange, or bioconjugation. However, it is important to keep in mind that surface coating should not impede important factors such as fluorescence intensity by shielding, particle size, and biocompatibility [134]. Mattoussi et al. have identified various surface functionalization strategies for quantum dots [140].

4.3. Hybrid nanosystems

The above mentioned nanosystems have gained increased interest for drug delivery due to their unique characteristics and widespread application. However, combining different materials may overcome the weaknesses of a single component, can enable synergistic functionalities, and is highly tunable. These hybrid nanosystems contain two or more different components, which can be a combination of organic, inorganic, and polymer materials.

The inclusion of polymers in nanohybrids is mainly focused on improving stability and therapeutic activity. Fang et al. designed multifunctional nanosystems based on a gold nanocage surrounded by a selenium and chitosan shell [141]. While the nanocage on its own will work as a photothermal agent and a photoacoustic contrast agent, incorporation of a polymer shell will enhance the loading capacity of the drug and initiate drug release at hyperthermic temperatures. Likewise, a combination of gold nanocages surrounded by a thermosensitive lipid layer will result in a hybrid system functionalized through heat-triggered drug release [9].

5. Imaging modalities

In the last decades, extraordinary technical development has led to a wide range of clinical imaging modalities able to obtain structural, functional, and molecular information about the tumor micro-environment [46]. In addition, this also allows for real-time visualization and quantification of drug delivery [142]. Despite these developments, each imaging technique is still limited to a specific penetration depth and resolution (Fig. 2). In order to circumvent this limitation, it is possible to employ complementary modalities to monitor the region of interest. This strategy, also known as multimodal imaging, is an excellent manner to improve image-guided drug delivery [143].

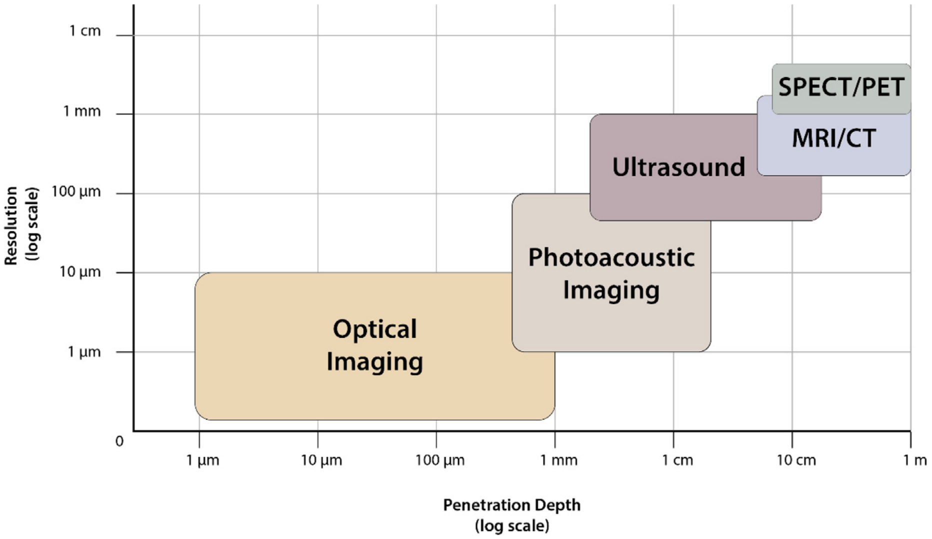

Fig. 2. Overview of the resolution and penetration depth of modalities for image-guided drug delivery. This figure is based on Wang et al. [257], Najafzadeh et al. [258], Betz et al. [259], and Walter et al. [143].

Optical imaging (OI) is an elementary imaging technique, which is based on reflectance and absorbance of non-destructive light over a wide spectral range (Table 1) [19]. OI covers both fluorescence- and (bio)luminescence imaging [13]. The latter is not discussed in this review, but has been described in great detail by others [27,144]. Fluorescence imaging (FI) is frequently applied in preclinical models as it provides high sensitivity, allows for repeated dosing, and is non-radioactive [145]. However, optical imaging using visible light (λ = 380 – 700 nm) is limited by poor tissue penetration in biological tissues. Application of light at near-infrared frequencies (λ = 700 – 3000 nm) allows for visualization with high spatial precision, deeper penetration, which is still limited to a maximum depth of several millimeters due to absorption and scattering, and decreased background fluorescence [21,146,147]. However, the selected frequency should fall within the optimal NIR window (λ = 650 – 950 nm) as a wavelength below 650 nm exhibit diminished penetration, while a wavelength exceeding 950 nm display more pronounced water absorption [35,121].

Photoacoustic imaging (PA) is a hybrid imaging modality based on the ‘‘light in, sound out” principle (Table 1) [123,148]. After optical illumination of the target area, absorbed light will cause thermoelastic expansion, which generates acoustic waves. These can subsequently be detected by an ultrasound transducer for visualization [41,44]. In comparison to fluorescence imaging, PA has an improved penetration depth up to 8 cm in soft tissue and improved resolution due to limited scattering of sound in comparison to light [44,148]. In addition, alteration of the ultrasonic frequency can even further improve the resolution and penetration depth [148]. Photoacoustic imaging exploits the rich optical contrast between both intrinsic and administered contrast agents (Table 2). Intrinsic tissue chromophores, such as hemoglobin, melanin, and water, can provide structural information. Administration of exogeneous contrast agents, for instance by encapsulation in tumor-specific nanosystems, can even further enhance contrast and allows for deeper imaging [41]. As all of these agents exhibit characteristic absorption spectra, photoacoustic imaging at multiple wavelengths allows for distinction between signals from different agents. Due to the non-invasive and non-ionizing nature, PA is suitable for long-term longitudinal monitoring [41].

Ultrasound (US) is a minimally invasive imaging technique, which is widely applied in the clinic for both diagnostic and therapeutic purposes (Table 1). US is based on longitudinal pressure waves in frequencies above the human audible range (20 kHz) [12,149]. Application of US requires a uniform medium, as interference with either air or bone induces acoustic reflections or energy absorption [121,150]. US parameters, such as intensity and frequency, can be optimized for the target area in order to produce minimal biological interference and to allow imaging with high spatial and temporal resolution [121,149]. Despite not being included in this review, it is worthwhile to mention that microbubbles are frequently used as US contrast agents. This intrinsic ability is related to high compression and strong scattering of signal [151]. Another factor to take into consideration is respiratory movement, as this can create motion artefacts [41]. Motion artefacts are able to influence both IGDD and IGDR, as precise imaging and -triggering are essential for optimal application. Next to imaging, ultrasound can also be used as a drug delivery facilitator in form of high-intensity focused ultrasound [121].

Magnetic Resonance Imaging (MRI) is a tomographic imaging modality based on non-ionizing radiation. Multiplanar imaging of the target tissue can be used to obtain anatomical, functional, and metabolic information (Table 1) [152]. Besides being devoid of ionizing radiation, other important characteristics of this technique are the high spatial resolution and -penetration depth [46,153]. In addition, MRI is an established technique due to its excellent soft tissue contrast enhancement. As the signal intensity of MRI is influenced by the relaxation rate of water protons, the high water content of soft tissues will result in relatively long T_2 and T_1 relaxation times. Therefore, visualization of for instance blood, brain, or skeletal muscle will generate strong MR signals in contrast to structures with low water content [154]. As mentioned in section 3.1.2, administration of MRI contrast agents even further improves the sensitivity to differentiate between healthy- and tumor tissue (Table 2) [45,46]. Selection of a suitable MR sequence is another vital parameter in data acquisition, which is dependent on the region of interest. For instance, while spin echo sequences can distinguish tissues in general based on water and fat content, more in-depth information can also be obtained with MR imaging. Comparing differences between relaxation times between intra- and extravascular water protons allows for assessment of tissue metabolic activity based on the blood-oxygenation-level-dependent signal [155,156].

Computed Tomography (CT), also known as X-ray computed tomography, is a non-invasive, tomographic imaging technique (Table 1). Similar to MRI, CT is suitable for obtaining high resolu-

Table 1
Overview of imaging modalities available for image-guided drug delivery. Table is based on Wallyn et al. [13], van Moolenbroek et al. [260], Sarbadhikary et al. [14], and Walter et al [143].

	FI	PA	US	MRI	CT	SPECT	PET
	Fluorescence imaging	Photoacoustic imaging	Ultrasound imaging	Magnetic Resonance imaging	Computed Tomography imaging	Single-photon emission computer tomography	Positron emission tomography
Source	NIR light	Sound waves	Sound waves	Radio waves	X-rays	Low-energy γ-rays	High-energy γ-rays
Resolution	1–5 mm	50–500 µm	50–500 µm	10–100 µm	50–200 µm	1–2 mm	1–2 mm
Penetration Depth	<1 cm	A few cm	Several cm	No limit	No limit	No limit	No limit
Imaging moieties	Fluorescent dyes	Tissue chromophores	Microbubbles	Gd chelates/ SPION	Heavy elements / ionidated molecules	Radionuclides	Radionuclides
Information	Physiological Molecular	Physiological Molecular	Anatomical Physiological	Anatomical Physiological Functional	Anatomical Physiological	Anatomical Physiological Functional	Anatomical Physiological Functional
Advantage	• Non-ionizing • Multichannel imaging	• Non-ionizing • Limited scattering	• Non-ionizing • Minimal biological interference	• Non-ionizing • Soft tissue contrast	• High resolution • Whole body imaging • Fast acquisition	• High sensitivity • Whole body imaging	• High sensitivity • Whole body imaging
Disadvantage	• Low resolution • Limited penetration depth	• Low resolution • Limited penetration depth	• Low resolution • Poor contrast	• Poor sensitivity • Long acquisition time	• Low sensitivity • Ionizing radiation • Poor tissue demarcation	• Low resolution • Ionizing radiation • Long acquisition time	• Low resolution • Ionizing radiation • Long acquisition time

tion structural and morphological information [51]. However, the main difference between these imaging modalities is the use of ionizing radiation. While MRI is based on water proton relaxation behavior, CT is dependent on differences in X-ray attenuation [13,50]. In addition to radiation exposure, another weakness is the relative low sensitivity between soft tissues [40]. In order to differentiate between tumor and peritumoral tissues, administration of contrast agents is required [50]. Regardless of the disadvantages, CT is frequently used in both experimental and clinical studies since it is a fast, cost-effective method with high resolution and unlimited penetration depth. For preclinical CT imaging, a distinction in spatial resolution can be made between mini-CT (50 – 200 µm), micro-CT (1 – 50 µm) and nano-CT (0.1 – 1 µm) [13].

Single-Photon Emission Computed Tomography (SPECT) and **Positron Emission Tomography (PET)** are quantitative nuclear imaging techniques, as they are able to provide metabolic and functional information (Table 1) [56]. Both imaging techniques are based on non-invasive tracking by labelling compounds with radionuclides. Due to the detection of high-energy photons from these radionuclides, SPECT and PET exhibit unlimited penetration depth with high sensitivity [52]. The difference between these two tomography-based imaging techniques lies in the applied radioisotopes and the mechanism for signal generation and detection. As mentioned in section 3.3, the physical properties of the radionuclide, such as half-life (t½) and γ-decay energy (γ), are important for optimal tomographic imaging. A considerable disadvantage of PET over SPECT lies in the ability to image multiple compounds within the same subject of the latter. As PET imaging is based on energy detection from photons during positron annihilation, only a singular signal can be detected as these all display the same energy (511 keV). This is in contrast to SPECT imaging, as these radionuclides all display unique energy emissions, and therefore can be detected individually [52].

6. Preclinical studies

As discussed in section 4, a plethora of nanoparticles is available with tunable properties such as size, charge, type of surface modification, shape, and biocompatibility [11]. An important factor to take into consideration during nanoparticle design is the tumor pathophysiology.

Tumor pathophysiology contributes to passive nanoparticle accumulation due to an increased vascular permeability in combination with a lack of functional lymphatics, coined the Enhanced Permeability and Retention (EPR) effect [1]. However, this phenomenon is considered to be unreliable as a basis for drug delivery, as tumors are heterogeneous and exhibit irregular vascular permeability during development [8]. The application of an external trigger, whether it be heat, ultrasound waves, or light, can positively affect both the nanosystem and the tumor-microenvironment. For instance, local application of mild hyperthermia (40–43 °C) is able to elicit a physiological response, resulting in an increase in blood flow, vascular permeability, and interstitial fluid pressure [157]. Therefore, heat-promoted EPR can be applied to improve intratumoral accumulation and subsequently initiate triggered release.

For treatment purposes, it is important to define where, when, and how long the facilitator should be applied. It is crucial to localize and precisely target the tumor as off-target triggering results in poor drug delivery, and may cause local and systemic toxicity. IGDD is able to support and facilitate precise tumor treatment, as it is able to visualize nanoparticle distribution within the tumor micro-vasculature and therefore the starting point of stimulation. Therapeutic efficacy for any smart drug delivery system would be optimal when initiation of triggered drug release occurs after

Table 2
Overview of a selection of imaging moieties available for image-guided drug delivery.

	FI	PA	US	MRI	CT	SPECT	PET
Nanosystems (intrinsic)							
Dendrimers							
Micelles							
Liposomes							
CNT	[104,117,261]	[104,117,260]	[96,104]				
SPION		[44,111,123]		[13,110,117,260]			
GNP	[120,262]	[40,117,260]			[51,117,260]		
MSN							
QD	[13,117,260]						
Endogenous agents							
Hemoglobin		[40,41]					
Polydopamine (melanin) (PDA)		[40]					
Protoporphyrin IX (PpIX)	[19]						
Polypyrrole (PPy)		[44]					
Drugs							
Doxorubicin (Dox)	[38,263]						
Topotecan	[39,263]						
Fluorescent dyes							
Calcein	[12]						
Carboxyfluorescein (CF)	[1]						
Cy5.5	[20]						
Cypate	[20]						
FITC	[19,20,260]						
Indocyanine green (ICG)	[19,20]	[40,260]					
IR780	[20]						
Methylene blue (MB)	[19,20]	[40,260]					
Phthalocyanines	[20]	[264]					
Rhodamine (Rho)	[260]	[260]					
Metals							
Gadolinium-based (Gd^{3+}, Gd_2O_3)				[13,51,260]	[51]		
Iodine-based (iopromide, iohexol)					[260]		
Gadopentetate dimeglumine (Magnevist®)				[13]			
Radionuclides							
^{18}F							[53,260]
^{64}Cu							[52,53,260]
^{89}Zr							[52,53,260]
^{99m}TC						[52,53,260]	
^{111}In						[52,53,260]	
^{188}Re						[52,53,260]	
^{213}Bi					[51]		
Others							
Microbubble-based			[13,260,265]				
Organic radicals				[71,165]			

FI = Fluorescence Imaging, **PA** = Photoacoustic imaging, **US** = Ultrasound imaging, **MRI** = Magnetic Resonance Imaging, **CT** = Computed Tomography, **SPECT** = Single-Photon Emission Computed Tomography, **PET** = Positron Emission Tomography.

(maximum) tumor accumulation. Taking the substantial variation in and between research groups on the same technique into account, a quantitative way to measure intratumoral accumulation is crucial to improve treatment strategies. Functionalization of nanoparticles through imaging moieties could provide important feedback on SDDS distribution and tumor uptake. In this section we will discuss preclinical application of both organic and inorganic nanosystems. The selected articles give an insight into the progress of image-guided drug delivery over the past decades. While a significant part of literature on nanosystems is focused on targeted therapy for cancer, we dispute that only a small number can be considered as true image-guided drug delivery.

6.1. Dendrimers

6.1.1. Conventional dendrimers

The strength of dendrimers as a nanosystem for solid tumor treatment lies in the generational architecture. Studies have shown that non-modified, high-generation dendrimers can be succesfully employed to improve local drug delivery in a wide range of cancers [63]. However, strategies exploring the full potential of the nanosystem incorporate multiple agents either by encapsulation within the core or conjugation to the branching units [158]. For instance, Cao et al. designed a G5 PAMAM dendrimer with encapsulated paclitaxel (PTX) within the hydrophobic core and harboring an imaging ligand on the exterior surface [159]. Based on two motifs, a NIR fluorescent dye cypate and RGD, the presence of the conjugated imaging ligand allows for dendrimer localization through fluorescence imaging and simultaneous exhibition of strong tumor selectivity. As the fluorescence of plain PAMAM dendrimers is easily overshadowed by biological auto-fluorescence, minor modifications such as addition of an imaging ligand can readily improve dendrimer imaging [159].

Another theranostic strategy that has been implemented with dendrimers is the incorporation of phthalocyanines (Pc). Pc is a photosensitizer with excellent NIR optical properties, however due to its hydrophobic nature the tendency to aggregate is high, resulting in self-quenching. Taratula et al. show that noncovalent encapsulation of Pc within 60 nm dendrimers results in emission at 710 nm and 815 nm, enabling fluorescence imaging and PDT [160]. While irradiation accompanied by visualization in this study is not a true example of image-guided drug delivery, it is a valuable example of the multifunctionality that dendrimers provide.

As mentioned in a previous section, for image-guided drug delivery purposes dendrimers are most commonly used as a carrier for MRI contrast agents [64,69]. Gd-functionalized dendrimers show increased sensitivity in neoplastic tissues for several reasons. Besides increased accumulation within the TME due to inadequate lymphatic drainage, which holds for all nanosystems, there are factors related to MR sensitivity specifically for dendrimers [158]. First, the hyperbranched structure of the dendrimer at higher generations is associated with an increase in surface group density. This allows the nanosystem to become more spherical, resulting in a higher amount of Gd^{3+} present [158,161]. And second, further functionalization in form of structural alterations could even further improve dendrimer-based magnetic resonance imaging [67].

In order to minimize the risk on gadolinium-related toxicity, it is crucial that the dendrimer exhibits proper retention and that the encapsulation of a low dose is sufficient for high sensitivity imaging. As shown by Mekuria et al., encapsulation of oxidized Gd^{3+} ions within the core of a high generation (G4.5) PEGylated PAMAM dendrimer results in negligible leakage levels in comparison to the same scaffold without the presence of PEG [162]. Subsequent in vivo MR imaging of the G4.5-Gd_2O_3-PEG nanoparticle showed positive contrast enhancement for both T_1 and T_2-weighted images. Despite proving that the dense population of Gd^{3+} present within the dendrimer core results in a dual-modal imaging agent with superior contrast effect, the MR images showed that this nanosystem is highly subject to renal excretion. In comparison to the other major organs, the change in contrast enhancement from kidney to bladder occurred relatively quickly after administration, indicating excretion.

While in this case the hepatic signal intensity was only slightly enhanced in comparison to the kidney, nanosystems are generally highly vulnerable to hepatic or splenic clearance due to opsonization and scavenging by the mononuclear phagocyte system [163]. Traditional anti-fouling properties such as PEGylation have proven to be successful in some cases, however novel strategies have cleared the way for improved diagnostic- and therapeutic applications. Studies on SDDS modification with zwitterionic molecules have shown that these ligands are more biocompatible, and do not trigger antibody production on a magnitude as PEG does [163,164].

As functionalization with zwitterionic molecules minimizes hepatic excretion, this strategy could be useful to enhance diagnosis of metastatic hepatic tumors through MR imaging. Zhou et al. designed a dendritic contrast agent (DCA), which is functionalized with zwitterionic molecules, and composed of a β-cyclodextrin (β-CD) core with biodegradable polyesters [66]. The implementation of a high generation (G4) dendrimer resulted in longer systemic retention and a 3.5 fold-increase in R_1 value in non-tumor-bearing animals in comparison to Magnevist®. The heterogeneous, low signal intensity within in healthy hepatic tissue and high signal intensity in blood vessels indicated that the presence of zwitterionic molecules contributed to a decreased DCA uptake by hepatocytes and Kupffer cells. In tumor-bearing animals, T_1-weighted images revealed a distinct increased intensity, indicating metastatic tumors, within 30 min after administration.

Besides improved pharmacokinetics, another important aspect of these DCAs is carrier degradability. Studies on the dendritic ligand showed that the hydrolysis kinetics were pH-dependent; being stable under acidic conditions and showing increased hydrolysis at neutral pH (∼7.4). The presence of esterase, which is an endogenous enzyme present within cells, accelerates the reaction kinetics and therefore also induces content release within the tumor cells [57]. In vitro studies showed that 50 % of the DCAs were hydrolyzed within 4 h at pH 7.4 in the presence of esterase. These results, given in combination with the low accumulation in the main organs, indicates that this type of DCA exhibits a relatively long blood circulation time, specific accumulation at the tumor site, and prevents systemic toxicity from long-term Gd retention due to the biodegradability.

As mentioned before, alternative imaging probes with higher safety are developed in combination with nanosystems. These contrast agents should provide similar or better paramagnetic properties in comparison to Gd-based CAs. A relatively novel candidate in this field are the dendrimers functionalized with metal-free organic radical contrast agents (ORCAs), also known as radical dendrimers. Initial functionalization of PAMAM and PPI dendrimers with PROXYL radical units did provide MRI enhancement, however issues with hydrophobicity and aggregation limited further development [71]. One way to overcome these limitations is the implementation of an amino acid linker between the dendrimer branches and the organic radicals [71,165]. This design makes the structure completely soluble at physiological pH without diminishing the high relaxivities. Zhang et al. studied the in vivo applicability of poly(phosphorhydrazone) (PPH)-based radical G3 dendrimers with 48 PROXYL radical units for glioblastoma diagnosis [166]. The amino acid tyrosine (Tyr) forms the linker, resulting in G3-Tyr-PROXYL dendrimers. Intracerebral T_1-weighted images of glioblastoma-bearing animals, showed strong intratumoral contrast enhancement after administration of the ORCA, reaching similar levels at a dose 4 times lower than the Gd-based control (Fig. 3A).

6.1.2. Dendrimer complexes

The above mentioned examples indicate that dendrimer-based contrast agents are convenient for tumor diagnosis without major side effects. G8 dendrimers have even been used as a tool to determine the impact of γ-irradiation on tumor vessel permeability [167]. Therefore, further dendrimer functionalization into theranostic systems may seem fairly easy, only requiring the encapsulation of a suitable drug. However, it is important to consider that these contrast-enhancement nanosystems are considered for single-dose administrations, while efficacy studies with theranostics may require multiple doses with corresponding cumulative side effects. For instance, Fillipi et al. have performed a longitudinal study on the therapeutic efficacy of dendrimerisomes in comparison to well-established paramagnetic liposomes [73,168]. Self-assembly of the low generation Janus dendrimers (3,5-C_{12}-EG-$(OH)_4$) results into spherical DSs vesicles with unilamellar membranes, which were co-loaded with prednisolone phosphate and the lipophilic MR contrast agent GdDOTAGA$(C_{18})_2$. T_1-weighted axial images showed inhomogeneous intratumoral DSs distribution, which could be attributed to local difference in vascularization. Similar MR contrast values were observed for the paramagnetic liposomal counterpart, with both also showing significant and persistent intensities in spleen and liver for several days after administration of every single dose (Fig. 3B). The two different nanosystems both showed anti-tumor efficacy, with initial differences in growth visible at day 11 and 13, which turned insignificant at the end of experimental monitoring after 15 days. In the end, both MR images and Gd quantification indicated long lasting DSs residence in tumor tissue and other organs, which may raise safety concerns.

Another evolved dendrimer type suitable for image-guided drug delivery are core–shell tecto dendrimers (CTSDs). Song et al. designed a CSTD based on a core G5 PAMAM dendrimer with β-CD and a shell comprised of multiple G3 PAMAM dendrimers functionalized with adamantane and gadolinium [169]. Self-assembly of the two dendrimer generations into CSTD complex is ensured through the supra-macromolecular host–guest recognition between β-CD and adamantane. In vitro comparison with G5 PAMAM dendrimer analogues and Magnevist® showed that CSTD complexes exhibit MR signal intensities with a 1.5 and 1.6-fold increase in r_1 relaxivity. Both dendrimer types are able to induce significant in vivo tumor MR contrast enhancement, regardless of the route of administration being intravenously (i.v.) or peritumorally (p.t.). However, the CSTD complexes show a higher MR signal intensity and signal-to-noise ratio with a peak value at 2.5 (i.v.) and 3 h (p.t.) post-injection, which can be attributed to an amplified passive EPR effect (Fig. 3C).

Taking this concept a step further, Liu et al. makes optimal use of the space on the in- and outside of the CSTD complex [170]. The internal cavities of the G5 core housed AuNPs, while the G3 surface was decorated with multiple structures; i) diethylenetriaminepentaacetic acid (DTPA) to chelate with Gd ions, ii) RGD peptide ligands for increased affinity to $\alpha_v\beta_3$ overexpressed tumors, and iii) 1,3-propane sultone (1,3-PS) to improve anti-fouling properties. CT and MR imaging revealed that in vivo intratumoral peak values were reached 1 h post-injection, and that signals remained strong for up to 3 h in comparison to the non-targeted CSTD counterpart. This multifunctional CSTD complex could be a strong candidate for future studies on image-guided drug delivery.

6.2. Micelles

6.2.1. Conventional micelles

Unlike the other nanosystems discussed in this review, the geometry and design of micelles is straightforward. Functionalizations are either made to i) the polymers which form the micelle or to ii) the core of the nanosystem by including multiple agents within. While it is possible to include multiple imaging agents within the nanosystem, the selection of the right block copolymer is the most elementary. For instance, Yang et al. have designed a micellar system, which is composed of BCs consisting of poly (acrylamide-*co*-acrylonitrile-*co*-vinylimidazole) (PAAV) as the hydrophobic block and hydrophilic PEG [171]. Besides being amphiphilic, this polymer is also thermosensitive and pH-responsive, which makes it highly suitable for targeted drug delivery. This multifunctional system exploits the pH of the tumor micro-environment, which generally lies between 5.6 and 7.0 [172], in combination with application of NIR laser irradiation. In vitro studies on this nanosystem showed that a decrease in pH value led to a simultaneous decrease in the upper critical solution temperature. Therefore, upon encountering the acidic TME the intermolecular interactions within the polymer will occur at lower temperatures, causing particle disassembly and subsequent rapid drug delivery upon application of local thermal therapy.

Whole animal fluorescence imaging showed that these micellar structures effectively target solid tumors, as intratumoral peak value can be seen 24 h post-injection. This was confirmed by photoacoustic imaging of the tumor at the same time point, as the micelle encapsulating IR780 and DOX showed a 1.5-fold increase in PA signal in comparison to administration of free theranostics (Fig. 4A). Subsequent laser irradiation (808 nm, 1 W/cm^2, 5 min) of the tumor region at the 24 h time point confirmed the intratumoral presence of the micellar system as shown by fluorescence. Thermal imaging revealed intratumor photothermal conversion due to a rapid increase in temperature, which was absent in the tumor-bearing control. Animals treated with micellar IR780/DOX with NIR treatment showed complete tumor inhibition without recurrence from day 9 up to the end of the study period at day 30. In contrast, animals treated with micelles + IR780 with NIR and micelles + DOX without NIR were unable to completely eliminate the tumor.

6.2.2. Micelle complexes

Another neat approach to overcome the multitude of drug delivery challenges could be a hierarchical targeting strategy. In this case, the outer layer is responsible for navigation towards the tumor environment, which will subsequently be lost, revealing the core nanosystem containing theranostic agents. Cherukla et al. designed a micellar-based nanosystem, which was enclosed by a thermosensitive lipid coating [173]. This outer layer contributes to the tumor delivery in two ways; charge conversion of the zwitterionic lipid DPPC due to the acidic tumor environment, followed by lipid deshielding as a response to local NIR irradiation. Therefore, this will result in local exposure of the core micellar structure, which was based on PEI for high internalization and lithocholic acid as a drug penetration enhancer, enclosing ICG and PTX. Whole animal fluorescence imaging studied of these LIL-PTX NPs showed that intratumoral accumulation peaked at 24 h after administra-

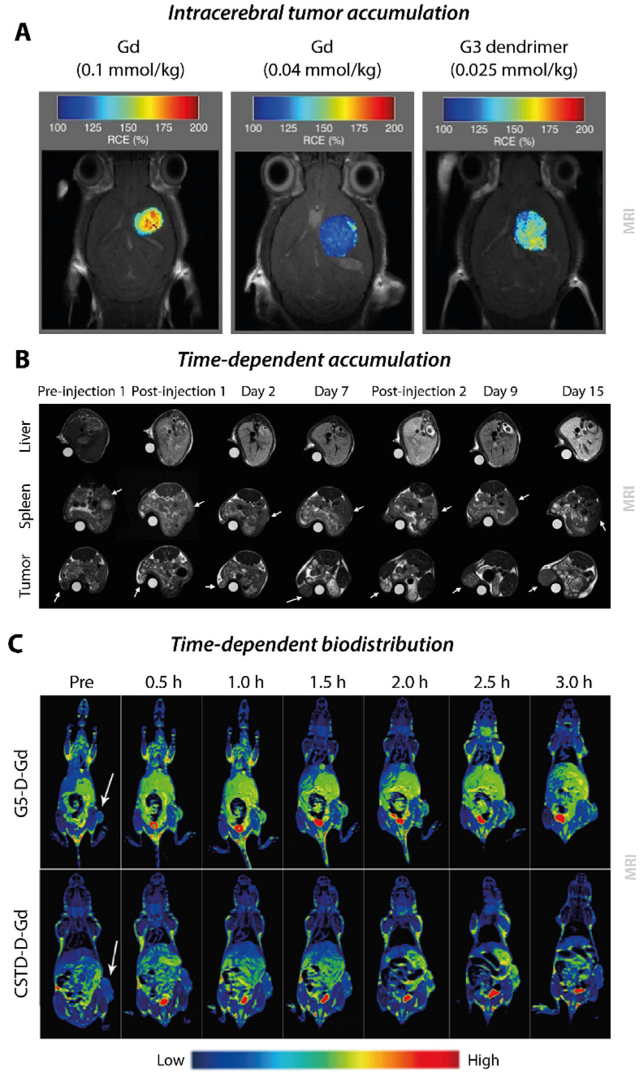

Fig. 3. In vivo imaging of dendrimers. **A**) Zhang et al. demonstrated the possible application of radical dendrimers as a metal-free MRI contrast agent [166]. Relative contrast enhancement of T_1-weighted images showed that G3 radical dendrimers exhibit similar contrast enhancement as the standard Gd dose of 0.1 mmol/kg at 60 min post-injection. **B**) Filippi et al. observed longitudinal MR contrast following dendrimersomes within a melanoma-bearing mouse [168]. Initial administration of PLP-Gd-DS resulted in inhomogeneous contrast enhancement within the tumor, followed by a time-dependent decrease. Administration of a second dose led to similar results, gaining increased enhancement for approximately 24 h, followed by a substantial decrease. Though not demonstrating remarkable contrast enhancement within muscle, both spleen and liver showed substantial and persistent contrast enhancement. **C**) Song et al. demonstrated the superiority of core–shell tecto dendrimers over conventional dendrimers for T_1-weighted imaging [169]. While both nanosystems are able to induce significant contrast enhancement, CSTDs demonstrated a higher MR signal intensity and signal-to-noise ratio at 2.5 h after administration. Adapted with permission from [166,168,169].

tion, with simultaneous clearance from other major organs such as liver and spleen. Therefore, laser irradiation (808 nm, 2 W/cm^2, 10 min) was applied at that time point. Thermal imaging of the tumor region revealed that the presence of LIL-PTX NPs contributed to a significant increase in tumor temperature in comparison to the controls. This is in line with the anti-tumor therapy studies, as LIL-PTX NPs without laser irradiation showed no activity, while a single dose with laser irradiation resulted in complete tumor ablation without recurrence during the 14 day study period. A similar targeting strategy was applied by Zhang et al, which proposed a ‘pomegranate’ type nanostructure based on multiple micellar structures [174]. First, the micelle is based on H30-PCL as the core, which holds both IR780 and camptothecin (CPT), and serves as the base for the positively charged helical PPI chains forming the corona. As a surface modification, terminal alkynyl-modified guanidinium groups were added to the PPI chains to increase penetration efficiency. Second, multiple of these micelles are entangled within PEI(−COOH/FA) chains to form the negatively-charged nanostructure. The working mechanism is dependent on the presence of an acidic TME as this will induce a charge inversion, subsequently causing micellar release from nanostructure. In vivo PA and US visualization of the CPT/IR780@ H30-PCL-PPI(L −)/PEI(−COOH/FA) nanostructure showed that intratumoral deposition gradually increases over time, reaching the maximum value approximately 24 h post-injection. Subsequent application of NIR irradiation allows for chemo-photothermal synergistic therapy. Performance studies showed that treatment efficacy is dependent on the heat-triggered drug release in combination with the photothermal properties, as the animals treated without a drug or irradiation did not show complete inhibition of tumor growth and also no improvement in survival.

The exploitation of the acidic tumor environment for triggered drug release is a refined strategy. However, this does not necessarily mean that the micelle has to be the theranostic carrier. Wang et al. have designed a treatment strategy, in which the cationic micelle acts as a catalyst for Phe-BF$_3$-mediated desilylation of the drug carrier [175]. The PEO$_{45}$-*b*-PC7A$_5$-*b*-PBA$_{25}$ (PC7BA) micelles shift from a neutral to positive-charge when the environmental pH changes from 7.4 to 6.5. In this study, *tert*-Butyldiphenylsilyl (TBDPS) forms the cage around the theranostic cargo hydroxyl camptothecin. The decaging reaction is locally induced by the presence of Phe-BF$_3$, and elevated to a higher efficiency by micellar catalysis, resulting in a significant decrease in tumor volume in comparison to the other study arms. Another multifunctional micellar-based nanosystem dependent on activation are the brush-arm star polymer (BASP) structures by Nguyen et al. [176]. The BASPs are small, polymeric particles consisting of branched macromonomers (MMs). In this study, these MMs host either pro-ORCAs for MR imaging or pro-drugs through cleavable linkers. Fluorophores are also connected to the MMs, but fluorescence will remain stable as these are conjugated through non-cleavable linkers. Upon cleavage through external or endogenous triggers, the pro-ORCA relaxivity will drop, resulting in a decrease in MR con-

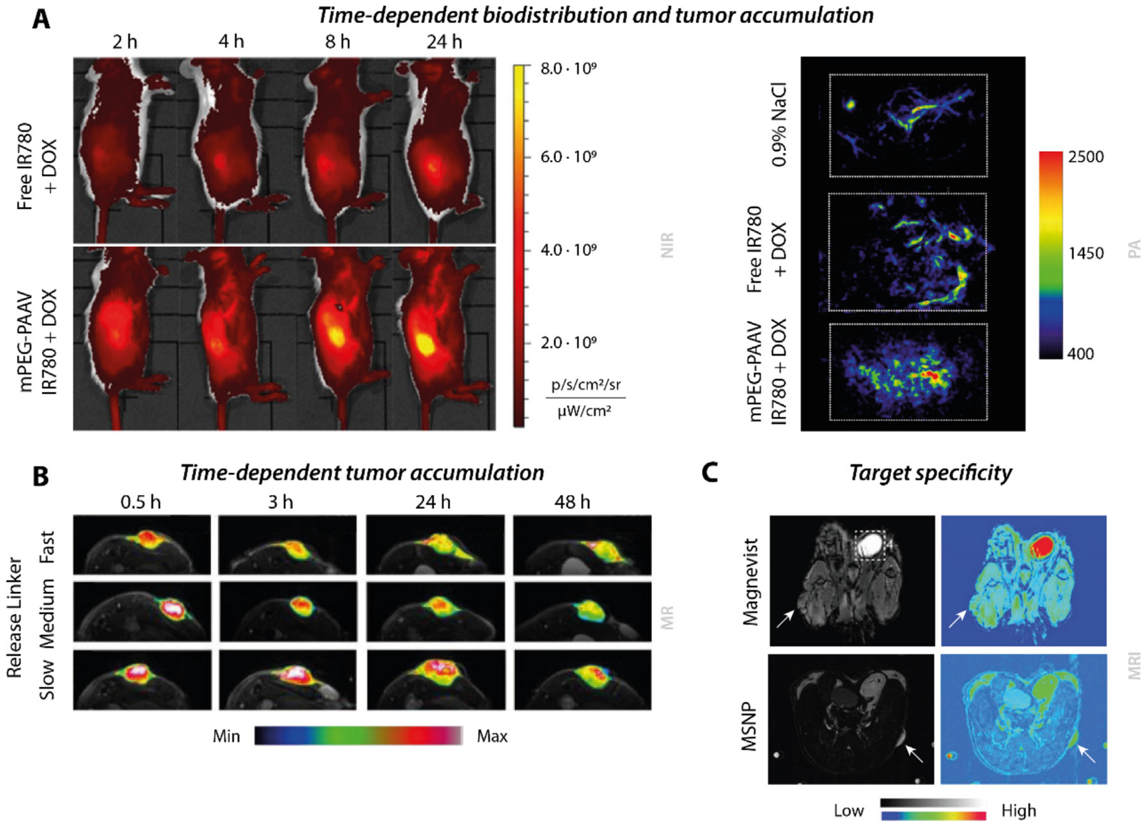

Fig. 4. In vivo imaging of micelles. **A**) Yang et al. demonstrated improved tumor-specific targeting of DOX-loaded micelles in comparison to administration of free agents [171]. (Left) The IR780 fluorescence signal increased gradually over time with peak intensity visible at 24 h post-injection. (Right) This intratumoral increase was also observed through photoacoustic imaging at 24 h post-injection, demonstrating a 1.5-fold increase in PA signal intensity in comparison to free theranostics. **B**) Nguyen et al. used false-color inverted T$_2$-weighted MR images to confirm intratumoral drug release using a micellar carrier based on either a slow, medium, of fast cleavable linker. As pro-drug activation is correlated to a decrease in MR contrast, these inverted images demonstrate effective intratumoral drug delivery within 24 h for the fast cleavable linker [176]. **C**) Yi et al. compared the contrast enhancement efficacy of a Pluronic-based cloaked micelle with a Magnevist® control [178]. The T$_1$-weighted MR- and corresponding pseudo color images of the tumor-bearing mice showed distinct differences in target specificity. At 30 min after administration, the control showed widespread enhancement with high signal intensity from the bladder (dotted box) and insignificant intensity from the tumor (white arrow). In contrast, the cloaked micelle showed high signal intensity within the tumor (white arrow) and limited signal from other tissues. Adapted with permission from [171,176,178].

trast. Simultaneously, cleavage of the pro-drug will result in a shift towards the therapeutically active agent. Therefore, a change in MR signal can be correlated with pro-drug activation (Fig. 4B). T_2-weighted images revealed that there is a time-dependent decrease in contrast enhancement. However, the fluorescent signal from the non-cleavable BASP remains constant, indicating that these nanosystems remain within the tumor-environment.

As mentioned in section 4.1.2., Pluronic® micelles are composed of a well-studied tri-block copolymer. While various Pluronic® micelles are currently tested in clinical trials, more advanced, experimental approaches based on Pluronic® micelles are developed in preclinical studies [78,177]. Cell membrane-coating nanotechnology has gained increased attention as a manner to improve tumor treatment. These systems are based on a synthetic nanoparticle as the core and an outer layer composed of natural cell membranes. Due to the biomimetic properties, these nanosystems are able to evade the immune system and the presence of negatively charged cell membranes on the outer surface, resulting in high tumor selectivity. For instance, Yi et al. have designed a smart, multilayered, biomimetic platform for targeted MRI visualization [178]. Self-assembled $NaGdF_4$-$CaCO_3$ nanoconjugates are known for being sensitive to the acidic tumor environment, which will result in disintegration of the complex and eventually shortening of the longitudinal relaxation time [179]. Encapsulation of these nanoconjugates within Pluronic® F127 was further improved by cell membrane cloaking, resulting in membrane-coated self-assembled nanoparticles (MSNP). Subsequent in vivo administration showed distinct differences in target specificity of this nanosystem in comparison to the control Magnevist® (Fig. 4C). T_1-weighted MR images of the control at 30 min post-injection showed contrast enhancement throughout multiple tissues with high signal intensity from the bladder, indicating fast renal clearance. In contrast, the cloaked nanosystem showed high signal intensity from the tumor with limited signal intensity from other tissues at the same time point.

A similar biomimetic platform was designed by Wang et al. with the intent to treat brain metastatic tumors [180]. A critical limitation for the treatment of these tumors is the presence of the blood–brain-barrier (BBB). However, as tumor cells are able to cross the BBB, their membranes may play a key role in metastatic establishment and progression. The core of this nanocarrier is based on polycaprolactone (PCL) and Pluronic® copolymer F68, and loaded with ICG as imaging- and photothermal agent. This synthetic core is camouflaged by a biocompatible shell, which is based on cancer cell membranes. In this study, nanosystems with melanoma (B16), mammary carcinoma (4 T1), or fibroblast-like (COS-7) membranes or without a shell were studied. The three biomimetic systems showed significantly slower in vivo blood clearance, with elimination times doubled (∼12 h) in comparison to the uncoated control (∼5h). While in healthy mice only the two cancer cell membrane-coated systems were able to traverse the BBB, in animals bearing a glioma with high proliferative activity all four nanosystems were able to enter the brain as shown by real-time fluorescence imaging. This can be attributed to the severely disrupted BBB associated with the rapid tumor growth. Peak intensity values were reached 8 h post-injection, and accumulation was superior for the B16 and 4 T1-based nanosystems. Therefore, biologically-camouflaged nanosystems may be a helpful functionalization to further tailor micellar-based drug delivery.

6.3. Liposomes

6.3.1. Conventional- and stealth liposomes

Liposomes have been of great interest since being proposed as carriers of enzymes or drugs by Gregoriadis and Ryman in 1971 [181]. However, the first generation of this nanosystem was highly sensitive to splenic- and hepatic clearance upon introduction into the systemic circulation, limiting their therapeutic potential. Therefore surface functionalization such as PEGylation were implemented, resulting in significant enhancement of pharmacokinetics, mainly due to reduced RES recognition and increased accumulation at the target site [182]. Both conventional- and stealth liposomes have been studied for image-guided drug delivery purposes. For instance, direct labeling of Doxil® with the lipophilic tracer DiO enables visualization of liposomal distribution. Seynhaeve et al. observed Doxil®-DiO in response to low dose TNFα at tumor vessel level using intravital microscopy [183]. Vascular manipulation of the tumor model resulted in a significant increase in Doxil®-DiO extravasation into the tumor interstitium, yielding a 7.1 fold increase in signal intensity.

High-resolution imaging up to the microvasculature level can also be enabled by encapsulating gadolinium-based contrast agents within liposomes. This development can be attributed to an increase in blood pool residence time, subsequently resulting in clinically relevant levels of contrast enhancement at lower dosages [184,185]. Despite the ability to have real-time visualization at tissue level at multiple planes, most drug delivery studies combine MR contrast agents with whole body imaging to determine biodistribution and validate therapeutic efficacy. For instance, Xiao et al. designed conventional liposomes that were co-loaded with sorafenib (SF) and gadolinium, enabling precise monitoring of liposomal biodistribution using MR imaging at multiple time points [186]. In comparison to Magnevist®, the SF/Gd-liposome displayed higher signal enhancement in combination with longer imaging times. An important safety concern of liposomal gadolinium is the risk on toxicity. If the residence time of the gadolinium (III) chelates within the systemic circulation exceeds the timeframe of kinetic stability, this may result in decomplexation and subsequent Gd^{3+} deposition in tissues.

Another possible high-resolution strategy is the use of radiolabeled liposomes. A distinction can be made between either incorporating radiolabeled drugs, radiolabeling a carrier either on the surface or within the lipid bilayer, or a combination of these two [187,188]. Implementing a dual-labelled nanosystems allows for tumor monitoring and drug uptake quantification using two different imaging modalities. Lamichhane et al. developed a dual-tracer imaging strategy implementing ^{111}In-labeled PEGylated liposomes, which encapsulate an ^{18}F-labeled carboplatin drug derivative [189]. While a similar in vivo radioactivity pattern was observed, a clear distinction can be made between SPECT-based liposomal biodistribution and PET-based drug accumulation over time. Nuclear imaging does provide high spatial resolution and good sensitivity, however the presence of ionizing radiation and possibility of tracer scattering due to liposomal degradation should be taken into account [52,190].

6.3.2. Stimuli-responsive liposomes

The shift towards smart drug delivery systems has gone through tremendous development for both experimental and clinical application since the introduction of thermosensitive liposomes by Yatvin in 1978 [191]. Currently, there are various strategies to induce stimuli-responsive drug release from liposomes, such as pH, light, and heat [12]. The light-sensitive, or photo-triggered liposomes show potential for enhanced drug delivery, as exposure to a non-invasive trigger can cause rapid destabilization of the lipid bilayer without negatively affecting the surrounding tissue. Implementation of photo-switchable agents, with specific absorbance wavelengths, within the lipid bilayer will catalyze the on-demand drug delivery. Chander et al. designed novel light-sensitive liposomes with in mind that these should mimic the composition and properties of clinically approved liposomes [192]. Therefore, the focus was on the use of saturated lipids that contain a choline headgroup at equimolar levels, and the use of cholesterol as the primary lipid. The photoactivatable liposomes were synthesized based on the self-assembly of DSPC, cholesterol, and UV- or red-light phosphatidylcholine analogs (AzoPC) with DOX loading. The pharmacokinetics of the nanosystem were assessed in vivo in transgenic zebrafish. At 2 h post-injection, the liposome were present throughout the systemic circulation without signals of clustering. At 24 h after administration, significant extravasation into surrounding tissue and accumulation was visible. Light exposure demonstrated a significant increase in DOX release from liposomes functionalized with either of the AzoPC analogues.

While in theory it could be a good idea to mimic the composition of clinically approved formulations and only make minor alterations, the practical application could be completely contradictory. Miranda et al. reported that liposomes composed of saturated lipids showed improved cargo retention stability in serum, but relatively slow release despite NIR laser exposure. Therefore, a novel design based on a mix of (un)saturated lipids, which allow for fast light-triggered release and good serum stability, with accelerated release due to the inclusion of porphyrin-phospholipid (POP) was proposed [193]. These POP liposomes contained three hydrophilic agents; sulforhodamine B (SRB), Magnevist®, and oxaliplatin. In order to study the liposome behavior within tumors based on light exposure, a bilateral tumor model was established with similar tumor volumes. While one side was exposed to irradiation (665 nm, 0.3 W/cm^2, 30 min) at 10 min post-injection, the contralateral tumor was shielded to minimize light exposure. The long exposure time was selected to account for light attenuation in tissues. Whole animal fluorescence imaging showed a rapid increase in fluorescence, indicating SRB release and unquenching, but only within the tumor exposed to light. Within 2 h after exposure, a decrease in fluorescence was observed, which can be attributed to rapid drainage. Strikingly, light exposure of the contralateral tumor at 24 h post-injection also resulted in a significant increase in fluorescent signal. This indicates that POP liposomes were able to accumulate and reside within the tumor, but more importantly, also maintained their cargo without significant leakage. In addition, contralateral tumors showed more persistent fluorescence, even up to 6 h after exposure, indicating delayed drainage. Animals receiving POP liposomes and delayed laser treatment did initially show a significant decrease in tumor volume, however fast tumor growth re-established after one week.

Despite the promising features of light-sensitive liposomes, requiring a simple trigger to catalyze liposomal drug release, the main focus of preclinical studies are the development of thermosensitive liposomes. Both liposome types are dependent on a similar, non-invasive stimulus, however the in vivo application of heat is able to enhance extravasation from tumor vasculature and simultaneously induce drug release from the nanosystem. There are various preclinical strategies to induce heat-triggered drug release, which are dependent on the research question, the location of the tumor, and the resources [121]. For the duration, studies on thermo-chemotherapy have shown that it is more beneficial to apply mild hyperthermia (40–42 °C) for 30–60 min in order to achieve maximal treatment outcome [194]. Applying higher temperatures for a shorter period of time is more prone to side effects such as vascular stasis, erythema of hemorrhagic necrosis [121].

For instance, Li et al. designed DPPC/DSPC/DSPE-PEG$_{2000}$ liposomes for the evaluation of DOX release [37]. In order to visualize heat-triggered drug release, the tumor was developed within a dorsal skinfold window, which allowed for simultaneous heating and confocal imaging. The use of a transgenic animal allows for facile distinguishing between the green vascular endothelial cells and the red doxorubicin autofluorescence. During heat application (42 °C, 1 h) triggered drug release was marginally visible at physiological temperatures up to 40 °C, with maximum fluorescence observed at 42 °C (Fig. 5A). After exposure, when the intratumoral temperature returned to baseline, the nuclear buildup of DOX is clearly visible. Animals treated with DOX-TSL and 42 °C showed significantly improved tumor growth control in comparison to the controls. However, as treatment did not completely eradicate the tumor, tumor regrowth was visible from day 16. Motamarry et al. employed DPPC/MSPC/DSPE-PEG$_{2000}$ liposomes for Doxorubicin delivery in subcutaneous tumors [195]. Heating (43 °C, 15-30-60 min) was applied through an external miniature hyperthermia probe, which allowed for unobstructed imaging of the tumor region. Drug release monitoring through fluorescence imaging showed that signal intensity kept increasing during heat exposure. However, discontinuation of the heat was pursued by rapid decrease of the signal, which is related to the wash-out of free, unbound Dox. In comparison to unheated control tumors, heated tumors demonstrated an 4.6-fold (15 min HT), 9.3-fold (30 min HT), and 13.2-fold (60 min HT) increase in signal intensity at 5 min after HT treatment (Fig. 5B). Subsequent analysis confirmed a strong, linear correlation between the observed fluorescence intensity and DOX tissue concentration, indicating the effectiveness of this heat-mediated treatment strategy.

Of all the heating techniques, MR-guided HIFU seems to be the most controlled manner for image-guided drug delivery [121,196]. Prior to TSL administration, treatment planning and temperature mapping can be performed in order to accurately determine the region of interest for HIFU application. In addition, MR-thermometry can be applied simultaneously to determine the intratumoral temperature in real-time [197,198]. Centelles et al. designed dual-labelled LTSLs to confirm hyperthermia-mediated drug delivery using both NIRF and MRI [39]. Full body images of the animals were captured at several time points after LTSL administration to trace the intrinsic fluorescence of the encapsulated drug, topotecan, and the second NIRF label, the lipid XL-750.DSA. Both agents showed co-localization within the tumor region 10 min after hyperthermia application. The liposomal distribution visible in the T$_1$-weighted MR images corresponded to the NIRF observations. However, in this study there is no question of image-guided drug delivery, as HIFU was applied independent of real-time spatio-temporal information. The HIFU protocol was based on initial distribution studies, which showed that in absence of hyperthermia, liposomal accumulation was most optimal between 10 and 45 min. In addition, MR imaging was only applied once, more than 2 h after HIFU application, and in this case the administered liposomes did not contain topotecan in order to minimize the risk of toxicity-induced MR changes. In similar work, Amrahli et al. continued to build on this set-up of HIFU-triggered release with both NIRF and MR imaging, but made some significant changes [199]. Several preliminary studies were performed in order to optimize the design of the HIFU protocol specific to the animal model. First, T$_1$-weighted images were acquired before and after LTSL administration without hyperthermia application to confirm the timespan for optimal intratumoral accumulation. As the presence of Gd-DOTA instigates a decrease of the T$_1$ value at the region of interest, a change in MR signal could be a reliable and quantifiable indicator for initiation of hyperthermia application. However, it should be noted that T$_1$ values may vary within a region of interest, owing to high tissue heterogeneity. The images demonstrated that intratumoral accumulation of LTSL occurred relatively rapid and persisted for at least 5 h after administration (Fig. 5C). Pharmacokinetic profiling elucidated that LTSL blood clearance was significant after 1 h and that LTSL presence was limited after 3 h. Therefore, this narrows the protocol down to HIFU application within 60 min to balance sufficient intratumoral accumulation and limited clearance. In the dual-tumor study, NIRF imaging of the animals bearing double tumors indicated that LTSL application benefits from HIFU-induced hyperthermia before and after LTSL administration. Both nanoparticle distribution and tumor uptake was significantly increased when the tumor was exposed to HIFU treatment in comparison to the untreated counterpart (Fig. 5D). This study shows that for preclinical treatment in a subcutaneous tumor, two short (≤5 min) periods of HIFU hyperthermia (43 °C) in combination with LTSL-DOX are sufficient to effectively increase intratumoral drug delivery.

Opposed to MR imaging in preliminary studies or only after hyperthermia application, De Smet et al. incorporated MRI scans at multiple time points during treatment [200]. T_2-weighted images were acquired before TSL administration and immediately after each HIFU treatment. Although both autoradiography and histology on tumor slices confirmed improved TSL distribution within the tumor, hyperthermia application did not significantly improve intratumoral accumulation immediately after HIFU treatment. However, after 48 h there is an overlap in the autoradiography-, histological- and fluorescence images, confirming treatment efficacy and thereby suggesting that HT-augmented EPR played a pivotal role in this study. The limited tumor response immediately after thermal treatment could be attributed to the set-up, as there is major heat loss due to the small size of the treatment cell in comparison to tumor volume (85 vs 500 mm^3) and gradual heat distribution to muscle tissue adjacent to the tumor.

While all of the above-mentioned studies do incorporate an imaging modality to follow intratumoral accumulation, there is no question of image-guided drug delivery. The most optimal manner of IGDD including MRI would be by having a continuous observation of temporal and spatial patterns of drug delivery. Ponce

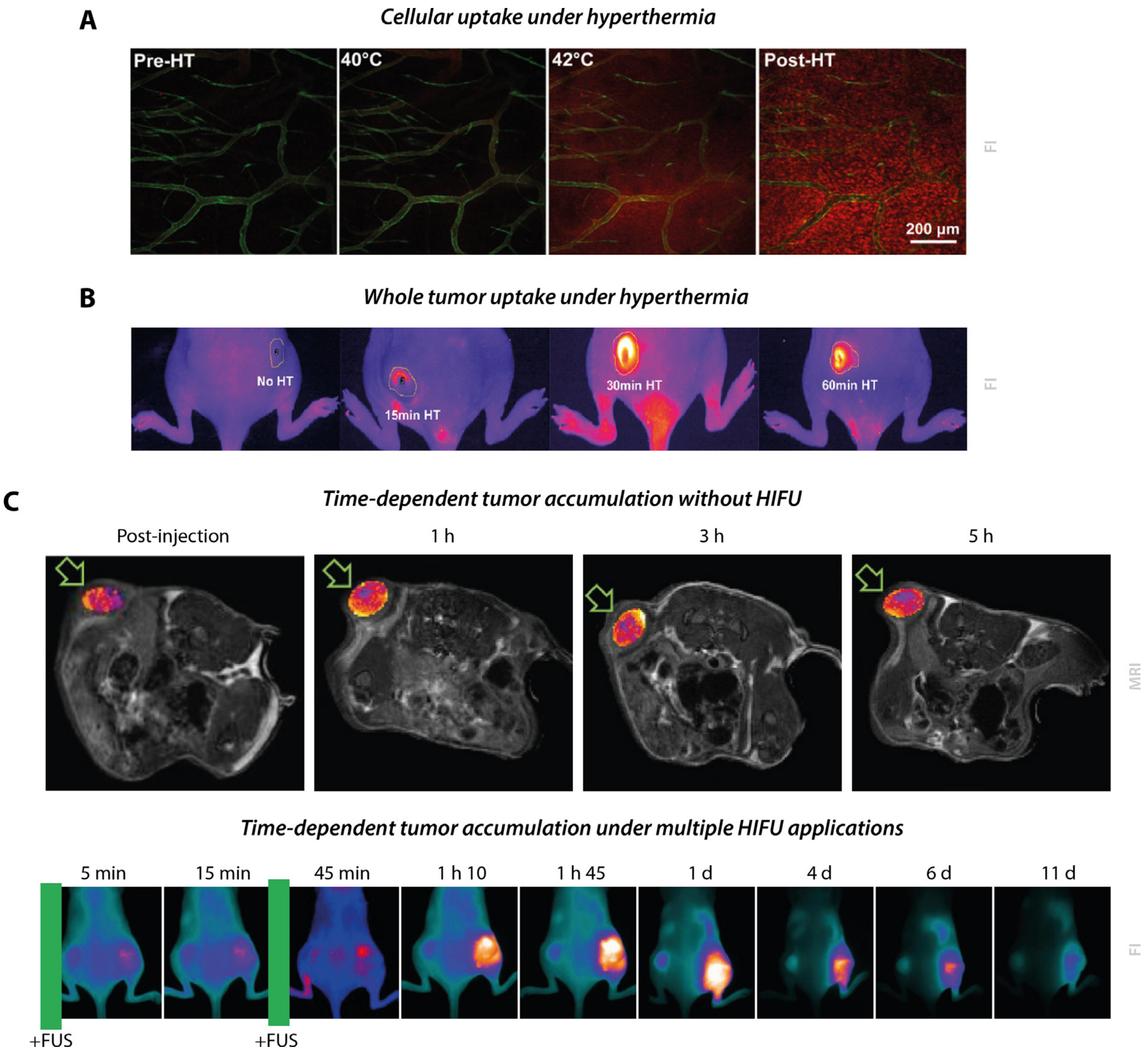

Fig. 5. In vivo imaging of liposomes. **A**) Li et al. evaluated heat-triggered release from DOX-LTSL at tissue level through confocal imaging [37]. At physiological temperature, little to no fluorescence signal is visible. Heat application immediately induces significant drug release, as shown by the homogeneous fluorescent signal. Discontinuation of heat application results in a more specific fluorescent signal, which shows nuclear uptake of Doxorubicin. **B**) Motamarry et al. demonstrated the effectiveness of heat-triggered drug release based on an external heat source [195]. Fluorescence imaging before, during, and after showed an initial rapid increase in fluorescent signal upon heat application. Tumor imaging after a 5-minute cool-down period clearly showed correlation between signal intensity and duration of the heating time. **C**) Amrahli et al. investigated HIFU-triggered release from thermosensitive liposomes with fluorescence and MR-imaging [199]. (Top) T_1-weighted images showed that intratumoral accumulation of the liposome formulation occurred relatively rapid, and persisted for at least 5 h post-injection. (Bottom) NIRF imaging of the dual tumor-bearing animals illustrate the benefit of HIFU application based on fluorescence. The left, untreated tumor showed minimal changes in fluorescence signal over the study period. The right, HIFU-treated tumor showed immediate response upon heat exposure, and allowed for accumulation to a larger extent than the control. Adapted with permission from [37,195,199].

et al. captured full sets of MR images over the full treatment period of 75 min [17]. Administration of DOX-LTSLs containing manganese provides the ability to observe triggered release within the tumor, as free manganese enhances contrast within the tumor. Subsequently, the obtained MRI data was used to calculate intratumoral doxorubicin concentrations. However, this method assumes co-localization of manganese and doxorubicin after liposomes release. While the magnetic resonance movies remained stable at the region of interest for 30 min, this phenomenon may be contributed to tissue binding of free manganese.

6.4. Carbon nanotubes

There has been a large interest in carbon nanotubes for both cancer diagnosis and -treatment [104,201]. Both the strong intrinsic fluorescent signal and the large surface area of the nanosystem, which is highly suitable for theranostic functionalization, contribute to the attractiveness of this nanosystem.

6.4.1. SWNTs

Functionalization with RGD peptide ligands is a commonly applied strategy for tumor-specific targeting of CNTs. Liu et al. designed multiple SWNT formulations, based on the presence of PEG with different chain lengths and RGD [202]. The PEG chain length appeared to be of high importance, as microPET scans revealed that SWNT functionalized with long PEG chains (5400) displayed decreased liver uptake and increased circulation time in comparison to SWNTs with short PEG chains (2000). In this study, the in vivo SWNT affinity for tumors with high and low $\alpha_v\beta_3$ expression was visualized through microPET imaging. RGD-functionalization of SWNT-PEG proved to be essential for therapeutic efficacy, as animals treatment with SWNT–PEG_{5400}–RGD did not only display decreased liver uptake, but also increased tumor accumulation in comparison to both untargeted SWNT-PEG formulations and SWNT–PEG_{2000}–RGD. In addition, the low $\alpha_v\beta_3$ tumor showed only limited SWNT–PEG_{5400}–RGD uptake. As the signal of these ^{64}Cu labelled SWNT-PEG-RGDs remained up to 24 h after administration, this suggests slow elimination and may result in undesired long-term radioactivity. In order to avoid radioactive side effects, Welsher et al. showed that the intrinsic NIRF characteristics can also be employed to visualize tumor vessels through murine skin at high-resolution (Fig. 6A) [203]. SWNT–PEG_{5000}–RGD were synthesized by surfactant exchange, which resulted in bright, biocompatible SWNTs. These nanosystems showed enhanced contrast despite administration of a 15-fold lower dose in comparison to SWNTs produced via direct sonication synthesis. On both whole animal- and tumor vessel level (λ = 1100 – 1700 nm), the SWNTs displayed clear NIRF signals with good tissue penetration and low autofluorescence, resulting in distinct images of the (tumor) vasculature. That same group also employed SWNTs for dynamic contrast-enhanced imaging, which allows for fluorescence imaging at anatomical resolution through time series over a short period of time (Fig. 6B) [204]. The principal component analysis turns pixels into groups based on their variance, thus discriminating based on the SWNT fluorescent signal as it travels through blood circulation. This results in a positive- and a negative group based on time [205]. After SWNT administration in a healthy animal, the oxygen-poor blood first circulates to the heart and lungs to be oxygenated, which is evident by the high contrast in the lungs [204]. Subsequently, the NIRF signal intensity fades, indicating further spread throughout the entire system. Almost simultaneously, peak value can be observed within high-vascularized kidneys. Within seconds the renal value decreases to the mean signal, which will remain constant throughout the entire body, indicating that the administered SWNTs have completed their first circulation time. In a tumor-bearing animal, the SWNTs follow a similar path, with the exception that the intratumoral pixel intensity was delayed in comparison to the major organs [205]. This can be credited to a delayed blood flow into the tumor due to the chaotic vessel growth. At 8 s after administration, the intratumoral fluorescent intensity appeared and increased further over time. As the tumor region showed both positive- and negative pixels, the overlay image is able to clearly distinguish the vasculature (positive) and the tumor outline (negative). However, for this technique, increased signal intensity does not automatically indicate accumulation and retention, but could be attributed to high vascularized organs or temporary extravasation of the nanosystem.

In addition to NIRF and PET, functionalized SWNT–PEG–RGD can also be employed to improve photoacoustic detection. De la Zerda et al. compared SWNT-PEG_{5000} with and without RGD functionalization to visualize nanosystem targeting to an $\alpha_v\beta_3$-positive tumor using three-dimensional ultrasound and photoacoustic imaging [109]. The subtracted PA images revealed that functionalized SWNTs displayed an 8-fold increase in the intratumoral photoacoustic signal, which remained consistent throughout the 4 h study period (Fig. 6C). This is in contrast to plain SWNTS, which demonstrated only a temporary intratumoral signal highly influenced by the presence of a neighboring large vessel.

6.4.2. MWNTs

Functionalization with multiple tumor-homing agents could even further improve anti-cancer treatment. For instance, Su et al. have designed a dual-targeting and co-delivery system based on a MWNT for lung cancer treatment [206]. The MWNT skeleton is connected to peptide ligand iRGD and plasmid pAT_2. iRGD is linked to the nanosystem via PEI, in order to improve the biocompatibility of the nanosystem. Candesartan (CaD), a therapeutic and targeting ligand, is conjugated to the skeleton via disulfide bonds, which is cleaved upon entering the tumor environment. Therefore, upon in vivo administration, the nanosystem specifically targets the tumor via the dual surface functionalization in the form of iRGD and CaD. After intratumoral accumulation, recognition through the receptor-mediated binding will lead to internalization in both tumor- and vascular endothelial cells. Upon presence in the tumor reducing environment, cleavage of disulfide bonds will initiate the release of CaD, resulting in synergistic downregulation of the AT_1R and AT_2R signal pathway resulting in anti-tumor effect. In vivo targeting studies revealed that injection of nanosystems containing either CaD or iRGD revealed a 1.88 and 2.41-fold increase in fluorescent signal at the tumor site in comparison to plain MWNTs. The iRGD-PEI-MWNT/pAT_2 nanosystems showed a significantly stronger fluorescence intensity in the tumor than in the liver, which could be attributed to the tumor-specific targeting of the $\alpha_v\beta_3$-receptor (Fig. 6D). Nanosystems containing both iRGD and CaD showed a 3.39-fold intratumoral increase and a 73.41 % hepatic reduction in comparison to the control group. Therefore, combination of these two high-affinity ligands result in synergistic tumor targeting and successful co-delivery.

Despite strong visualization and improved targeting efficacy, the application of an external facilitator seems to be required in order to completely eradicate a tumor with CNT-based treatments. Hu et al. designed MWNTs for dual-modal imaging with tumor-targeting via the ligand folic acid (FA)[207]. The nanosystem was covalently conjugated with PEI, which forms the anchor for modification with FA, the fluorescein FITC, and surface carboxylation of the excess PEI branch through SAH. Incorporation of ICG is beneficial for localized tumor treatment through PDT and PTT application. Both whole animal fluorescence- and photoacoustic imaging confirmed the tumor-homing properties of the FA-modified MWCNT complexes, demonstrating increased intratumoral signal intensities. Subsequently, the tumor region was exposed to laser irradiation (808 nm, 1 W/cm^2, 5 min) at 1 h post-injection. Moni-

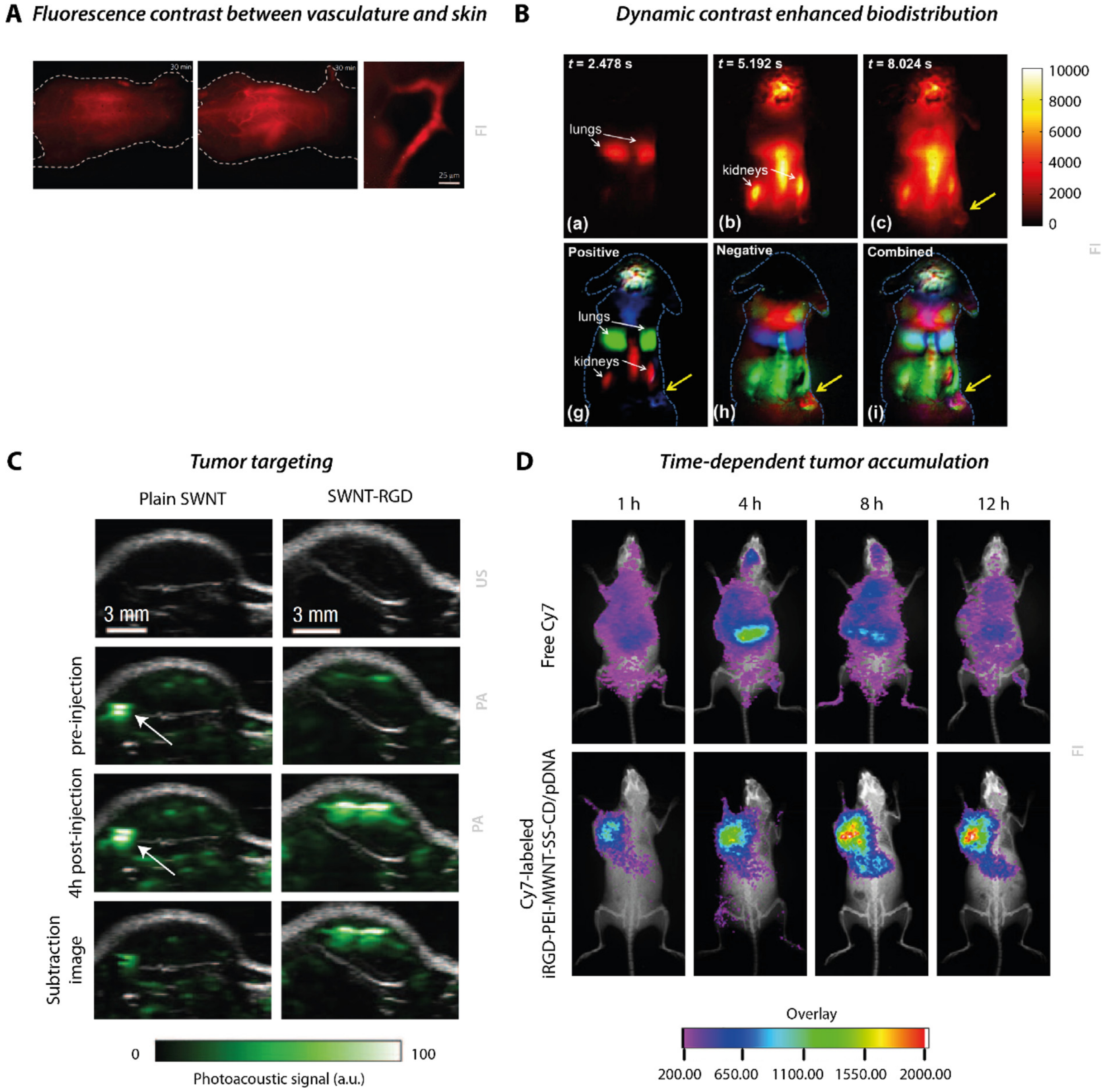

Fig. 6. In vivo imaging of single-walled carbon nanotubes (SWNTs). **A**) Welsher et al. used two SWNT formulations, based on a different synthesis route, which were both able to show high image contrast between the vasculature and skin [203]. Optical imaging using intravital microscopy demonstrated the ability of SWNT to visualize tumor vasculature at high magnification. **B**) Robinson et al. employed SWNTs for dynamic contrast-enhanced imaging, which allows for high-resolution biodistribution studies based on residence time [205]. Upon i.v. administration, initial high signal intensities are visible in the kidneys and lungs, with delayed intratumor distribution (yellow arrow). **C**) De la Zerda et al. employed RGD-functionalized SWNTs for enhanced tumor-targeting [109]. The intrinsic photoacoustic properties of the SWNTs were used to visualize the intratumoral accumulation. While functionalized SWNTs showed a significant intratumoral intensity, plain SWNTs demonstrated a high signal, which was not visible in the subtraction image (white arrow). This can be attributed to the presence of a large blood vessel, and does not indicate SWNT accumulation. **D**) Su et al. designed a dual-targeting multi-walled carbon nanotubes (MWNTs) sensitive to the tumor reducing environment [206]. While free Cy7 showed fluorescence distribution throughout the whole body, while temporary hepatic accumulation after 4 h, the functionalized MWNTs exhibited a time-dependent increase in fluorescent signal. Adapted with permission from [109,203,205,206]. (For interpretation of the references to color in this figure legend, the reader is referred to the web version of this article.)

toring through photothermal imaging revealed a significant increase in intratumoral temperature up to 57.8 °C. The PDT and PTT efficacy was undoubtedly visible by the naked eye, as the superficial tumor was completely cured 11 days post-treatment. This demonstrates that the MWCNT complexes exhibit excellent photostability and phototherapy, as animals treated with sole laser irradiation or sole administration of the MWCNT complex showed a ~ 20-fold increase in tumor volume at 24 days post-treatment.

6.5. Superparamagnetic iron oxide nanoparticles

SPIONS have demonstrated superior MR contrast properties due to the superparamagnetic properties of the iron oxide core. The size and biocompatible coating determine whether the SPION exhibits T_1- or T_2 relaxation. In general, SPIONS with ultrasmall size (<40 nm) exhibit T_1 contrast properties, while larger diameters result in T_2-weighted contrast enhancement [208,209].

6.5.1. Conventional superparamagnetic iron oxide nanoparticles

A multi-layered SPION was designed by Wang et al., based on a Fe_3O_4 core, a PPy shell, and functionalized by a layer of DOX and PEGylated outer layer [210]. The ultrasmall iron oxide nanoparticles had a diameter of 8–10 nm, assembling into nanoclusters with a size of approximately 50 nm, and therefore showed potential as a T_2 contrast agent. The strategy was to administer the SPION complexes via intratumoral injection, followed by immediate application of low power NIR laser irradiation (808 nm, 0.35 W/cm^2, 25 min). As the NIR irradiation induces mild photothermal heating, this could simultaneously promote internalization of the Fe_3O_4@PPy-PEG-DOX complex and triggered DOX release.

Whole animal thermographic imaging showed localized heating in the tumor region, reaching a sustained temperature of 44–45 °C within 20 min. In addition, the adjacent tissues demonstrated only a minor temperature increase to 35–36 °C within the same period. Mice treated with Fe_3O_4@PPy-PEG-DOX demonstrated ~ 88 % tumor growth inhibition in comparison to the control group. These results were confirmed by T_2-weighted imaging, which showed darkening of the tumor area after SPION administration. At day 7 post-treatment, a reduction in tumor size was evident for the animal receiving Fe_3O_4@PPy-PEG-DOX in combination with low power NIR laser irradiation (Fig. 7A). Administration of the same dose and treatment with a higher NIR laser power led to an intratumoral temperature of 48–49 °C. Mice treated with NIR laser irradiation and SPION without DOX did show a decrease in tumor volume over time. This is likely due to incomplete tumor ablation, as after 10 days tumor growth resumed. Animals treated with NIR laser irradiation and the Fe_3O_4@PPy-PEG-DOX complex exhibited complete eradication without loss of body weight.

6.5.2. Superparamagnetic iron oxide nanoparticle complexes

As part of a hybrid nanosystems, SPIONs can be used either internally or externally. For instance, Zheng et al. have designed a hybrid nanosystem based on the encapsulation of SPIONs within a sterically stabilized liposome (SSL) [211]. The pH-responsive peptide $H_7K(R_2)_2$ was used as a targeting ligand on the liposome, while PTX was encapsulated within the lipid bilayer, and SPIONs within the aqueous core. This resulted in a nanosystem with a mean size larger than 150 nm. Liposomal conjugation with the NIR dye DiR allowed for visualization of nanosystem tissue distribution. Mice receiving the DiR/SPIO-SSL-$H_7K(R_2)_2$ complex exhibited a strong fluorescent signal at the tumor site. This can be attributed to the $H_7K(R_2)_2$ activation in response to the acidic TME. In addition, the targeted complex exhibited an increased circulation time as intratumor signals could be observed up to 48 h. This in contrast to the DiR/SPIO-SSL controls, which showed a steep decrease in fluorescence already at the 4 h time point (Fig. 7B). The in vivo targeting effect was also confirmed through T_2-weighted MR imaging. At 30 min after administration, darkening of the tumor region was visible, indicative of PTX/SPIO-SSL-$H_7K(R_2)_2$ accumulation. This decrease in signal intensity remained steady up to 1.5 h post-injection. Administration of the control formulation did not induce a change in signal intensity. Animals receiving PTX/SPIO-SSL-$H_7K(R_2)_2$ did initially show tumor growth inhibition up to 90 % in comparison to the control. Despite the significant initial reduction, from day 25 an increase in tumor volume could be observed.

External use of SPIONS for enhanced tumor treatment was studied by Wang et al. [212] The center of the nano-assembly was based on a biotin-functionalized exosome, which contained doxorubicin. Surface functionalization of this exosome was performed through PDA-coated Fe_3O_4, which were decorated with avidin, a glycoprotein with a strong binding affinity for exosomal surface biotin, and a Cy5 molecular beacon [213]. This resulted in a nano-assembly with a mean size larger than 100 nm. Besides photothermal sensitivity, the PDA coating is also able to quench MB fluorescence. This is switched to an active form upon tumor cell internalization due to microRNA-21 (miR-21) recognition. Upon comparing tumor targeting of the Cy5-labelled exo-DOX-Fe_3O_4@PDA, the animals received an i.v. injection of the SPION complex with or without application of a continuous external magnetic field (MF) up to 48 h. Whole animal fluorescence imaging showed a significant intratumoral signal in the animals which were exposed to a magnetic field. This distinct signal was visible after 24 h, but most prominent at 48 h (Fig. 7C). This in contrast to the control group, which were not exposed to a magnetic field and demonstrated an uneven signal distribution with a proportional decrease in signal intensity over time. In correspondence with these results, the animals receiving the targeted nanosystem, continuous MF application, and subsequent NIR laser irradiation (808 nm, 1.0 W/cm^2, 3 min) at 48 h post-injection demonstrated the highest increase in intratumoral temperature (21.33 °C). This resulted in a 97.57 % reduction in tumor size in comparison to the control group after 31 days. Therefore, active magnetic targeting is able to steer and treat superficial tumors with high efficiency. However, all of the SPION formulations mentioned in this section displayed a mean size larger than 50 nm. As large SPIONs have the tendency to accumulate in the major organs, this results in persistent negative contrast at undesired locations. The development of ultrasmall SPIONs show potential due to the small size (<5 nm) and corresponding strong renal clearance [214]. Functionalization in form of zwitterionic SPIONs show the potential to even further improve contrast-enhanced MRI. Ma et al. designed ultrasmall, zwitterionic SPIONS with a size of ~ 3 nm for enhanced T_1-weighted MR imaging, showing potential for application in both rats and mice [215]. Evaluation of the tumor-targeting potential in mice showed that the Fe_3-O_4-PEG-Cys NPs displayed fast tumor accumulation, reaching peak values as soon as 45 min post-injection. The strong signal intensities remained throughout the 3 h imaging period. These results show the potential to convert this design into targeted drug-delivery nanosystems.

Another nice anti-cancer strategy, which technically is on the verge of IGDD, is combining SPIONS with stem cells for cell-based tumor treatment. Thin et al. have incubated Luciferase (Luc)-transfected adipocyte-derived stem cells (ADSCs) with ^{111}In-labelled SPIONs (ADSC-^{111}In-SPION) to obtain cells with tri-modal imaging properties [216]. As cellular-labelling with plain SPIONs may lead to “blooming” of the signal void, it is valuable to include another imaging moiety to obtain both structural and quantifiable information. In vivo distribution studies showed that the selected administration route is of high importance for the ADSC-^{111}In-SPION biodistribution. Multi-modal imaging revealed that intracardiac (i.c.) administration showed higher tumor uptake than i.v. administration 5 h post-injection (Fig. 7D).

6.6. Gold nanoparticles

A multitude of gold nanoparticle (GNP) geometries, such as nanoshells [217], nanorods [218], nanocages [9], and nanostars [219], have been studied in vivo. Without functionalization these nanosystems show potential to be employed for CT, PA, and thermal imaging. The main anti-tumor mechanism of GNPs is tumor cell internalization, followed by synergistic promotion of drug release and induction of apoptosis through photothermal effects.

6.6.1. Conventional gold nanoparticles

Due to the strong and tunable optical absorption, which can be attributed to surface plasmon resonance, AuNPs are suitable as a photoacoustic contrast agent [220]. Liu et al. visualized the tumor targeting potential of gold nano prisms through PA and FL imaging [221]. The nanosystem was functionalized through PEGylation and PD-L1 targeting, and incorporation of Ce6 gave both a fluorescent- and photosensitizer function. Photoacoustic imaging of the tumor region demonstrated an increase in signal intensity within 1 h post-injection, which increased linearly up to 24 h (Fig. 8A). As both fluorescent- and PA imaging confirmed enhanced tumor targeting, the GNPs@PEG/Ce6-P were subsequently exposed to NIR irradiation (633 nm, 0.8 W/cm^2, 20 min) at 24 h after i.v. administration. Thermal images demonstrated that NIR exposure led to induction of a hyperthermic intratumoral temperature (43.5 °C),

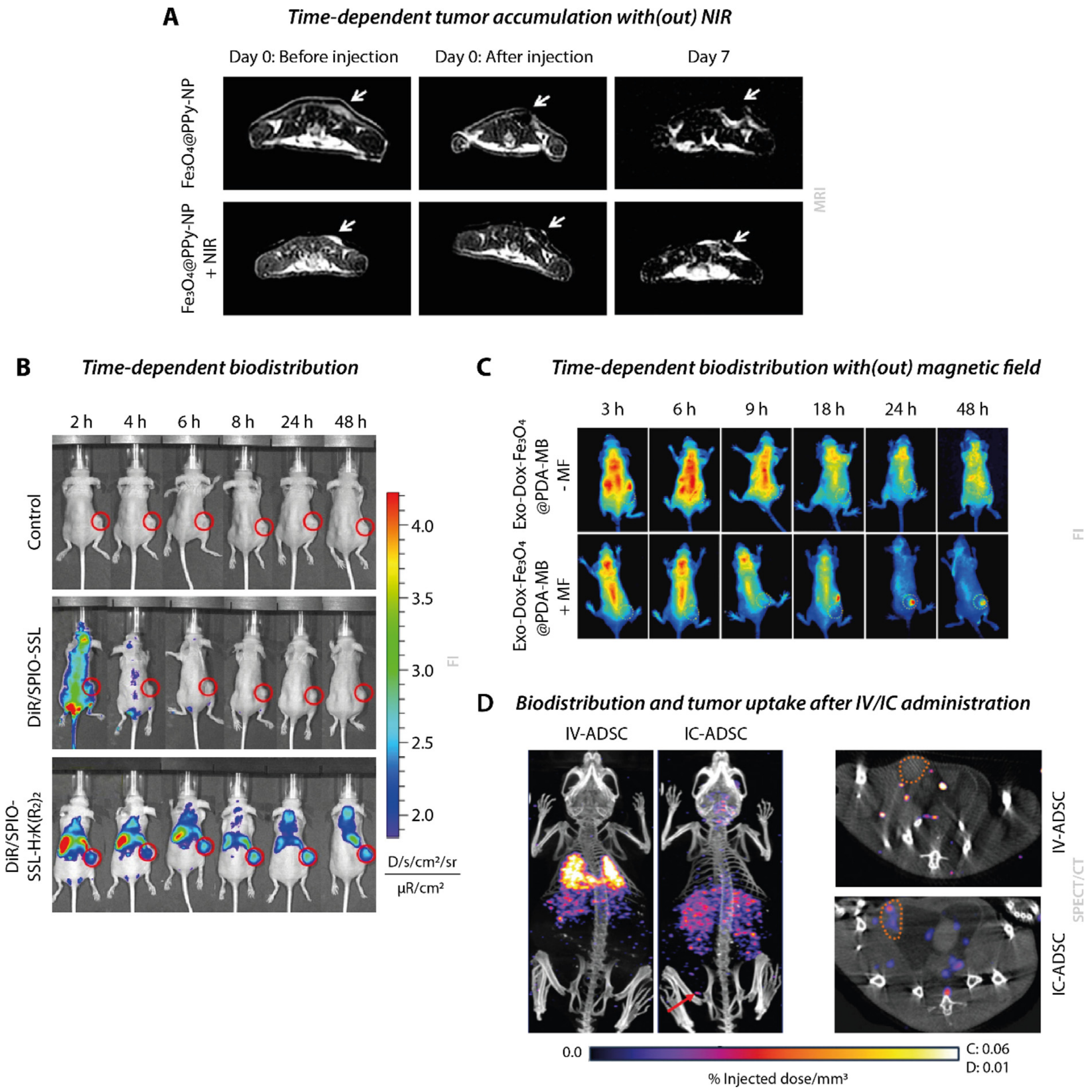

Fig. 7. In vivo imaging of superparamagnetic iron oxide nanoparticles (SPION). **A**) Wang et al. assessed tumor growth inhibition through T_2-weighted MR images [210]. Animals treated with the SPION formulation showed darkening of the tumor area after administration, indicating accumulation. Subsequent NIR irradiation of the tumor area showed a reduction in tumor size at day 7 post-treatment. **B**) Zheng et al. designed SPIONs with a pH-responsive peptide as a targeting ligand [211]. Comparing the biodistribution between the control, untargeted, and targeted formulation through fluorescence imaging showed differences in distribution and retention. While the untargeted SPION formulation shows a heterogeneous signal throughout the body, which disappeared within 4 h, the targeted formulation showed an increased circulation time and a high fluorescent signal from the tumor. **C**) Wang et al. visualized magnetic steering of a SPION formulation through fluorescence imaging [212]. Animals treated with only the specific SPION formulation exhibited long circulation times, but limited uptake in the tumor. Continuous exposure to an external magnetic field near the tumor resulted in a significantly higher uptake, as shown by the increased fluorescence signal after 48 h. **D**) Thin et al. incorporated SPIONS within stem cells for potential cell-based tumor treatment [216]. Comparison of the administration route through SPECT/CT demonstrated that intracardiac administration of the formulation resulted in a higher tumor uptake than intravenous administration in both coronal (left) and axial (right) images. Adapted with permission from [210–212,216].

which is distinct from the saline control (36.3 °C) and non-targeted gold nanoprisms (42.1 °C) (Fig. 8A). Despite the relative minor difference in temperature between the targeted and non-targeted gold nanoprisms, a significant difference between these groups in tumor volume was observed at day 25 post-treatment. This indicates more effective tumor growth inhibition by the GNPs@PEG/Ce6-P, though not a complete eradication of the tumor.

Similar results were obtained by Xu et al, although this study was based on porous gold nanoshells (PGNSs). Surface functionalization occurred through PEGylation and trastuzumab (HER) targeting, and the exterior was co-decorated with the drug DM1 [217]. Real-time treatment monitoring was achieved through multimodal imaging; CT, PA, and PT. After administration, CT imaging demonstrated enhanced tumor contrast up to 12 h for all three PGNS formulations. This in contrast to the control CT contrast agent iohexol, which did not exhibit any contrast enhancement at that time point (Fig. 8B). Photoacoustic imaging did show gradual enhanced brightness, which was maintained for up to 24 h after administration and was significant in comparison to the saline control for all time points. The intratumor temperature of the mPEG/HER-PGNSs group increased rapidly after NIR irradiation (808 nm, 3.0 W/cm^2, 5 min) at 24 h after i.v. administration. Ultimately reaching temperatures up to 45 °C at the 5-minute mark in compar0069son to 38 °C in the saline control. The average tumor volume over 20 days post-treatment confirmed the efficacy of the chemo-photothermal therapy, as the mPEG/HER-PGNSs group displayed a 39.47 % tumor growth inhibition rate in comparison to the DM1 only group and 83.9 % in comparison to the saline control group.

6.6.2. Gold nanoparticle complexes

The gold nanosystems do not necessarily have to be the main core component of a nanosystem. For instance, Li et al. designed a self-assembling, spherical nanostructure, which is based on a combination of ultra-small gold nanoparticles and trivalent gadolinium ions (Gd^{3+}) [222]. Functionalization of the nanosystem occurred through PEGylation, MMP-2 surface modification, and IR820 encapsulation. Dual-modal imaging of Gd-AuNPS@IR820 within tumor-bearing animals demonstrated a positive correlation between T_1-weighted MR- and whole-body fluorescence imaging. Signal intensity was initially observed in liver, which gradually weakened over time as the signal increased within the tumor region. At 12 h after nanosystem administration, intratumoral peak values were observed for both imaging modalities. Therefore, this time point was selected for application of NIR laser irradiation (808 nm, 0.8 W/cm^2, 3 min) for 2 rounds at 3 min intervals. Subsequent thermal imaging of the tumor showed that Gd-AuNPS@IR820 nanosystems induced the highest temperature increase (43.5 °C) (Fig. 8C). Over time, this resulted in effective tumor cell killing as shown by a decreased tumor volume and increased survival rate in comparison to the control groups.

Another study which exploited AuNP functionalization with MMP for tumor-targeting properties was performed by Yang et al. [223]. The main objective of this nanosystems was to enhance extracellular assembly within the TME in order to improve the absorption red-shift. This nanosystem carried both functionalization and therapeutic cargo on the AuNP surface. First, complementary DNA strands were attached, followed by DOX linking through thermolabile connections. Subsequent PEGylation formed a coating around the AuNP through peptide linkers with MMP ligands, resulting in PEG-pep-DOX-AuNPs. Upon i.v. injection, the nanosystem will remain monodisperse and exhibits improved circulation time due to their small size and PEGylation. However, upon entering the MMP-rich tumor tissues, cleavage of the shielding PEG layer exposes complementary DNA strands. This will drive rapid aggregation and accumulation within the TME. PET imaging through PEG-pep-DOX-AuNPs labelled with ^{64}Cu confirmed a maximum tumor uptake at 24 h post-injection, which was also demonstrated through PA imaging (Fig. 8D). The average tumor PA intensity for the nanosystems was increased by 1.74-fold in comparison to the MMP-inert controls. Subsequent NIR laser irradiation (808 nm, 1.0 W/cm^2, 10 min) and thermal imaging at 24 h post-injection did not only reveal a more rapid local temperature increase, but also a more homogeneous heating of the entire tumor region for animals treated with the PEG-pep-DOX-AuNPs. The tumor growth- and survival curves confirmed the synergistic anti-tumor effect of designed nanosystem with local laser irradiation. Interestingly, despite both being functionalized for tumor-specific targeting through MMP and similar in size (72.4 vs 73.2 nm), there is a difference in in vivo spatiotemporal characteristics and therapeutic outcome [222,223]. Both Gd-AuNPS@MMP2 and PEG-pep-DOX-AuNPs exhibit initial high signal intensity within the liver, but peak intratumoral accumulation was observed at different time points (12 h vs 24 h). In addition, there is also an observed difference in survival (day 15, 80 % vs 40 %). While this can also be attributed to differences in the NIR laser irradiation treatment, the tumor model (HCC-LM3 vs SCC-7), and DNA hybridization, it is valuable to see that same nanosystem base material and functionalization does not necessarily result in an effective treatment design.

The excellent PTT/PDT capabilities of gold nanoparticles can be even further improved with the design of heterostructued nanosystems. Yang et al. constructed such as system based on the hollow, mesoporous structure of Bi_2Se_3 with surface-deposited AuNPs [224]. This Bi_2Se_3/Au complex is able to act as a strong photothermal agent. In addition, interactions between BS and Au act as a photocatalyst, resulting in boosted conversion of TME molecules into cytotoxic ROS. The Bi_2Se_3/Au complex is able to induce strong CT contrast enhancement, which can be attributed to a combination of the high X-ray attenuation coefficient of gold and the high Z-element of bismuth. PLGA-PEG coating of the nanosystem complex to improve the biocompatibility and circulation time was followed by DOX encapsulation within the hollow Bi_2Se_3/Au complex. CT and thermal imaging of the BS/Au@PP-DOX complex revealed significant image brightness enhancement at 4 h post-injection. Subsequent NIR laser irradiation (808 nm, 1.0 W/cm^2, 10 min) induced a significant temperature increase in comparison to the BS control (22.1 °C vs 12.0 °C), resulting in intratumoral ablative temperatures. Complete tumor eradication was observed for the tumor-bearing animals receiving the BS/Au@PP-DOX complex with NIR laser irradiation at day 14. The strong tumor inhibition can be attributed to the synergistic therapeutic effect of initial tumor ablation, increased ROS production, and local doxorubicin release.

6.7. Mesoporous silica nanoparticles

As mentioned in section 4.2.4, MSN design can be categorized in ordered-, hollow, or rattle-type MSN. Plain hollow mesoporous organosilica nanoparticles (HMON) are subject to high drug leakage, due to weak adsorption of hydrophobic drugs in combination with the presence of small, superficial pores. Therefore, functionalization of HMONs should incorporate a manner to minimize drug leakage through the pores.

6.7.1. Conventional hollow mesoporous organosilica nanoparticles

Yang et al. designed HMPDINs@TP-SN38, which are small-sized hollow mesoporous organosilica nanoparticles with PEG_{2000}-PDI-silane hybridization [225]. Perylene diimide (PDI) is a thermosensitive polymer, which can be exploited for fluorescent-, and photoacoustic imaging and photothermal treatment. Co-hydrolysis of the HMON with the PEG_{2000}-PDI-silane molecule resulted in PDI polymer growth within the hollow interior, silica shell shielding, and extended PEG on the outer surface. The internal presence of PDI within the HMON did not only contribute to an increase in loading capacity, but also prevents undesired SN38 release. Evaluation of tumor accumulation showed consistent results for PA and FI, as increased intensities could be pick-up at the 1 h mark. The peak intensity was visible at 24 h post-injection, showing a 3.31 fold signal increase in comparison to 1 h post-injection (Fig. 9A). The synergistic therapeutic effect of the HMPDINs@TP-SN38 was evaluated by local NIR laser irradiation (671 nm, 0.5 W/cm^2, 5 min) at 24 h post-injection. This treatment induced controlled laser stimulation, reaching temperatures as high as 55 °C. Animals showed tumor ablation without recurrence, which was quantifiable in form of the prolonged survival rate in comparison to the control groups.

Another strategy to improve and retain drug encapsulation within MSNs is through surface decoration with small particles. Wu et al. have designed HMO nanoparticles for treatment of glioblastoma multiforme (GBM) [127]. Functionalization of the nanosystem occurred through functionalization with ultrasmall $Cu_{2-x}Se$ particles, which can be used as a contrast agent for PA imaging. In addition, the presence of these particles on the HMON

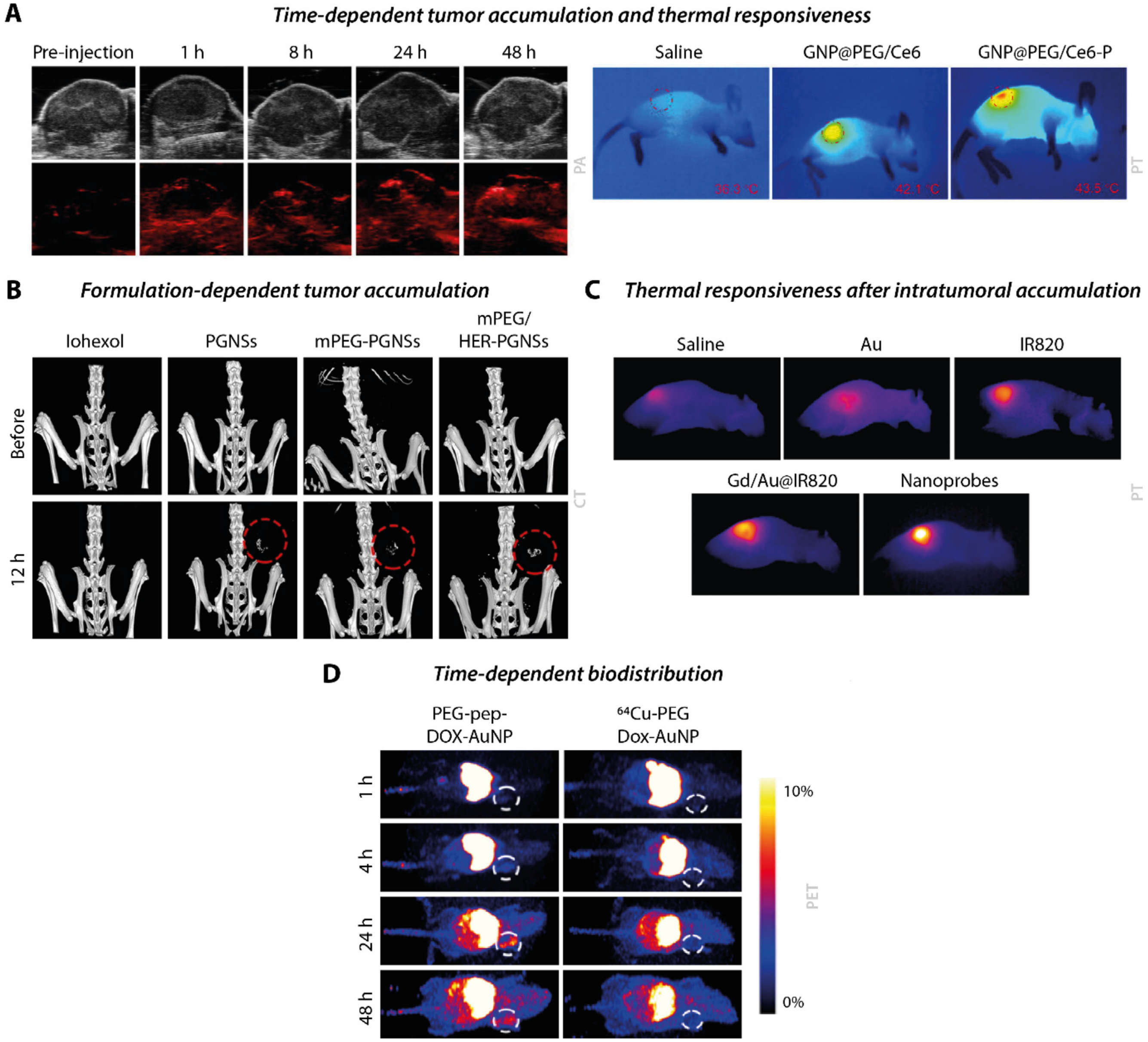

Fig. 8. In vivo imaging of gold nanoparticles (GNPs). **A**) Liu et al. visualized the treatment efficacy of functionalized gold nanoprisms through PA and thermal imaging [221]. (Left) Photoacoustic imaging of the tumor region showed a time-dependent increase in signal intensity. (Right) Exposing the tumor-bearing animal to NIR laser irradiation at 24 h post-injection resulted in the development of hyperthermic temperatures within the tumor region. **B**) Xu et al. used PEGylated, HER-targeted porous gold nanoshells (PGNSs) to deliver DM1 to s.c. tumors in the mammary fat pad [217]. Comparison of three different PGNSs formulations to the control CT contrast agent iohexol revealed that all PGNSs formulations demonstrated enhanced tumor contrast at 12 h after administration. This observation was in contrast to iohexol, which did not exhibit any signal at that time point. **C**) Li et al. designed self-assembling nanostructures based on ultra-small gold nanoparticles and trivalent gadolinium [222]. Comparing thermal responsiveness of saline, Au, IR820, untargeted (Gd/Au@IR820) and targeted (nanoprobe) formulation at time point 12 h showed significant differences in local temperature increase. **D**) Yang et al. developed a tumor-targeted gold nanoparticle formulation through peptide linking [223]. PET imaging of the tumor area indicated the efficacy of peptide linking, as a higher intratumoral signal was observed at each time point for the targeted formulation, exhibiting peak values at 24 h post-injection. Adapted with permission from [217,221–223].

surface also reduces the size pore size. The large, hollow interior of the nanosystem was subsequently exploited for encapsulation of doxorubicin. Multiple HMONs are able to develop a framework through disulfide linkers, which are also responsible for the Cu_{2-x}-Se connection on the outer shell. Therefore, within the tumor-reducing environment, biodegradation of DOX-HCu nanosystems will occur on two levels due to redox-responsive behavior. This will subsequently result in on-demand, tumor-specific DOX release. One of the hurdles for GBM treatment is the presence of the blood–brain-barrier. The use of focused ultrasound (FUS) has been shown to be an effective facilitator to induce openings within the BBB. Consecutive ultrasound- and photoacoustic imaging of the tumor region prior to administration only showed contrast from the blood vessels in the skin and skull. Significant intratumoral contrast enhancement is visible in the PA images of animals receiving HCu and FUS treatment. No obvious PA signals are visible in the control group, which did receive HCu but were not exposed to FUS. In order to assess intracranial biodistribution of the HCu nanosystem, ICG labelling was established through loading in the hollow interior. While the control group only showed minor fluorescence, which can be attributed to the presence of free ICG or nanoparticle diffusion through defective BBB, strong signal intensities were observed in animals treated with ICG-HCu/FUS.

These results suggest enhanced nanosystem delivery and -penetration as a result of FUS-mediated BBB disruption. Confocal imaging of ex vivo healthy brain tissue showed little to no fluorescent signal, which suggests that non-invasive, localized drug delivery can be induced with the use of HCu/FUS. FUS-mediated DOX delivery was studied through an intracranial brain tumor model based on luciferase-expressing tumor cells. At day 7 after tumor inoculation, all groups exhibited a similar bioluminescent intensity. Over time, the control groups receiving no treatment, only FUS, or only free DOX show increasing bioluminescent signal, indicating tumor growth. This is not observed in the DOX-HCu/FUS group, which exhibits a 91.1 % tumor growth inhibition at day 22 in comparison to the control group and an increased survival over the 60-day study period.

6.7.2. Stimuli-responsive hollow mesoporous organosilica nanoparticles

Tumor homeostasis and -development is largely orchestrated by the bidirectional communication between tumor cells and the micro-environment through soluble factors [226]. Therefore, a refined strategy could be the development of theranostic nanosystems susceptible to factors present within the TME, such as reactive oxygen species. High levels of endogenous ROS are present within tumor cells due to an imbalance between oxidants and anti-oxidants. In addition, external triggers such as PDT are also able to induce a substantial increase in exogenous ROS levels [227,228].

Rao et al. designed hollow MSNs, which exhibited drug release through ROS-responsive pore engineering [229]. These R-MSNs are based on the encapsulation of DOX within the hollow interior. In order to seal the mesopores, Gd-DOTA complexes were connected through aminoacrylate linkage, which are sensitive to cleavage by singlet oxygen. Therefore, during systemic circulation the DOX-R-MSN complex will remain stable. Upon reaching the TME, the presence of $^{1}O_2$ will initiate cleavage, resulting in a shift into opened mesopores. The DOX-R-MSN complex was decorated with PEG-conjugated Ce6 on the outer surface, which contribute to improved accumulation and enhanced ROS generation to catalyze intratumoral drug delivery. Whole-body fluorescence imaging showed that the R-MSN circulate throughout the entire body for a prolonged period of time. At 6 h post-injection, the peak fluorescent signal was observed within the tumor region. This signal remained constant for up to 24 h. T_1-weighted MR images confirmed intratumoral accumulation, indicating that the nanosystems remained stable under physiological conditions without loss of signal over time. Subsequent application of NIR laser irradiation (660 nm, 0.5 W/cm^2, 10 min) at 6 h after R-MSN administration confirmed the ability to induce PDT-maneuvered chemotherapy delivery, as animals receiving DOX-R-MSN demonstrated significant tumor inhibition with low systemic toxicity as shown by stable body weight.

6.7.3. Rattle-type mesoporous silica nanoparticles

An example of MSNs which require PDT-based ROS production for optimal therapeutic efficacy are the rattle-type MSNs designed by Feng et al. [230]. This nanosystem is based on a small Fe_3O_4-Au core, which allows for magnetic resonance (MR)- and micro-computed tomography (µCT) imaging, and a SiO_2 outer shell. Subsequently, the photosensitizer methylene blue was encapsulated within the MSN, and the outer surface was modified with P^{D}PPA-1, a MMP-2 cleavable peptide. Inclusion of this peptide is part of the immune checkpoint blockade (ICB) therapeutic activity. Upon entering the tumor region, micro-environment-responsive cleavage will convert P^{D}PPA-1 in free ^{D}PPA-1. This peptide is able to bind and block to the overexpressed programmed cell death ligand-1 (PD-L1) transmembrane protein, and therefore reduce the tumor-suppressive immune micro-environment through silencing of the checkpoint inhibitor PD-L1 [231]. Both µCT and MR imaging of the MB@MSP nanocarrier demonstrated that peak signal intensity within the tumor region was reached 8 h after i.v. administration (Fig. 9B). As signals were still visible after 48 h, this indicates that after accumulation the nanosystems will remain at the site. As ICB alone is not sufficient to completely inhibit metastatic development, combination with PDT may facilitate activation of the anti-tumor immune system. In order to study the nanosystems ability to treat metastatic tumors by combining ICB with PDT, a bilateral tumor model was established with significant

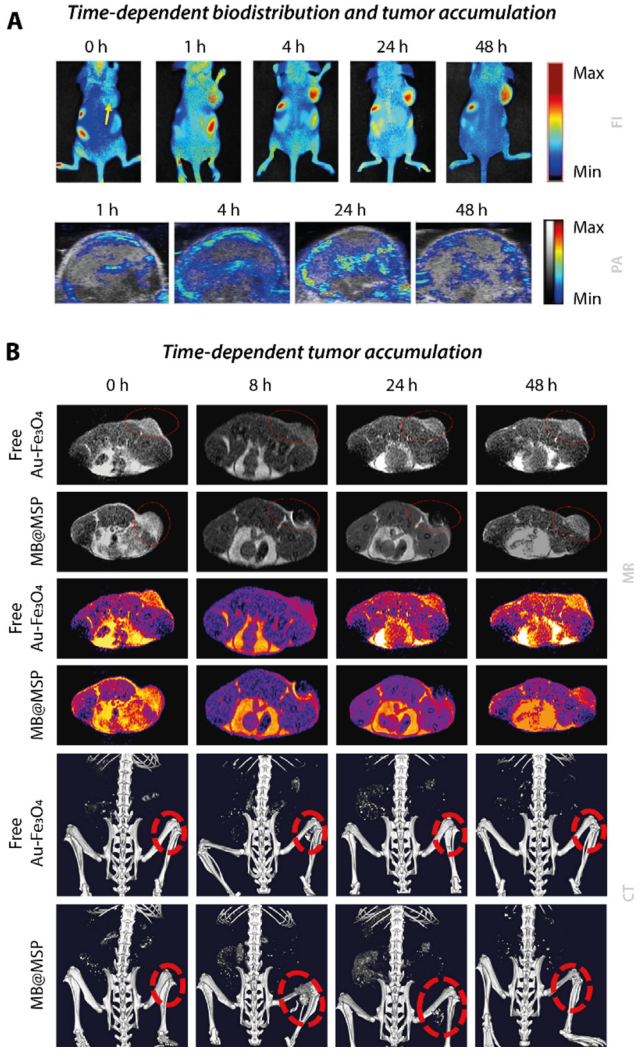

Fig. 9. In vivo imaging of mesoporous silica nanoparticles (MSNs). **A**) Yang et al. designed a multi-layered MSN formulation, which is essential to prevent undesired drug leakage [225]. (Top) Whole animal fluorescence imaging showed a time-dependent increase in signal intensity, with peak intensity at 24 h after administration. (Bottom) Photoacoustic imaging of the tumor region confirmed intratumoral accumulation with peak values at 24 h post-injection, which was consistent with the fluorescent imaging results. **B**) Feng et al. designed rattle-type mesoporous silica nanoparticles with tumor-sensitive properties [230]. (Top) T_2-weighted MR images and the corresponding pseudo color images demonstrated intratumoral accumulation with highest signal at 8 h after administration and contrast-enhancement up to 48 h. (Bottom) The inclusion of µCT images confirmed gradual intratumor signal increase with high spatial resolution and clear boundaries. In comparison to free Au-Fe_3O_4, the MB@MSP formulation demonstrated a higher CT signal at 24 h post-injection. Adapted with permission from [225,230].

differences in tumor volume. Application of intermittent NIR laser irradiation (660 nm, 0.5 W/cm^2, 8 min) at 8 h post-injection on day 1, 3, 5, and 8 was only performed on the primary tumor. A 98.49 % volume decrease was observed in the primary tumor upon treatment with MB@MSP + NIR. However, distal tumors did benefit from this treatment schedule as shown by the inhibited tumor growth in comparison to the rapidly growing control groups. Therefore the nanosystem formulation is able to trigger tumor cell apoptosis and subsequently further influence the anti-tumor response of the immune system.

6.8. Quantum dots

Quantum Dots have been studied extensively for application as an imaging probe, being able to be visualized in vivo with high levels of brightness through advanced techniques such as spectral- [135] and intravital imaging [232]. Due to the broad optical range, QDs are able to fall within the NIR-I (λ = 650 – 950 nm) or NIR-II (λ = 1000 – 1350 nm) spectrum depending on the size and the incorporated materials [233]. A comparison between CdSe@Zns (NIR-I) and Ag_2S (NIR-II) demonstrated more defined real-time visualization of tumor vasculature for the NIR-II quantum dots [234]. Despite the Ag_2S nanosystems not falling within the tissue transparency window, the negligible tissue autofluorescence at these wavelengths allows for imaging at high spatial resolution. Regardless of the corresponding wavelength, heavy-metal QDs are still considered to exhibit superior brightness and photostability. Even showing potential to localize small metastatic foci upon functionalization with tumor-targeted ligands [235].

6.8.1. Conventional quantum dots

Aside from the establishment as a strong imaging probe, QDs also show potential as smart drug delivery systems. Savla et al. designed targeted QDs with pH-responsive drug release for treatment of multidrug resistant ovarian cancer [236]. Initial DNA aptamer conjugation induced MUC-1 specific targeting, followed by DOX attachment through pH-sensitive hydrazone bonds. Whole animal fluorescence imaging showed that in comparison to non-modified QDs, QD-MUC1 showed significant differences in major organ distribution, mainly decreased splenic- and increased intratumoral uptake, already at 1 h post-injection.

In order to maximize circulation time and minimize organ uptake, functionalization through zwitterions can act as non-specific tumor targeting. Sun et al. designed heavy metal quantum dots with a Cu-In-Se (CIS) base [237]. Functionalization occurred through inclusion of ^{111}In and multidentate zwitterionic polymer ligands. The latter contributes to physiological stability by reducing non-specific interaction, and therefore results in prolonged blood circulation. The CIS radioactive QDs (cIS-rQDs) were subsequently used as a tracer for intratumoral accumulation. Despite being untargeted, radioactive- and the fluorescent signals indicated the presence of QDs within the tumor region, which can be attributed to the passive EPR effect (Fig. 10A). After 48 h, signal co-localization of both imaging techniques confirmed the stability and retention of cIS-rQDs within the tumor.

However, in vivo applications of heavy-metal QDs for theranostic purposes are rather limited in comparison to other organic- and inorganic nanosystems. This can be largely contributed to the intrinsic, long-term toxicity, as quantum dots show the tendency to accumulate within the liver and spleen [134]. A distinction can be made between four factors that add to this toxicity; i) heavy metals within the QD core, ii) surface coatings with toxic potential, iii) free radicals or ROS generated from excitation, and iv) tissue and nano-colloid interaction in biological environments [134].

6.8.2. Quantum dot complexes

Surface passivation of quantum dots could potentially reduce the release of toxic ions into the systemic circulation. Olerile et al. co-encapsulated PTX and QDs within a nanostructured lipid carrier (NLC) shell, which also contained an internal lipid matrix to protect the theranostic cargo [238]. NIR fluorescence imaging demonstrated distinct fluorescence contrast within the tumor region, which was visible 1 h post-injection. However, the intratumoral signal intensity decreased over time, which coincided with an increase in hepatic signal. Nevertheless, treatment with NLCs showed a tumor growth inhibition rate of more than 77 % in comparison to the saline control. Characteristic for systemic toxicity is observation of weight changes after treatment. In this study, no significant weight changes were observed over a period of 20 days after drug administration. This indicates minimal toxicity associated with administration of either free PTX or the co-loaded NLC.

Besides shielding, the development of metal-free quantum dots shows promise as an alternative QD type, as these yield similar characteristics, such as brightness and photostability, with reduced toxicity. Hua et al. designed a BCCGH nanosystem, which is synthesized by introducing carbon dots to an environment containing BSA-Cu^{2+}–Gd^{3+} complexes [239]. Subsequent external functionalization with the photosensitizer HPPH resulted in a nanosystem with excellent hemocompatibility and -photodynamic therapeutic performance. The small size of the nanosystem (~7.9 nm) and biocompatibility resulted in high tumor accumulation within 3 h post-injection, as confirmed through NIR, PA, and T_1-weighted MR imaging. Subsequent NIR laser irradiation (808 nm, 0.3 W/cm^2, 10 min) resulted in the intratumoral induction of mild hyperthermic temperatures (43.1 °C), which completely eradicated the subcutaneous tumor after 6 days with no noticeable regrowth up to 14 days. In addition, nanosystem displayed efficient renal clearance over time, which avoided Cu or Gd-induced systemic toxicity. Luo et al. demonstrated that harsh components, such as Gd, are not necessary to grant enhanced multimodal imaging using carbon-based quantum dots [240]. A hybrid nanosystem based on iron-doped carbon dots (Fe@CDs) surrounded by amphiphilic lipopeptide assemblies (DSPE-mPEG2000/RLS) was designed for gene delivery. The PEG-RLS/Fe@CDs complexes were suitable for tetramodal imaging, as nanosystem accumulation could be confirmed through FL, PA, PTT, and T_1-weighted MR imaging (Fig. 10B). As the peak intensity was confirmed at 28 h post-injection, subsequent NIR laser irradiation (660 nm, 0.5 W/cm^2, 5 min) was performed at that time point. This resulted in tumor growth inhibition and a significant increase in survival in comparison to the control groups. Therefore indicating that this nanotheranostic platform is suitable for gene delivery, synergistic therapy, and tetramodal imaging without the implementation of toxic heavy metals for either the nanosystem base or as an imaging modality.

6.9. Hybrids and other ingenious strategies

It is difficult to define a true hybrid, as some of the aforementioned designs incorporated other nanosystems as a minor functionalization. However, in our opinion, there are some noteworthy studies on nanosystems which technically cannot be placed in one of the defined nanosystem categories.

An excellent example of nanohybrid strength are Janus nanoparticles (JNPs). These two-faced delivery platforms are able to integrate conflicting materials into a single delivery platform [241]. Development of an asymmetric heterostructure is important to establish distinct functionalizations. For instance, Chen et al. designed multifunctional JNPs via the masking method; by maintaining one side of the base and modifying the other with different functional materials, the nanosystem becomes asymmetrical and two-faced [242]. The biopolymer poly(acrylic acid) (PAA) was

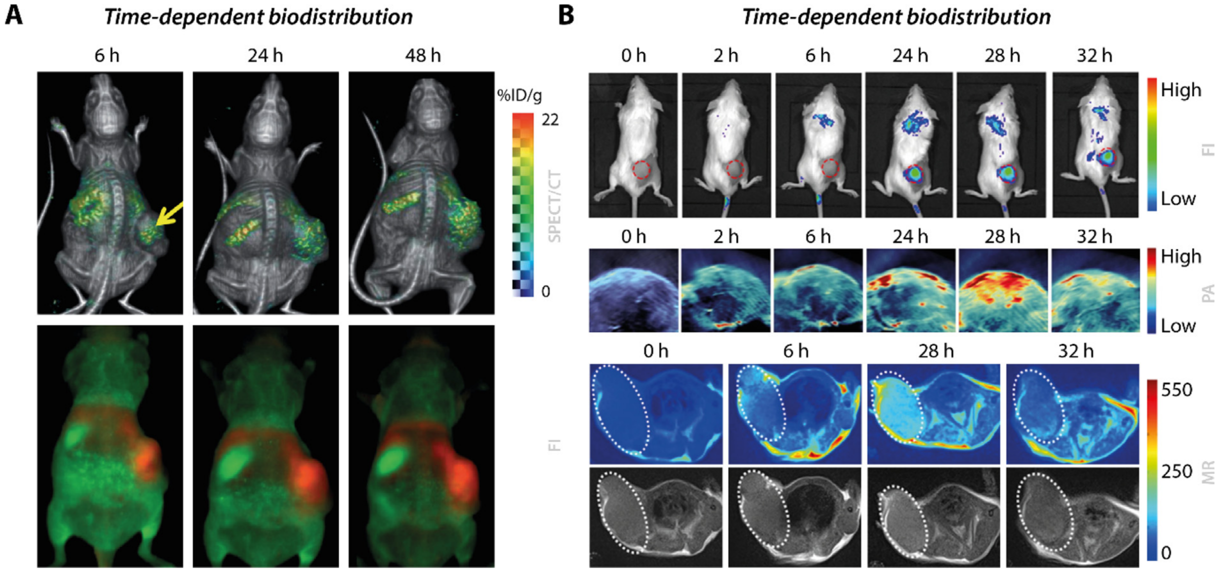

Fig. 10. In vivo imaging of quantum dots (QDs). **A**) Sun et al. designed indium-111 labelled, zwitterionic quantum dots [237]. Despite the lack of tumor-targeting functionalities, the SPECT/CT images and fluorescence images showed strong signal intensities within the tumor region. After 48 h, co-localization of both imaging modalities confirmed the stability and retention within the tumor. **B**) Luo et al. employed iron-doped quantum dots as an alternative to harsh materials for tetramodal imaging [240]. Fluorescence (Top), PA (Middle), and MR imaging (Bottom) all confirmed that peak QD accumulation was at 28 h post-injection. Adapted with permission from [237,240].

selected as the base material, which makes the nanosystem sensitive to the acidic micro-environment. The addition of various elements (N, Na, Y, Yb, and Au) within the PAA base allowed CT and MR imaging. Subsequent addition of multiple chemicals followed by a solvothermal reaction resulted in the formation of the double-layered nanobowls (NB). The formation of gold nanoflowers (AuF) on the NB surface was established via the addition of $HAuCl_4$, which provides a tuneable NIR response. The functionalization of these OA-UCNPs/PDA-AuF JNPs was completed through the loading of hydrophilic doxorubicin and hydrophobic hydroxycamptothecin within their distinct domains. Therefore, upon either pH or NIR exposure, only the release of a single drug type is initiated. Sequential therapy will result in synergistic tumor treatment due to simultaneous drug release and photothermal conversion. CT- and T_2-weighted MR imaging confirmed tumor accumulation, with peak signal intensities visible at 24 h post-injection. Subsequent NIR laser irradiation (1064 nm, 1.0 W/cm^2, 10 min) led to an intratumoral temperature of 51.5 °C, eventually resulting in effective tumor growth inhibition and prolonged survival.

In another study, Zhang et al. established a cage-sphere Janus nanoparticle via a different approach [243]. This design begins with an Ag nanocube (AgNC) base, which is subsequently partially enveloped by PAA. Selective growth of $Fe(OH)_3$ on the PAA surface provides the pH stimuli-responsive capability, MR imaging-, and hydrophilic drug loading properties. Initiation of a galvanic replacement reaction via the addition of $HAuCl_4$ causes the transformation from AgNC to AuNC. This does not only provide the NIR stimuli-responsive properties, but also grants hydrophobic drug storage, exploitation as a CT CA, and PTT capability. These AuNC/$Fe(OH)_3$-PAA JNPs nanosystems were loaded with hydrophilic doxorubicin and hydrophobic docetaxel, which were independently released based on either pH or NIR exposure. Animal imaging at 24 h post-injection demonstrated a time-dependent positive contrast enhancement at the tumor site for both CT and MR. The synergistic efficacy of DOX/Dtxl delivery was evident, as only delivery of the JNP nanosystem already improved tumor inhibition, while JNP administration with NIR laser exposure even further decreased the tumor volume and -weight.

Instead of biodegradability based on the acidic tumor micro-environment, other factors which are known for their overexpression within TME could also be employed. For instance, Cai et al. developed a nanoparticle dependent on fragmentation of the polymer backbone through cathepsin B [30]. Cathepsin B overexpression is predictive for poor prognosis in a number of tumor types, and a positive correlation has been established between cathepsin B expression and metastatic potential [244]. Functionalization of poly[N-(2-hydroxypropyl) methacrylamide (pHPMA) with Cy5.5, PTX, and Gd results in a branched polymer backbone. Integration of the Gly-Phe-Leu-Gly (GFLG) tetrapeptide induces stimuli-sensitive crosslinking between branched pHPMAs, resulting in the formation of BP-PTX-Gd NPs through self-assembly. Upon entering the tumor cellular micro-environment, cathepsin B induces fragmentation of the nanosystem through cleavage of both the GFLG and the pHPMA backbone. Temporal-spatial distribution of the nanosystem was assessed through MRI imaging, which demonstrated peak intensity at 24 h after administration. Confocal microscopy showed a gradual increase in fluorescence intensity in the non-vascular tumor region after 6 h, indicating that BP-PTX-Gd NPs were able to extravasate from the tumor blood vessels. Subsequent therapeutic efficacy was evaluated through longitudinal image-guided drug response. Only the T_1-weighted images of the treated group showed both a decrease in tumor volume and an increase in tumor T_1 values, indicative of effective tumor therapy.

Other possible applications of hybrids are encapsulation of drug-loaded nanosystems within other nanomaterials. For instance, Zhou et al. designed a nanosystem with gelatin-based DOX-loaded SWNT [245]. This entity was subsequently copolymerized with pNIPAM in order to create a thermo-sensitive hydrogel. Intratumoral administration of the DOX/SWNT-GEL and subsequent NIR laser irradiation (976 nm, 0.2 W/cm^2, 10 min) showed significant reduction in tumor size over a 27 day study period. This was confirmed through ^{18}F-FDG tracked PET/CT imaging, which allows for assessment of tumor biological metabolism activity through radiotracer uptake. Animals treated with DOX/SWNT-GEL showed the least tumor growth and the lowest metabolic activity, confirming inhibitory efficiency.

7. Clinical application

Despite the preclinical nature of this review, it is important to mention the potential of image-guided drug delivery of nanomedicine for clinical application. When looking at IGDD and publications on this topic, as also argued in the next section, a considerable number of publications do not deal with true IGDD when we adhere to our definition. A majority of the data deals with the possibility to monitor what is happening, for instance nanoparticle accumulation, delivery, and tumor response. Acting based on imaging and thus inflicting or improving drug delivery is less shown.

The clinical trials currently listed at the clinical trials website (https://www.clinicaltrials.gov) with "imaged guided drug delivery" as search term and limited to "cancer" show mostly studies related to surgery (removal of tumors and biopsies), ablation, and radiotherapy (last search conducted October 18, 2022). Only two out of the 291 trials in total retrieved remained when also the keywords "nanoparticle" or "nanosystem" where added. While these studies within the 291 retrieved are not focused on image guided drug delivery, some of these do shed some light on what is possible. Especially the use of MR and the powerful possibilities for visualization of the tumor and tracking of the compound of interest is underscored. The clinical trial on topotecan delivery in high-grade glioma shows how MR can be used to see the tumor while gadolinium is added to the chemotherapeutic to follow the drug (NCT02278510). Likewise, MR is used to locate a tumor, and to monitor efficiency of ablation through MR-guided HIFU by thermal mapping (NCT02616016 and NCT01309048). Alternatively, NIR guided fluorescence imaging has been employed for sentinel lymph node mapping in breast cancer. ICG is injected and followed to identify the lymph node (NCT01468649). A currently recruiting trial on image-guided targeted doxorubicin delivery using hyperthermia and TSLs in combination with MR-HIFU is precisely using the possibilities provided by the examples above (NCT03749850). MR-based identification of the tumor in combination with MR-based temperature mapping helps to heat the region of interest, i.e. the tumor, precisely. More so, this setup allows, if implemented, real time steering of the temperature location and level and as such steer efficient drug release from TSLs.

The last mentioned trial is one of the clearest example where IGDD is possible and may provide a powerful tool to optimize local delivery of an active compound and as such improve clinical outcome. Chaudhry et al. show in a recent overview the status of preclinical and clinical studies on thermosensitive liposomes and heating modalities [246]. Clearly, MR-HIFU or radiofrequency-based heating is preferred, which both allow MR thermometry. As MR imaging has multiple advantages, as mentioned above, this imaging modality may not only be used in combination with TSLs but likely also with other nanosystems.

We conclude that clinical application of true image-guided drug delivery is currently limited. While in animals a plethora of possibilities are available, translation to patients is met with serious hurdles. The size of humans and the limited penetration of important imaging methods do not go well together. Fluorescence and photoacoustic imaging may have use for superficial tumors or when IGDD is combined with surgery to expose the area of interest. This is a pity as optical imaging provides high resolution not seen with MR and nuclear imaging techniques. Although MR and nuclear imaging make the use of costly and bulky machines necessary, the advantages are obvious. The good penetration of tissues and acceptable resolution (mm) as well as the possibility of combination with other modalities provide basis for further exploration.

An important aspect of nanomedicine and IGDD is the cumulated complexity of the application. When studies in animals show promising results, translation is not seldom met by the almost impossible setup needed. Heating a mouse, while receiving NIR irradiation and at the same time being monitored is feasible in that animal. However, in patients, treatment combinations need to be developed that are compatible with the patient and with the available systems. We argue that the nanosystem devised needs to be compatible, not-toxic, degradable or at least readily excreted and cost-efficient. The imaging modalities can be a range of techniques discussed here and may all apply depending on the setting, such as tumor location, combination with surgery or radio-intervention, and the used nanomedicine.

8. Conclusions and future perspectives

Precision medicine may well be the Holy Grail in cancer therapy. While new and promising compounds, with specific function or acting on specific tumor features, become available in an increasing rate, personalization of treatment becomes more and more important. However, precision medicine also equals precision diagnosis and precision delivery of therapeutics. The recent rise in application of, for instance, checkpoint inhibitors and other compounds acting on tumor cell- and tumor micro-environment specific characteristics, shows clearly benefit [247]. But, it also becomes more and more clear that in quite a few cases patients are over-treated with actually little to no beneficial effect. This is certainly undesirable considering the notion that, like the wide spectrum chemotherapeutics, also these specific compounds are able to induce serious side effects [248]. More so, these observations indicate that irrespective of the compound administered for the treatment of cancer, two sides of the equation need to be considered: effective tumor cell killing, and exclusion of healthy tissues. It is important to realize that both are, first of all, affected by the precision and extent of delivery. Importantly, this is actually gravely ignored.

Nanomedicine and nano(bio)technology have vastly developed and gained an important position in cancer therapy. However, the most progress has been made in the experimental and preclinical setting. To understand the success and failure of nanosystem-based cancer therapy, the development of a lipid-based nanoparticle for the delivery of doxorubicin, a broad band chemotherapeutic with distinct and severe toxicity, serves as a useful example. Doxil$^{®}$, the formulation of doxorubicin in a PEGylated liposome, was devised to improve pharmacokinetics, augment drug delivery, and diminish toxicity, especially to the heart [91]. Encapsulation of doxorubicin in a liposome prevents drug interaction with cardiomyocytes, thus preventing late toxicity and the necessity of a heart transplant. Also, and certainly due to PEGylation of these liposomes, pharmacokinetics is dramatically changed. The blood residence time has become a matter of days instead of minutes for free doxorubicin, and a volume of distribution of around 5 L with Doxil$^{®}$ compared to around 500 L for free doxorubicin after administration of the same dose [11]. Indeed, these alterations resulted in the registration of Doxil$^{®}$. However, close examination of the registration and clinical data revealed that Doxil$^{®}$ is mainly beneficial due to the altered toxicity profile, and not per se as a result of an improved clinical response. This although administration of Doxil$^{®}$ does improve accumulation of doxorubicin in tumors.

Doxil$^{®}$, like the majority of the nanosystems developed for treatment of solid tumors, is made with the so-called EPR effect in mind. EPR is the Enhanced Permeability and Retention of particles in a tumor due to altered pathophysiology, such as leaky vasculature and poor lymphatic drainage [1]. These characteristics are absent in healthy tissues. The premises are simple: when a particle circulates long enough and the EPR effect is in place, particles (when small enough, i.e. approximately 100 nm) will accumulate to a higher extent in the tumor. Indeed a correlation exists between circulation time and tumor accumulation. As this effect is passive, or also denoted as the natural fate of long circulating nanoparticles, treatment is relatively simple and does not demand costly and troublesome interventions. Despite all these favored characteristics, the question is why is treatment with Doxil® not more effective than administered free doxorubicin, and what can be done?

Formulation of nanosystems for the delivery of compounds brings forward a list of demands, which are grossly in conflict. To ensure a long circulation time, protect the compound against degradation, prevent compound interaction with healthy tissues, and to obtain accumulation at the target site – this can be achieved at different levels as discussed below –a nanosystem needs to be stable. Stable on the shelf and stable in circulation. We and others observed that Doxil® is indeed very stable, and that after infusion of Doxil® the carrier (i.e. liposome) and doxorubicin stay together for days within the circulation [183,249]. However, clearly at one moment content and carrier need to dissociate to enable the encapsulated drug to interact. This is coined bioavailability. We showed previously that upon accumulation of Doxil®, drug and carrier remained associated in both tumor and tumor cells [38,250]. These results indicate that a trigger should be employed, which would initiate a release of content at the right moment. Several studies are present that employ triggers, either intrinsic to the tumor micro-environment (i.e. endogenous triggers) or applied externally [247,251]. Upon accumulation a reduction in pH or presence of enzymes, which are specifically upregulated in tumors, can be used to alter the nature of a nanoparticle to such extent that payload release is induced. The benefit of this approach is that it does not require a complex, uncomfortable (for the patient), and costly setting. Also, as the tumor determines the content release, a certain degree of specificity is achieved. However, endogenous triggers are seldom tumor specific, have slow kinetics, meaning that payload release could take hours to days, and may be heterogeneously present within a tumor. Taken together, nanomedicine would benefit from the possibility to monitor, control, and manipulate nanoparticle accumulation and content release at a reasonable spatial and temporal level.

To continue on the first registered liposomal chemotherapeutic and what can be done to improve therapeutic activity. As described above, Doxil® does not have to be written off completely, but could be used as a starting point for further improvement to tackle the bioavailability issues. Next to that, accumulation in tumors is not as good as what may be expected from EPR determination. Gaps up to 1200 μm were detected between endothelial cells in the tumor vascular lining, enabling unhindered extravasation of nanoparticles [252]. However, this is not happening as smoothly, and extravasation of 90 nm particles is dramatically impaired reaching on average a meager 0.7 % of the injected dose [253]. Tumor pathophysiology and tumor characteristics, such as an elevated interstitial fluid pressure (IFP) and desmoplasia, are responsible for this limitation. We and others showed that extravasation of nanoparticles is augmented by locally heating tumors to mild hyperthermic temperatures (40–43 °C) [254–256]. In addition, local hyperthermia is used to manipulate drug bioavailability by inducing triggered release from so-called thermosensitive liposomes. In both settings, application of a local trigger determines targeting of delivery. Clearly, the use of an external energy source determines how precise and to what extent drug is delivered after systemic bulk administration. It is easy to envision that local delivery through the above described methods, as would be for other locally tunable systems, enables precision medicine. But, and that is instrumental and can be learned from our review, this can only be achieved if a higher level of control is achieved. This control, we argue, comes from online and precise monitoring, which is coupled to decision making on application of the external trigger or manipulation (both of the tumor pathophysiology as well as the nanoparticle). You would like to be able to image the nanoparticle, monitor the presence in tumor, tumor interstitial space, or tumor cells, and monitor kinetics of the active component. In other words, precision medicine would profit from image-guided delivery.

For image-guided drug delivery, several settings are required. We describe here the plethora of imaging possibilities, at resolution up to mm and at all sites of the body, which can be used to monitor nanosystems. Also, there are numerous labelling techniques to visualize nanosystems, induce tumor-specific targeting, or to monitor the response to internal- or external triggers. Additionally, a number of energy sources are used to improve intratumoral accumulation of drugs and nanocarriers or to induce release of active compound. Together, these allow for image-guided drug delivery. An example are thermosensitive liposomes combined with high-intensity focused ultrasound (HIFU)-triggered release guided by MR imaging [199,200]. However, clinical trials on this combination set-up failed to reach the endpoint and showed no benefit. Closer examination of these trials indicated that actually the absence of IGDD contributed largely to this failure.

Do we see light at the end of the tunnel? Indeed we do. Here we review a number of studies showing the use or potential of IGDD. It is of course important to consider several aspects. One: a majority of publication mentioning IGDD do not actually show this, but rather use imaging to follow the process. In other words, imaging is not used to directly affect nanoparticle behavior or drug activity. We started our review by providing a definition of IGDD. And, we think that when applied properly and truly, IGDD has profound benefits. Two: IGDD needs to be separated from IGDR, image-guided drug release. Although we want to prevent that we as researchers get lost in semantics, clear definitions of IGDD and IGDR may not only help to understand how treatment options work, but may also guide further development. Where IGDD is the use of imaging to improve delivery at the tumor, IGDR is the use of imaging to determine separation of the drug from a carrier when in the tumor cell. In the latter, drug delivery already occurred, but remains trapped within the tumor cell. Also, this option still relies on EPR with the above mention limitations. Three: Simple is beautiful. Clearly, combination of a trigger-responsive nanosystem, together with online monitoring, adjustment of treatment based upon that, and the application of a facilitator with high accuracy and homogeneity, is a complex and costly approach. Exotic and complex hybrid nanosystems with multiple functions and responsiveness to several external triggers have been described. The efficacy of these systems sometimes do result from the fact that several processes act together, possibly in synergy. However, with the lack of solid proof that these set-ups may actually work in patients, and the failure of preceding trials, the reluctance to invest is understandable.

Image-guided drug delivery and image-guided drug release of nanosystems are, in our opinion, the way forward to render the field of nanomedicine effective in the oncologic setting. We propose a relatively simple approach, which allows for imaging, monitoring, and manipulation in a feasible setting. Taken together, the necessary tools are available, patients groups with amendable oncology, such as locally advanced cancers, recurrent cancers and cancers in need of local control or tumor volume reduction, are present, and therefore the need is there. Image-guided nanomedicine-based cancer therapy definitely has future, and when conducted in optimally controlled and executed trials will certainly proof our conviction.

Data availability

No data was used for the research described in the article.

Declaration of Competing Interest

The authors declare that they have no known competing financial interests or personal relationships that could have appeared to influence the work reported in this paper.

References

[1] T.L.M. Ten Hagen, M.R. Dreher, S. Zalba, A.L.B. Seynhaeve, M. Amin, L. Li, D. Haemmerich, Drug transport kinetics of intravascular triggered drug delivery systems, Commun Biol. 4 (1) (2021) 920.
[2] S. Hossen, M.K. Hossain, M.K. Basher, M.N.H. Mia, M.T. Rahman, M.J. Uddin, Smart nanocarrier-based drug delivery systems for cancer therapy and toxicity studies: A review, J Adv Res. 15 (2019) 1–18.
[3] A.A. Exner, M.C. Kolios, Bursting Microbubbles: How Nanobubble Contrast Agents Can Enable the Future of Medical Ultrasound Molecular Imaging and Image-Guided Therapy. Curr Opin Colloid, Interface Sci. (2021) 54.
[4] Y. Ma, Q. Mou, D. Yan, X. Zhu, Engineering small molecule nanodrugs to overcome barriers for cancer therapy, View. 1 (3) (2020).
[5] Y. Gou, D. Miao, M. Zhou, L. Wang, H. Zhou, G. Su, Bio-Inspired Protein-Based Nanoformulations for Cancer Theranostics, Front Pharmacol. 9 (2018) 421.
[6] J. Wang, P. Mi, G. Lin, Y.X. Wang, G. Liu, X. Chen, Imaging-guided delivery of RNAi for anticancer treatment, Adv Drug Deliv Rev. 104 (2016) 44–60.
[7] L. Wu, W. Zhou, L. Lin, A. Chen, J. Feng, X. Qu, H. Zhang, J. Yue, Delivery of therapeutic oligonucleotides in nanoscale, Bioact Mater. 7 (2022) 292–323.
[8] S. Fobian, Z. Cheng, T.L.M. Ten Hagen, Smart Lipid-Based Nanosystems for Therapeutic Immune Induction against Cancers: Perspectives and Outlooks, Pharmaceutics. 14 (26) (2022).
[9] H. He, L. Liu, S. Zhang, M. Zheng, A. Ma, Z. Chen, H. Pan, H. Zhou, R. Liang, L. Cai, Smart gold nanocages for mild heat-triggered drug release and breaking chemoresistance, J Control Release. 323 (2020) 387–397.
[10] S. Li, Q. Jiang, Y. Liu, W. Wang, W. Yu, F. Wang, X. Liu, Precision Spherical Nucleic Acids Enable Sensitive FEN1 Imaging and Controllable Drug Delivery for Cancer-Specific Therapy, Anal Chem. 93 (32) (2021) 11275–11283.
[11] A.L.B. Seynhaeve, M. Amin, D. Haemmerich, G.C. van Rhoon, T.L.M. Ten Hagen, Hyperthermia and smart drug delivery systems for solid tumor therapy, Advanced Drug Delivery Reviews. 163 (2020) 125–144.
[12] M.S. Franco, E.R. Gomes, M.C. Roque, M.C. Oliveira, Triggered Drug Release From Liposomes: Exploiting the Outer and Inner Tumor Environment, Front Oncol. 11 (2021).
[13] J. Wallyn, N. Anton, S. Akram, T.F. Vandamme, Biomedical Imaging: Principles, Technologies, Clinical Aspects, Contrast Agents, Limitations and Future Trends in Nanomedicines, Pharm Res. 36 (6) (2019) 78.
[14] P. Sarbadhikary, B.P. George, H. Abrahamse, Recent Advances in Photosensitizers as Multifunctional Theranostic Agents for Imaging-Guided Photodynamic Therapy of Cancer, Theranostics. 11 (18) (2021) 9054–9088.
[15] H.S. Jung, P. Verwilst, A. Sharma, J. Shin, J.L. Sessler, J.S. Kim, Organic molecule-based photothermal agents: an expanding photothermal therapy universe, Chem Soc Rev. 47 (7) (2018) 2280–2297.
[16] J. Wahsner, E.M. Gale, A. Rodriguez-Rodriguez, P. Caravan, Chemistry of MRI Contrast Agents: Current Challenges and New Frontiers, Chem Rev. 119 (2) (2019) 957–1057.
[17] A.M. Ponce, B.L. Viglianti, D. Yu, P.S. Yarmolenko, C.R. Michelich, J. Woo, M.B. Bally, M.W. Dewhirst, Magnetic resonance imaging of temperature-sensitive liposome release: drug dose painting and antitumor effects, J Natl Cancer Inst. 99 (1) (2007) 53–63.
[18] D.K. Kirui, M. Ferrari, Intravital Microscopy Imaging Approaches for Image-Guided Drug Delivery Systems, Current Drug Targets. 16 (6) (2015) 528–541.
[19] B.P. Joshi, T.D. Wang, Targeted Optical Imaging Agents in Cancer: Focus on Clinical Applications, Contrast Media Mol Imaging. 2018 (2018) 2015237.
[20] S. Luo, E. Zhang, Y. Su, T. Cheng, C. Shi, A review of NIR dyes in cancer targeting and imaging, Biomaterials. 32 (29) (2011) 7127–7138.
[21] M. Potara, T. Nagy-Simon, M. Focsan, E. Licarete, O. Soritau, A. Vulpoi, S. Astilean, Folate-targeted Pluronic-chitosan nanocapsules loaded with IR780 for near-infrared fluorescence imaging and photothermal-photodynamic therapy of ovarian cancer, Colloids Surf B Biointerfaces. 203 (2021).
[22] L. Wang, C. Niu, IR780-based nanomaterials for cancer imaging and therapy, J Mater Chem B. 9 (20) (2021) 4079–4097.
[23] J. Jiao, J. Zhang, F. Yang, W. Song, D. Han, W. Wen, W. Qin, Quicker, deeper and stronger imaging: A review of tumor-targeted, near-infrared fluorescent dyes for fluorescence guided surgery in the preclinical and clinical stages, Eur J Pharm Biopharm. 152 (2020) 123–143.
[24] W.N. Zeng, Q.P. Yu, D. Wang, J.L. Liu, Q.J. Yang, Z.K. Zhou, Y.P. Zeng, Mitochondria-targeting graphene oxide nanocomposites for fluorescence imaging-guided synergistic phototherapy of drug-resistant osteosarcoma, J Nanobiotechnology. 19 (1) (2021) 79.
[25] A.L.B. Seynhaeve, T.L.M. Ten Hagen, An adapted dorsal skinfold model used for 4D intravital followed by whole-mount imaging to reveal endothelial cell-pericyte association, Sci Rep. 11 (1) (2021) 20389.
[26] T. Satake, A. Suetsugu, M. Nakamura, T. Kunisada, M. Shimizu, S. Saji, H. Moriwaki, R.M. Hoffman, Color-coded Imaging of the Circulating Tumor Cell Microenvironment, Anticancer Res. 38 (10) (2018) 5635–5638.
[27] Mezzanotte L, van 't Root M, Karatas H, Goun EA, Lowik C. In Vivo Molecular Bioluminescence Imaging: New Tools and Applications. Trends Biotechnol. 2017;35(7):640-52.
[28] A.L.B. Seynhaeve, T.L.M. Ten Hagen, Intravital Microscopy of Tumor-associated Vasculature Using Advanced Dorsal Skinfold Window Chambers on Transgenic Fluorescent Mice, J Vis Exp. 131 (2018).
[29] J.L. Arias, Advanced methodologies to formulate nanotheragnostic agents for combined drug delivery and imaging, Expert opinion on drug delivery. 8 (12) (2011) 1589–1608.
[30] H. Cai, X. Dai, X. Wang, P. Tan, L. Gu, Q. Luo, X. Zheng, Z. Li, H. Zhu, H. Zhang, et al., A Nanostrategy for Efficient Imaging-Guided Antitumor Therapy through a Stimuli-Responsive Branched Polymeric Prodrug, Adv Sci (Weinh). 7 (6) (2020) 1903243.
[31] H.L. Stewart, D.J.S. Birch, Fluorescence Guided Surgery. Methods Appl Fluoresc. 9 (2021) 4.
[32] W. Blondel, M. Amouroux, S.M. Zaytsev, E.A. Genina, V. Colas, C. Daul, A.B. Pravdin, V.V. Tuchin, Human skin autofluorescence and optical clearing, in: D. Zhu, V.V. Tuchin, E.A. Genina (Eds.), Handbook of Tissue Optical Clearing: New Prospects in Optical, CRC Press, Imaging, 2022, pp. 109–125.
[33] A.B. Shrirao, R.S. Schloss, Z. Fritz, M.V. Shrirao, R. Rosen, M.L. Yarmush, Autofluorescence of blood and its application in biomedical and clinical research, Biotechnol Bioeng. 118 (12) (2021) 4550–4576.
[34] S. Bhaumik, J. DePuy, J. Klimash, Strategies to minimize background autofluorescence in live mice during noninvasive fluorescence optical imaging, Lab Anim. 36 (8) (2007) 40–43.
[35] A.M. Smith, M.C. Mancini, S. Nie, Bioimaging: second window for in vivo imaging, Nat Nanotechnol. 4 (11) (2009) 710–711.
[36] C. Li, M. Qian, S. Wang, H. Jiang, Y. Du, J. Wang, W. Lu, N. Murthy, R. Huang, Aptavalve-gated Mesoporous Carbon Nanospheres image Cellular Mucin and provide On-demand Targeted Drug Delivery, Theranostics. 7 (13) (2017) 3319–3325.
[37] L. Li, T.L. ten Hagen, M. Hossann, R. Suss, G.C. van Rhoon, A.M. Eggermont, D. Haemmerich, G.A. Koning, Mild hyperthermia triggered doxorubicin release from optimized stealth thermosensitive liposomes improves intratumoral drug delivery and efficacy, J Control Release. 168 (2) (2013) 142–150.
[38] A.A. Manzoor, L.H. Lindner, C.D. Landon, J.Y. Park, A.J. Simnick, M.R. Dreher, S. Das, G. Hanna, W. Park, A. Chilkoti, et al., Overcoming limitations in nanoparticle drug delivery: triggered, intravascular release to improve drug penetration into tumors, Cancer Res. 72 (21) (2012) 5566–5575.
[39] M.N. Centelles, M. Wright, P.W. So, M. Amrahli, X.Y. Xu, J. Stebbing, A.D. Miller, W. Gedroyc, M. Thanou, Image-guided thermosensitive liposomes for focused ultrasound drug delivery: Using NIRF-labelled lipids and topotecan to visualise the effects of hyperthermia in tumours, J Control Release. 280 (2018) 87–98.
[40] S. Park, U. Jung, S. Lee, D. Lee, C. Kim, Contrast-enhanced dual mode imaging: photoacoustic imaging plus more, Biomed Eng Lett. 7 (2) (2017) 121–133.
[41] A.B.E. Attia, G. Balasundaram, M. Moothanchery, U.S. Dinish, R. Bi, V. Ntziachristos, M. Olivo, A review of clinical photoacoustic imaging: Current and future trends, Photoacoustics. 16 (2019).
[42] W. Wang, T. Jing, X. Xia, L. Tang, Z. Huang, F. Liu, Z. Wang, H. Ran, M. Li, J. Xia, Melanin-loaded biocompatible photosensitive nanoparticles for controlled drug release in combined photothermal-chemotherapy guided by photoacoustic/ultrasound dual-modality imaging, Biomater Sci. 7 (10) (2019) 4060–4074.
[43] L. Zhang, D. Jin, M.H. Stenzel, Polymer-Functionalized Upconversion Nanoparticles for Light/Imaging-Guided Drug Delivery, Biomacromolecules. 22 (8) (2021) 3168–3201.
[44] M.S. Karthikesh, X. Yang, Photoacoustic image-guided interventions, Exp Biol Med (Maywood). 245 (4) (2019) 330–341.
[45] H. Hu, Recent Advances of Bioresponsive Nano-Sized Contrast Agents for Ultra-High-Field Magnetic Resonance Imaging, Front Chem. 8 (2020) 203.
[46] T. Anani, S. Rahmati, N. Sultana, A.E. David, MRI-traceable theranostic nanoparticles for targeted cancer treatment, Theranostics. 11 (2) (2021) 579–601.
[47] G. Ma, X. Liu, G. Deng, H. Yuan, Q. Wang, J. Lu, A novel theranostic agent based on porous bismuth nanosphere for CT imaging-guided combined chemo-photothermal therapy and radiotherapy, J Mater Chem B. 6 (42) (2018) 6788–6795.
[48] V. Saluja, Y. Mishra, V. Mishra, N. Giri, P. Nayak, Dendrimers based cancer nanotheranostics: An overview, Int J Pharm. 600 (2021).
[49] D.Y. Zhang, Y. Zheng, H. Zhang, G.G. Yang, C.P. Tan, L. He, L.N. Ji, Z.W. Mao, Folate receptor-targeted theranostic IrSx nanoparticles for multimodal imaging-guided combined chemo-photothermal therapy, Nanoscale. 10 (47) (2018) 22252–22262.
[50] X. Meng, Y. Wu, W. Bu, Functional CT Contrast Nanoagents for the Tumor Microenvironment, Adv Healthc Mater. 10 (5) (2021) e2000912.

[51] N. Aslan, B. Ceylan, M.M. Koç, F. Findik, Metallic nanoparticles as X-Ray computed tomography (CT) contrast agents: A review, Journal of Molecular Structure. 1219 (2020).

[52] Man F, Gawne PJ, R TMdR. Nuclear imaging of liposomal drug delivery systems: A critical review of radiolabelling methods and applications in nanomedicine. Adv Drug Deliv Rev. 2019;143:134-60.

[53] A. Polyak, T.L. Ross, Nanoparticles for SPECT and PET Imaging: Towards Personalized Medicine and Theranostics, Curr Med Chem. 25 (34) (2018) 4328–4353.

[54] J. Jeon, Review of Therapeutic Applications of Radiolabeled Functional Nanomaterials, Int J Mol Sci. 20 (9) (2019).

[55] Z. Iqbal, E.-S.-A. Arafa, Z. Kanwal, G. Murtaza, Smart solution of severe problems: Radiolabeled nanocarriers for cancer imaging and therapy, Journal of Drug Delivery Science and Technology. 61 (2021).

[56] R. Chakravarty, H. Hong, W. Cai, Positron emission tomography image-guided drug delivery: current status and future perspectives, Mol Pharm. 11 (11) (2014) 3777–3797.

[57] M. Xu, W. Yim, J. Zhou, J. Zhou, Z. Jin, C. Moore, R. Borum, A. Jorns, J.V. Jokerst, The Application of Organic Nanomaterials for Bioimaging, Drug Delivery, and Therapy: Spanning Various Domains, IEEE Nanotechnology Magazine. 15 (4) (2021) 8–28.

[58] V. Mishra, M. Singh, P. Nayak, Smart Functionalised-Dendrimeric Medicine in Cancer Therapy. Dendrimers in Nanomedicine: Concept, Theory and Regulatory Perspectives: CRC Press (2021) 233–253.

[59] S. Ray, Z. Li, C.H. Hsu, L.P. Hwang, Y.C. Lin, P.T. Chou, Y.Y. Lin, Dendrimer- and copolymer-based nanoparticles for magnetic resonance cancer theranostics, Theranostics. 8 (22) (2018) 6322–6349.

[60] F. Najafi, M. Salami-Kalajahi, H. Roghani-Mamaqani, A review on synthesis and applications of dendrimers, Journal of the Iranian Chemical Society. 18 (3) (2020) 503–517.

[61] F. Vögtle, E. Buhleier, W. Wehner, Cascade and nonskid-chain-like synthesis of molecular cavity topologies, Synthesis. 2 (1978) 155–158.

[62] N. Filipczak, S.S.K. Yalamarty, X. Li, F. Parveen, V. Torchilin, Developments in Treatment Methodologies Using Dendrimers for Infectious Diseases, Molecules. 26 (11) (2021).

[63] J. Pan, S.A. Attia, N. Filipczak, V.P. Torchilin, Dendrimers for drug delivery purposes. Nanoengineered Biomaterials for Advanced, Drug Delivery (2020) 201–242.

[64] C.C. Lee, J.A. MacKay, J.M. Frechet, F.C. Szoka, Designing dendrimers for biological applications, Nat Biotechnol. 23 (12) (2005) 1517–1526.

[65] L. Palmerston Mendes, J. Pan, V.P. Torchilin, Dendrimers as Nanocarriers for Nucleic Acid and Drug Delivery in Cancer Therapy, Molecules. 22 (9) (2017).

[66] X. Zhou, M. Ye, Y. Han, J. Tang, Y. Qian, H. Hu, Y. Shen, Enhancing MRI of liver metastases with a zwitterionized biodegradable dendritic contrast agent, Biomater Sci. 5 (8) (2017) 1588–1595.

[67] X. Li, A. Naeem, S. Xiao, L. Hu, J. Zhang, Q. Zheng, Safety Challenges and Application Strategies for the Use of Dendrimers in Medicine, Pharmaceutics. 14 (6) (2022).

[68] H. Li, J. Sun, H. Zhu, H. Wu, H. Zhang, Z. Gu, K. Luo, Recent advances in development of dendritic polymer-based nanomedicines for cancer diagnosis, Wiley Interdiscip Rev Nanomed Nanobiotechnol. 13 (2) (2021) e1670.

[69] E. Wiener, M. Brechbiel, H. Brothers, R. Magin, O. Gansow, D. Tomalia, P. Lauterbur, Dendrimer-based metal chelates: a new class of magnetic resonance imaging contrast agents, Magn Reson Med. 31 (1) (1994) 1–8.

[70] R. Iacobazzia, N. Denorab, in: Dendrimer as Imaging Contrast Agents, Academic Press, Dendrimer-Based Nanotherapeutics, 2021, pp. 337–361.

[71] S. Zhang, V. Lloveras, D. Pulido, F. Liko, L.F. Pinto, F. Albericio, M. Royo, J. Vidal-Gancedo, Radical Dendrimers Based on Biocompatible Oligoethylene Glycol Dendrimers as Contrast Agents for MRI, Pharmaceutics. 12 (8) (2020).

[72] M. Filippi, D. Patrucco, J. Martinelli, M. Botta, P. Castro-Hartmann, L. Tei, E. Terreno, Novel stable dendrimersome formulation for safe bioimaging applications, Nanoscale. 7 (30) (2015) 12943–12954.

[73] V. Percec, D.A. Wilson, P. Leowanawat, C.J. Wilson, A.D. Hughes, M.S. Kaucher, D.A. Hammer, D.H. Levine, A.J. Kim, F.S. Bates, et al., Self-assembly of Janus dendrimers into uniform dendrimersomes and other complex architectures, Science. 328 (5981) (2010) 1009–1014.

[74] D.A. Tomalia, Dendrons/dendrimers: quantized, nano-element like building blocks for soft-soft and soft-hard nano-compound synthesis, Soft Matter. 6 (3) (2010) 456–474.

[75] M. Studzian, P. Dzialak, L. Pulaski, D.M. Hedstrand, D.A. Tomalia, B. Klajnert-Maculewicz, Synthesis, Internalization and Visualization of N-(4-Carbomethoxy) Pyrrolidone Terminated PAMAM [G5:G3-TREN] Tecto (dendrimers) in Mammalian Cells, Molecules. 25 (19) (2020).

[76] P. Trzepiński, B. Klajnert-Maculewicz, Dendrimers for fluorescence-based bioimaging, Journal of Chemical Technology & Biotechnology. 92 (6) (2017) 1157–1166.

[77] M. Konopka, A. Janaszewska, K.A.M. Johnson, D. Hedstrand, D.A. Tomalia, B. Klajnert-Maculewicz, Determination of non-traditional intrinsic fluorescence (NTIF) emission sites in 1-(4-carbomethoxypyrrolidone)-PAMAM dendrimers using CNDP-based quenching studies, Journal of Nanoparticle Research. 20 (8) (2018).

[78] Q. Zhou, L. Zhang, T. Yang, H. Wu, Stimuli-responsive polymeric micelles for drug delivery and cancer therapy, Int J Nanomedicine. 13 (2018) 2921–2942.

[79] S.M. Simoes, A.R. Figueiras, F. Veiga, A. Concheiro, C. Alvarez-Lorenzo, Polymeric micelles for oral drug administration enabling locoregional and systemic treatments, Expert Opin Drug Deliv. 12 (2) (2015) 297–318.

[80] P. Samaddar, A. Deep, K.-H. Kim, An engineering insight into block copolymer self-assembly: Contemporary application from biomedical research to nanotechnology, Chemical Engineering Journal. 342 (2018) 71–89.

[81] A.S. Mikhail, C. Allen, Block copolymer micelles for delivery of cancer therapy: Transport at the whole body, tissue and cellular levels, Journal of Controlled Release. 138 (3) (2009) 214–223.

[82] S. Movassaghian, O.M. Merkel, V.P. Torchilin, Applications of polymer micelles for imaging and drug delivery, Wiley Interdiscip Rev Nanomed Nanobiotechnol. 7 (5) (2015) 691–707.

[83] J. Yu, H. Qiu, S. Yin, H. Wang, Y. Li, Polymeric Drug Delivery System Based on Pluronics for Cancer Treatment, Molecules. 26 (12) (2021).

[84] M. Ghezzi, S. Pescina, C. Padula, P. Santi, E. Del Favero, L. Cantu, S. Nicoli, Polymeric micelles in drug delivery: An insight of the techniques for their characterization and assessment in biorelevant conditions, J Control Release. 332 (2021) 312–336.

[85] A. Mittal, D. Chitkara, Structural modifications in polymeric micelles to impart multifunctionality for improved drug delivery, Therapeutic delivery. 7 (2) (2016) 73–87.

[86] K.K. Gill, A. Kaddoumi, S. Nazzal, PEG-lipid micelles as drug carriers: physiochemical attributes, formulation principles and biological implication, J Drug Target. 23 (3) (2015) 222–231.

[87] V. Torchilin, Lipid-Core Micelles for Targeted Drug Delivery, Current Drug Delivery. 2 (2005) 319–327.

[88] M. Amin, W. Huang, A.L.B. Seynhaeve, T.L.M. Ten Hagen, Hyperthermia and Temperature-Sensitive Nanomaterials for Spatiotemporal Drug Delivery to Solid Tumors, Pharmaceutics. 12 (11) (2020).

[89] N. Monteiro, A. Martins, R.L. Reis, N.M. Neves, Liposomes in tissue engineering and regenerative medicine, J R Soc Interface. 11 (101) (2014) 20140459.

[90] F. Bayat, R. Hosseinpour-Moghadam, F. Mehryab, Y. Fatahi, N. Shakeri, R. Dinarvand, T.L.M. Ten Hagen, A. Haeri, Potential application of liposomal nanodevices for non-cancer diseases: an update on design, characterization and biopharmaceutical evaluation, Advances in Colloid and Interface Science. 277 (2020).

[91] Y. Barenholz, Doxil(R)–the first FDA-approved nano-drug: lessons learned, J Control Release. 160 (2) (2012) 117–134.

[92] G.R. Anyarambhatla, D. Needham, Enhancement of the Phase Transition Permeability of DPPC Liposomes by Incorporation of MPPC: A New Temperature-Sensitive Liposome for use with Mild Hyperthermia, Journal of Liposome Research. 9 (4) (1999) 491–506.

[93] G. Kong, G. Anyarambhatla, W.P. Petros, R.D. Braun, O.M. Colvin, D. Needham, M.W. Dewhirst, Efficacy of liposomes and hyperthermia in a human tumor xenograft model: importance of triggered drug release, Cancer Research. 60 (24) (2000) 6950–6957.

[94] L.H. Lindner, M.E. Eichhorn, H. Eibl, N. Teichert, M. Schmitt-Sody, R.D. Issels, M. Dellian, Novel Temperature-Sensitive Liposomes with Prolonged Circulation Time, Clinical Cancer Research. 10 (6) (2004) 2168–2178.

[95] R. Mohammapdour, H. Ghandehari, Mechanisms of immune response to inorganic nanoparticles and their degradation products, Adv Drug Deliv Rev. 180 (2022).

[96] D. Chen, C.A. Dougherty, K. Zhu, H. Hong, Theranostic applications of carbon nanomaterials in cancer: Focus on imaging and cargo delivery, J Control Release. 210 (2015) 230–245.

[97] Q. Jiang, L. Liu, Q. Li, Y. Cao, D. Chen, Q. Du, X. Yang, D. Huang, R. Pei, X. Chen, et al., NIR-laser-triggered gadolinium-doped carbon dots for magnetic resonance imaging, drug delivery and combined photothermal chemotherapy for triple negative breast cancer, J Nanobiotechnology. 19 (1) (2021) 64.

[98] A.R. Bagheri, N. Aramesh, M. Bilal, J. Xiao, H.-W. Kim, B. Yan, Carbon nanomaterials as emerging nanotherapeutic platforms to tackle the rising tide of cancer – A review, Bioorganic & Medicinal Chemistry. 51 (2021).

[99] S. Lijima, T. Ichihashi, Y. Ando, Pentagons, heptagons and negative curvature in graphite microtubule growth, Nature. 776–8 (1992).

[100] S. Senapati, A.K. Mahanta, S. Kumar, P. Maiti, Controlled drug delivery vehicles for cancer treatment and their performance, Signal Transduct Target Ther. 3 (2018) 7.

[101] S. Dhanasekaran, S. Chopra, Getting a Handle on Smart Drug Delivery Systems – A Comprehensive View of Therapeutic Targeting Strategies. Smart Drug Delivery, System (2016) 31–62.

[102] H. Zare, S. Ahmadi, A. Ghasemi, M. Ghanbari, N. Rabiee, M. Bagherzadeh, M. Karimi, T.J. Webster, M.R. Hamblin, E. Mostafavi, Carbon Nanotubes: Smart Drug/Gene Delivery Carriers, Int J Nanomedicine. 16 (2021) 1681–1706.

[103] R. Chadar, O. Afzal, S.M. Alqahtani, P. Kesharwani, Carbon nanotubes as an emerging nanocarrier for the delivery of doxorubicin for improved chemotherapy, Colloids Surf B Biointerfaces. 208 (2021).

[104] L. Tang, Q. Xiao, Y. Mei, S. He, Z. Zhang, R. Wang, W. Wang, Insights on functionalized carbon nanotubes for cancer theranostics, J Nanobiotechnology. 19 (1) (2021) 423.

[105] G. Hong, S. Diao, A.L. Antaris, H. Dai, Carbon Nanomaterials for Biological Imaging and Nanomedicinal Therapy, Chem Rev. 115 (19) (2015) 10816–10906.

[106] H.K. Moon, S.H. Lee, H.C. Choi, In Vivo Near-Infrared Mediated Tumor Destruction by Photothermal Effect of Carbon Nanotubes, ACS Nano. 3 (11) (2009) 3707–3713.

[107] X. Yuan, X. Zhang, L. Sun, Y. Wei, X. Wei, Cellular Toxicity and Immunological Effects of Carbon-based Nanomaterials, Part Fibre Toxicol. 16 (1) (2019) 18.

[108] N. Kobayashi, H. Izumi, Y. Morimoto, Review of toxicity studies of carbon nanotubes, J Occup Health. 59 (5) (2017) 394–407.

[109] A. De la Zerda, C. Zavaleta, S. Keren, S. Vaithilingam, S. Bodapati, Z. Liu, J. Levi, B.R. Smith, T.J. Ma, O. Oralkan, et al., Carbon nanotubes as photoacoustic molecular imaging agents in living mice, Nat Nanotechnol. 3 (9) (2008) 557–562.

[110] D. Zhi, T. Yang, J. Yang, S. Fu, S. Zhang, Targeting strategies for superparamagnetic iron oxide nanoparticles in cancer therapy, Acta Biomater. 102 (2020) 13–34.

[111] Y. Guo, X.Y. Wang, Y.L. Chen, F.Q. Liu, M.X. Tan, M. Ao, J.H. Yu, H.T. Ran, Z.X. Wang, A light-controllable specific drug delivery nanoplatform for targeted bimodal imaging-guided photothermal/chemo synergistic cancer therapy, Acta Biomater. 80 (2018) 308–326.

[112] M. Talelli, C.J. Rijcken, T. Lammers, P.R. Seevinck, G. Storm, C.F. van Nostrum, W.E. Hennink, Superparamagnetic Iron Oxide Nanoparticles Encapsulated in Biodegradable Thermosensitive Polymeric Micelles: Toward a Targeted Nanomedicine Suitable for Image-Guided Drug Delivery, Langmuir. 25 (4) (2009) 2060–2067.

[113] A. Luchini, R.K. Heenan, L. Paduano, G. Vitiello, Functionalized SPIONs: the surfactant nature modulates the self-assembly and cluster formation, Phys Chem Chem Phys. 18 (27) (2016) 18441–18449.

[114] Fang C, Veiseh O, Kievit F, Bhattarai N, Wang F, Stephen ZL, C., Lee D, Ellenbogen RG, Zhang M. Functionalization of iron oxide magnetic nanoparticles with targeting ligands: their physicochemical properties and in vivo behavior. Nanomedicine. 2010;5(9):1357-69.

[115] D. Bonvin, J.A.M. Bastiaansen, M. Stuber, H. Hofmann, E.M. Mionic, Folic acid on iron oxide nanoparticles: platform with high potential for simultaneous targeting, MRI detection and hyperthermia treatment of lymph node metastases of prostate cancer, Dalton Trans. 46 (37) (2017) 12692–12704.

[116] Y. Yu, B. Sun, Superparamagnetic iron oxide nanoparticle 'theranostics' for multimodality tumor imaging, gene delivery, targeted drug and prodrug delivery, Expert Rev Clin Pharmacol. 3 (1) (2010) 117–130.

[117] H.C. Huang, S. Barua, G. Sharma, S.K. Dey, K. Rege, Inorganic nanoparticles for cancer imaging and therapy, J Control Release. 155 (3) (2011) 344–357.

[118] S.J. Amina, B. Guo, A Review on the Synthesis and Functionalization of Gold Nanoparticles as a Drug Delivery Vehicle, Int J Nanomedicine. 15 (2020) 9823–9857.

[119] J.C. Bischof, K.R. Diller, From Nanowarming to Thermoregulation: New Multiscale Applications of Bioheat Transfer, Annu Rev Biomed Eng. 20 (2018) 301–327.

[120] A. Kumar, X.J. Liang, Gold nanomaterials as prospective metal-based delivery systems for cancer treatment, in: R.H. Kretsinger, V.N. Uversky, E.A. Permyakov (Eds.), Encyclopedia of Metalloproteins, Springer Science +Business Media New York, New York, NY, 2013.

[121] M.I. Priester, S. Curto, G.C. van Rhoon, T.L.M. ten Hagen, External Basic Hyperthermia Devices for Preclinical Studies in Small Animals, Cancers. 13 (18) (2021) 4628.

[122] F. Wang, C. Li, J. Cheng, Z. Yuan, Recent Advances on Inorganic Nanoparticle-Based Cancer Therapeutic Agents, Int J Environ Res Public Health. 13 (12) (2016).

[123] C. Moore, J.V. Jokerst, Strategies for Image-Guided Therapy, Surgery, and Drug Delivery Using Photoacoustic Imaging, Theranostics. 9 (6) (2019) 1550–1571.

[124] R. Narayan, U.Y. Nayak, A.M. Raichur, S. Garg, Mesoporous Silica Nanoparticles: A Comprehensive Review on Synthesis and Recent Advances, Pharmaceutics. 10 (3) (2018).

[125] D.H. Everett, IUPAC Manual of Symbols and Terminology for Physicochemical Quantities and Units, Appendix II: Definitions, Terminology and Symbols in Colloid and Surface Chemistry, Pure and Applied Chemistry. 31 (4) (1972) 577–638.

[126] R. Huang, Y.W. Shen, Y.Y. Guan, Y.X. Jiang, Y. Wu, K. Rahman, L.J. Zhang, H.J. Liu, X. Luan, Mesoporous silica nanoparticles: facile surface functionalization and versatile biomedical applications in oncology, Acta Biomater. 116 (2020) 1–15.

[127] M. Wu, W. Chen, Y. Chen, H. Zhang, C. Liu, Z. Deng, Z. Sheng, J. Chen, X. Liu, F. Yan, et al., Focused Ultrasound-Augmented Delivery of Biodegradable Multifunctional Nanoplatforms for Imaging-Guided Brain Tumor Treatment, Adv Sci (Weinh). 5 (4) (2018) 1700474.

[128] T.T.H. Thi, V.D. Cao, T.N.Q. Nguyen, D.T. Hoang, V.C. Ngo, D.H. Nguyen, Functionalized mesoporous silica nanoparticles and biomedical applications, Mater Sci Eng C Mater Biol Appl. 99 (2019) 631–656.

[129] J.P.M. Almeida, A.L. Chen, Foster AD, R, In vivo biodistribution of nanoparticles. Nanomedicine. 6 (5) (2011) 815–835.

[130] A. Fernandez-Fernandez, R. Manchanda, A.J. McGoron, Theranostic applications of nanomaterials in cancer: drug delivery, image-guided therapy, and multifunctional platforms, Appl Biochem Biotechnol. 165 (7–8) (2011) 1628–1651.

[131] S. Jiang, K.Y. Win, S. Liu, C.P. Teng, Y. Zheng, M.Y. Han, Surface-functionalized nanoparticles for biosensing and imaging-guided therapeutics, Nanoscale. 5 (8) (2013) 3127–3148.

[132] D. Vasudevan, R.R. Gaddam, A. Trinchi, I. Cole, Core–shell quantum dots: Properties and applications, Journal of Alloys and Compounds. 636 (2015) 395–404.

[133] L. Tang, J. Li, T. Pan, Y. Yin, Y. Mei, Q. Xiao, R. Wang, Z. Yan, W. Wang, Versatile carbon nanoplatforms for cancer treatment and diagnosis: strategies, applications and future perspectives, Theranostics. 12 (5) (2022) 2290–2321.

[134] A.M. Wagner, J.M. Knipe, G. Orive, N.A. Peppas, Quantum dots in biomedical applications, Acta Biomater. 94 (2019) 44–63.

[135] X. Gao, Y. Cui, R.M. Levenson, L.W. Chung, S. Nie, In vivo cancer targeting and imaging with semiconductor quantum dots, Nat Biotechnol. 22 (8) (2004) 969–976.

[136] R. Mohammadi, H. Naderi-Manesh, L. Farzin, Z. Vaezi, N. Ayarri, L. Samandari, M. Shamsipur, Fluorescence sensing and imaging with carbon-based quantum dots for early diagnosis of cancer: A review, J Pharm Biomed Anal. 212 (2022).

[137] X. Xu, R. Ray, Y. Gu, H.J. Ploehn, L. Gearheart, K. Raker, W.A. Scrivens, Electrophoretic analysis and purification of fluorescent single-walled carbon nanotube fragments, Journal of the American Chemical Society. 126 (40) (2004) 12736–12797.

[138] N. Tejwan, A.K. Saini, A. Sharma, T.A. Singh, N. Kumar, J. Das, Metal-doped and hybrid carbon dots: A comprehensive review on their synthesis and biomedical applications, J Control Release. 330 (2021) 132–150.

[139] A. Nair, J.T. Haponiuk, S. Thomas, S. Gopi, Natural carbon-based quantum dots and their applications in drug delivery: A review, Biomed Pharmacother. 132 (2020).

[140] H. Mattoussi, G. Palui, H.B. Na, Luminescent quantum dots as platforms for probing in vitro and in vivo biological processes, Adv Drug Deliv Rev. 64 (2) (2012) 138–166.

[141] X. Fang, K.H. Lui, S. Li, W.S. Lo, X. Li, Y. Gu, W.T. Wong, Multifunctional Nanotheranostic Gold Nanocage/Selenium Core-Shell for PAI-Guided Chemo-Photothermal Synergistic Therapy in vivo, Int J Nanomedicine. 15 (2020) 10271–10284.

[142] D. Calle, P. Ballesteros, S. Cerdan, Advanced Contrast Agents for Multimodal Biomedical Imaging Based on Nanotechnology, Methods Mol Biol. 1718 (2018) 441–457.

[143] A. Walter, P. Paul-Gilloteaux, B. Plochberger, L. Sefc, P. Verkade, J.G. Mannheim, P. Slezak, A. Unterhuber, M. Marchetti-Deschmann, M. Ogris, et al., Correlated Multimodal Imaging in Life Sciences: Expanding the Biomedical Horizon. Frontiers, Physics. (2020) 8.

[144] N. Alsawaftah, A. Farooq, S. Dhou, A.F. Majdalawieh, Bioluminescence Imaging Applications in Cancer: A Comprehensive Review, IEEE Rev Biomed Eng. 14 (2021) 307–326.

[145] H. Wang, X. Chen, Applications for site-directed molecular imaging agents coupled with drug delivery potential, Expert Opin Drug Deliv. 6 (7) (2009) 745–768.

[146] E. Ruggiero, S. Alonso-de Castro, A. Habtemariam, L. Salassa, Upconverting nanoparticles for the near infrared photoactivation of transition metal complexes: new opportunities and challenges in medicinal inorganic photochemistry, Dalton Trans. 45 (33) (2016) 13012–13020.

[147] C. Ash, M. Dubec, K. Donne, T. Bashford, Effect of wavelength and beam width on penetration in light-tissue interaction using computational methods, Lasers Med Sci. 32 (8) (2017) 1909–1918.

[148] J. Xia, C. Kim, J.F. Lovell, Opportunities for Photoacoustic-Guided Drug Delivery, Curr Drug Targets. 16 (6) (2015) 571–581.

[149] N.S. Awad, V. Paul, N.M. AlSawaftah, G. Ter Haar, T.M. Allen, W.G. Pitt, G.A. Husseini, Ultrasound-Responsive Nanocarriers in Cancer Treatment: A Review, ACS Pharmacol Transl Sci. 4 (2) (2021) 589–612.

[150] S.E. Ahmed, A.M. Martins, G.A. Husseini, The use of ultrasound to release chemotherapeutic drugs from micelles and liposomes, J Drug Target. 23 (1) (2015) 16–42.

[151] L. Li, Y. Guan, H. Xiong, T. Deng, Q. Ji, Z. Xu, Y. Kang, J. Pang, Fundamentals and applications of nanoparticles for ultrasound-based imaging and therapy, Nano Select. 1 (3) (2020) 263–284.

[152] A.S. Mikhail, A. Partanen, P. Yarmolenko, A.M. Venkatesan, B.J. Wood, Magnetic Resonance-Guided Drug Delivery, Magn Reson Imaging Clin N Am. 23 (4) (2015) 643–655.

[153] B. Brito, T.W. Price, J. Gallo, M. Banobre-Lopez, G.J. Stasiuk, Smart magnetic resonance imaging-based theranostics for cancer, Theranostics. 11 (18) (2021) 8706–8737.

[154] S. Mastrogiacomo, W. Dou, J.A. Jansen, X.F. Walboomers, Magnetic Resonance Imaging of Hard Tissues and Hard Tissue Engineered Bio-substitutes, Mol Imaging Biol. 21 (6) (2019) 1003–1019.

[155] M. Markl, J. Leupold, Gradient echo imaging, J Magn Reson Imaging. 35 (6) (2012) 1274–1289.

[156] P.C.M. van Zijl, K. Brindle, H. Lu, P.B. Barker, R. Edden, N. Yadav, L. Knutsson, Hyperpolarized MRI, functional MRI, MR spectroscopy and CEST to provide metabolic information in vivo, Curr Opin Chem Biol. 63 (2021) 209–218.

[157] M. Dunne, M. Regenold, C. Allen, Hyperthermia can alter tumor physiology and improve chemo- and radio-therapy efficacy, Adv Drug Deliv Rev. 163–164 (2020) 98–124.

[158] Z. Bober, D. Bartusik-Aebisher, D. Aebisher, Application of Dendrimers in Anticancer Diagnostics and Therapy, Molecules. 27 (10) (2022).

[159] J. Cao, R. Ge, M. Zhang, J. Xia, S. Han, W. Lu, Y. Liang, T. Zhang, Y. Sun, A triple modality BSA-coated dendritic nanoplatform for NIR imaging, enhanced

tumor penetration and anticancer therapy, Nanoscale. 10 (19) (2018) 9021–9037.

[160] O. Taratula, C. Schumann, M.A. Naleway, A.J. Pang, K.J. Chon, O. Taratula, A multifunctional theranostic platform based on phthalocyanine-loaded dendrimer for image-guided drug delivery and photodynamic therapy, Mol Pharm. 10 (10) (2013) 3946–3958.

[161] M.T. McMahon, J.W.M. Bulte, Two decades of dendrimers as versatile MRI agents: a tale with and without metals, Wiley Interdiscip Rev Nanomed Nanobiotechnol. 10 (3) (2018) e1496.

[162] S.L. Mekuria, T.A. Debele, H.C. Tsai, Encapsulation of Gadolinium Oxide Nanoparticle (Gd2O3) Contrasting Agents in PAMAM Dendrimer Templates for Enhanced Magnetic Resonance Imaging in Vivo, ACS Appl Mater Interfaces. 9 (8) (2017) 6782–6795.

[163] P. Bevilacqua, S. Nuzzo, E. Torino, G. Condorelli, M. Salvatore, A.M. Grimaldi, Antifouling Strategies of Nanoparticles for Diagnostic and Therapeutic Application: A Systematic Review of the Literature, Nanomaterials (Basel) 11 (3) (2021).

[164] C. Lubich, P. Allacher, M. de la Rosa, A. Bauer, T. Prenninger, F.M. Horling, J. Siekmann, J. Oldenburg, F. Scheiflinger, B.M. Reipert, The Mystery of Antibodies Against Polyethylene Glycol (PEG) - What do we Know?, Pharm Res 33 (9) (2016) 2239–2249.

[165] V. Lloveras, J. Vidal-Gancedo, Polyphosphorhydrazone-Based Radical Dendrimers, Molecules. 26 (2021) 5.

[166] S. Zhang, V. Lloveras, S. Lope-Piedrafita, P. Calero-Perez, S. Wu, A.P. Candiota, J. Vidal-Gancedo, Metal-Free Radical Dendrimers as MRI Contrast Agents for Glioblastoma Diagnosis: Ex Vivo and In Vivo Approaches, Biomacromolecules (2022).

[167] Kobayashi H, Reijnders K, English S, Yordanov AT, Milenic DE, Sowers ALC, D., Krishna MC, Waldmann TA, Mitchell JB, Brechbiel MW. Application of a Macromolecular Contrast Agent for Detection of Alterations of Tumor Vessel Permeability Induced by Radiation. Clin Cancer Res. 2004;10:7712-20.

[168] M. Filippi, V. Catanzaro, D. Patrucco, M. Botta, L. Tei, E. Terreno, First in vivo MRI study on theranostic dendrimersomes, J Control Release. 248 (2017) 45–52.

[169] C. Song, Z. Ouyang, H. Guo, J. Qu, Y. Gao, J. Xia, M. Shen, X. Shi, Core-Shell Tecto Dendrimers Enable Enhanced Tumor MR Imaging through an Amplified EPR Effect, Biomacromolecules. 22 (5) (2021) 2181–2188.

[170] R. Liu, H. Guo, Z. Ouyang, Y. Fan, X. Cao, J. Xia, X. Shi, R. Guo, Multifunctional Core-Shell Tecto Dendrimers Incorporated with Gold Nanoparticles for Targeted Dual Mode CT/MR Imaging of Tumors, ACS Appl Bio Mater. 4 (2) (2021) 1803–1812.

[171] Z. Yang, R. Cheng, C. Zhao, N. Sun, H. Luo, Y. Chen, Z. Liu, X. Li, J. Liu, Z. Tian, Thermo- and pH-dual responsive polymeric micelles with upper critical solution temperature behavior for photoacoustic imaging-guided synergistic chemo-photothermal therapy against subcutaneous and metastatic breast tumors, Theranostics. 8 (15) (2018) 4097–4115.

[172] E. Boedtkjer, S.F. Pedersen, The Acidic Tumor Microenvironment as a Driver of Cancer, Annu Rev Physiol. 82 (2020) 103–126.

[173] K. Cherukula, S. Uthaman, I.K. Park, "Navigate-dock-activate" anti-tumor strategy: Tumor micromilieu charge-switchable, hierarchically activated nanoplatform with ultrarapid tumor-tropic accumulation for trackable photothermal/chemotherapy, Theranostics. 9 (9) (2019) 2505–2525.

[174] J. Zhang, Z. Qiao, H.Y. Liu, J. Song, J. Yin, Positively charged helical chain-modified stimuli-responsive nanoassembly capable of targeted drug delivery and photoacoustic imaging-guided chemo-photothermal synergistic therapy, Biomater Sci. 7 (5) (2019) 2050–2060.

[175] C. Wang, H. Hong, M. Chen, Z. Ding, Y. Rui, J. Qi, Z.C. Li, Z. Liu, A Cationic Micelle as In Vivo Catalyst for Tumor-Localized Cleavage Chemistry, Angew Chem Int Ed Engl. 60 (36) (2021) 19750–19758.

[176] H.V. Nguyen, A. Detappe, P. Harvey, N. Gallagher, C. Mathieu, M.P. Agius, O. Zavidij, W. Wang, Y. Jiang, A. Rajca, et al., Pro-organic radical contrast agents ("pro-ORCAs") for real-time MRI of pro-drug activation in biological systems, Polym Chem. 11 (29) (2020) 4768–4779.

[177] W. Alshaer, H. Hillaireau, E. Fattal, Aptamer-guided nanomedicines for anticancer drug delivery, Adv Drug Deliv Rev. 134 (2018) 122–137.

[178] Z. Yi, Z. Luo, N.D. Barth, X. Meng, H. Liu, W. Bu, A. All, M. Vendrell, X. Liu, In Vivo Tumor Visualization through MRI Off-On Switching of NaGdF4 -CaCO3 Nanoconjugates, Adv Mater. 31 (37) (2019) e1901851.

[179] Z. Wei, X. Lin, M. Wu, B. Zhao, R. Lin, D. Zhang, Y. Zhang, G. Liu, X. Liu, J. Liu, Core-shell NaGdF4@CaCO3 nanoparticles for enhanced magnetic resonance/ultrasonic dual-modal imaging via tumor acidic micro-enviroment triggering, Sci Rep. 7 (1) (2017) 5370.

[180] C. Wang, B. Wu, Y. Wu, X. Song, S. Zhang, Z. Liu, Camouflaging Nanoparticles with Brain Metastatic Tumor Cell Membranes: A New Strategy to Traverse Blood-Brain Barrier for Imaging and Therapy of Brain Tumors, Advanced Functional Materials. 30 (14) (2020).

[181] G. Gregoriadis, B.E. Ryman, Liposomes as Carriers of Enzymes or Drugs: a New Approach to the Treatment of Storage Diseases, Biochem J. 124 (5) (1971) 58.

[182] L. Sercombe, T. Veerati, F. Moheimani, S.Y. Wu, A.K. Sood, S. Hua, Advances and Challenges of Liposome Assisted Drug Delivery, Front Pharmacol. 6 (2015) 286.

[183] A.L. Seynhaeve, S. Hoving, D. Schipper, C.E. Vermeulen, G. de Wiel-Ambagtsheer, S.T. van Tiel, A.M. Eggermont, T.L. Ten Hagen, Tumor necrosis factor alpha mediates homogeneous distribution of liposomes in murine melanoma that contributes to a better tumor response, Cancer Res. 67 (19) (2007) 9455–9462.

[184] K.M. Bennett, J. Jo, H. Cabral, R. Bakalova, I. Aoki, MR imaging techniques for nano-pathophysiology and theranostics, Adv Drug Deliv Rev. 74 (2014) 75–94.

[185] A.L. Ayyagari, X. Zhang, K.B. Ghaghada, A. Annapragada, X. Hu, R.V. Bellamkonda, Long-circulating liposomal contrast agents for magnetic resonance imaging, Magn Reson Med. 55 (5) (2006) 1023–1029.

[186] Y. Xiao, Y. Liu, S. Yang, B. Zhang, T. Wang, D. Jiang, J. Zhang, D. Yu, N. Zhang, Sorafenib and gadolinium co-loaded liposomes for drug delivery and MRI-guided HCC treatment, Colloids Surf B Biointerfaces. 141 (2016) 83–92.

[187] L. Aranda-Lara, E. Morales-Avila, M.A. Luna-Gutierrez, E. Olive-Alvarez, K. Isaac-Olive, Radiolabeled liposomes and lipoproteins as lipidic nanoparticles for imaging and therapy, Chem Phys Lipids. 230 (2020).

[188] A.L. Petersen, A.E. Hansen, A. Gabizon, T.L. Andresen, Liposome imaging agents in personalized medicine, Adv Drug Deliv Rev. 64 (13) (2012) 1417–1435.

[189] N. Lamichhane, G.K. Dewkar, G. Sundaresan, R.N. Mahon, J. Zweit, [(18)F]-Fluorinated Carboplatin and [(111)In]-Liposome for Image-Guided Drug Delivery, Int J Mol Sci. 18 (5) (2017).

[190] T. van der Geest, P. Laverman, J.M. Metselaar, G. Storm, O.C. Boerman, Radionuclide imaging of liposomal drug delivery, Expert Opin Drug Deliv. 13 (9) (2016) 1231–1242.

[191] M.B. Yatvin, Design of liposomes for enhanced local release of drugs by hyperthermia, Science. 202 (4374) (1978) 1290–1293.

[192] N. Chander, J. Morstein, J.S. Bolten, A. Shemet, P.R. Cullis, D. Trauner, D. Witzigmann, Optimized Photoactivatable Lipid Nanoparticles Enable Red Light Triggered Drug Release, Small. 17 (21) (2021) e2008198.

[193] D. Miranda, K. Carter, D. Luo, S. Shao, J. Geng, C. Li, U. Chitgupi, S.G. Turowski, N. Li, G.E. Atilla-Gokcumen, et al., Multifunctional Liposomes for Image-Guided Intratumoral Chemo-Phototherapy, Adv Healthc Mater. 6 (16) (2017).

[194] G.C. van Rhoon, M. Franckena, T.L.M. Ten Hagen, A moderate thermal dose is sufficient for effective free and TSL based thermochemotherapy, Adv Drug Deliv Rev. 163–164 (2020) 145–156.

[195] A. Motamarry, A.H. Negussie, C. Rossmann, J. Small, A.M. Wolfe, B.J. Wood, D. Haemmerich, Real-time fluorescence imaging for visualization and drug uptake prediction during drug delivery by thermosensitive liposomes, Int J Hyperthermia. 36 (1) (2019) 817–826.

[196] H.P. Kok, E.N.K. Cressman, W. Ceelen, C.L. Brace, R. Ivkov, H. Grull, G. Ter Haar, P. Wust, J. Crezee, Heating technology for malignant tumors: a review, Int J Hyperthermia. 37 (1) (2020) 711–741.

[197] N. Farr, Y.N. Wang, S. D'Andrea, F. Starr, A. Partanen, K.M. Gravelle, J.S. McCune, L.J. Risler, S.G. Whang, A. Chang, et al., Hyperthermia-enhanced targeted drug delivery using magnetic resonance-guided focussed ultrasound: a pre-clinical study in a genetic model of pancreatic cancer, Int J Hyperthermia. 34 (3) (2018) 284–291.

[198] B. Cheng, C. Bing, R.M. Staruch, S. Shaikh, M. Wodzak Staruch, D. Szczepanski, N.S. Williams, T.W. Laetsch, R. Chopra, The effect of injected dose on localized tumor accumulation and cardiac uptake of doxorubicin in a Vx2 rabbit tumor model using MR-HIFU mild hyperthermia and thermosensitive liposomes, Int J Hyperthermia. 37 (1) (2020) 1052–1059.

[199] M. Amrahli, M. Centelles, P. Cressey, M. Prusevicius, W. Gedroyc, X.Y. Xu, P.W. So, M. Wright, M. Thanou, MR-labelled liposomes and focused ultrasound for spatiotemporally controlled drug release in triple negative breast cancers in mice, Nanotheranostics. 5 (2) (2021) 125–142.

[200] M. de Smet, N.M. Hijnen, S. Langereis, A. Elevelt, E. Heijman, L. Dubois, H. Grüll, Magnetic Resonance Guided High-Intensity Focused Ultrasound Mediated Hyperthermia Improves the Intratumoral Distribution of Temperature-Sensitive Liposomal Doxorubicin, Investigative radiology. 48 (6) (2013) 395–405.

[201] C. Bura, T. Mocan, C. Grapa, L. Mocan, Carbon Nanotubes-Based Assays for Cancer Detection and Screening, Pharmaceutics. 14 (4) (2022).

[202] Z. Liu, W. Cai, L. He, N. Nakayama, K. Chen, X. Sun, X. Chen, H. Dai, In vivo biodistribution and highly efficient tumour targeting of carbon nanotubes in mice, Nat Nanotechnol. 2 (1) (2007) 47–52.

[203] K. Welsher, Z. Liu, S.P. Sherlock, J.T. Robinson, Z. Chen, D. Daranciang, H. Dai, A route to brightly fluorescent carbon nanotubes for near-infrared imaging in mice, Nat Nanotechnol. 4 (11) (2009) 773–780.

[204] K. Welsher, S.P. Sherlock, H. Dai, Deep-tissue anatomical imaging of mice using carbon nanotube fluorophores in the second near-infrared window, Proc Natl Acad Sci U S A. 108 (22) (2011) 8943–8948.

[205] J.T. Robinson, G. Hong, Y. Liang, B. Zhang, O.K. Yaghi, H. Dai, In vivo fluorescence imaging in the second near-infrared window with long circulating carbon nanotubes capable of ultrahigh tumor uptake, J Am Chem Soc. 134 (25) (2012) 10664–10669.

[206] Y. Su, Y. Hu, Y. Wang, X. Xu, Y. Yuan, Y. Li, Z. Wang, K. Chen, F. Zhang, X. Ding, et al., A precision-guided MWNT mediated reawakening the sunk synergy in RAS for anti-angiogenesis lung cancer therapy, Biomaterials. 139 (2017) 75–90.

[207] Y. Hu, R. Wang, Y. Zhou, N. Yu, Z. Chen, D. Gao, X. Shi, M. Shen, Targeted dual-mode imaging and phototherapy of tumors using ICG-loaded multifunctional MWCNTs as a versatile platform, J Mater Chem B. 6 (38) (2018) 6122–6132.

[208] A. Alipour, Z. Soran-Erdem, M. Utkur, V.K. Sharma, O. Algin, E.U. Saritas, H.V. Demir, A new class of cubic SPIONs as a dual-mode T1 and T2 contrast agent for MRI, Magn Reson Imaging. 49 (2018) 16–24.

[209] N. Nelson, J. Port, M. Pandey, Use of Superparamagnetic Iron Oxide Nanoparticles (SPIONs) via Multiple Imaging Modalities and Modifications to Reduce Cytotoxicity: An Educational Review, Journal of Nanotheranostics. 1 (1) (2020) 105–135.
[210] C. Wang, H. Xu, C. Liang, Y. Liu, Z. Li, G. Yang, L. Cheng, Y. Li, Z. Liu, Iron oxide @ polypyrrole nanoparticles as a multifunctional drug carrier for remotely controlled cancer therapy with synergistic antitumor effect, ACS nano. 7 (8) (2013) 6782–6795.
[211] X.C. Zheng, W. Ren, S. Zhang, T. Zhong, X.C. Duan, Y.F. Yin, M.Q. Xu, Y.L. Hao, Z. T. Li, H. Li, et al., The theranostic efficiency of tumor-specific, pH-responsive, peptide-modified, liposome-containing paclitaxel and superparamagnetic iron oxide nanoparticles, Int J Nanomedicine. 13 (2018) 1495–1504.
[212] J. Wang, P. Chen, Y. Dong, H. Xie, Y. Wang, F. Soto, P. Ma, X. Feng, W. Du, B.F. Liu, Designer exosomes enabling tumor targeted efficient chemo/gene/photothermal therapy, Biomaterials. 276 (2021).
[213] K. Pathak, A. Vaidya, Avidin-based nanoparticles for drug delivery. Applications of Nanocomposite Materials, Drug Delivery (2018) 163–190.
[214] H. Wei, O.T. Bruns, M.G. Kaul, E.C. Hansen, M. Barch, A. Wisniowska, O. Chen, Y. Chen, N. Li, S. Okada, et al., Exceedingly small iron oxide nanoparticles as positive MRI contrast agents, Proc Natl Acad Sci U S A. 114 (9) (2017) 2325–2330.
[215] D. Ma, J. Chen, Y. Luo, H. Wang, X. Shi, Zwitterion-coated ultrasmall iron oxide nanoparticles for enhanced T1-weighted magnetic resonance imaging applications, J Mater Chem B. 5 (35) (2017) 7267–7273.
[216] M.Z. Thin, H. Allan, R. Bofinger, T.D. Kostelec, S. Guillaume, J.J. Connell, P.S. Patrick, H.C. Hailes, A.B. Tabor, M.F. Lythgoe, et al., Multi-modal imaging probe for assessing the efficiency of stem cell delivery to orthotopic breast tumours, Nanoscale. 12 (31) (2020) 16570–16585.
[217] P. Xu, R. Wang, W. Yang, Y. Liu, D. He, Z. Ye, D. Chen, Y. Ding, J. Tu, Y. Shen, A DM1-doped porous gold nanoshell system for NIR accelerated redox-responsive release and triple modal imaging guided photothermal synergistic chemotherapy, J Nanobiotechnology. 19 (1) (2021) 77.
[218] N. Zhang, J. Li, R. Hou, J. Zhang, P. Wang, X. Liu, Z. Zhang, Bubble-generating nano-lipid carriers for ultrasound/CT imaging-guided efficient tumor therapy, Int J Pharm. 534 (1–2) (2017) 251–262.
[219] X. Han, Y. Xu, Y. Li, X. Zhao, Y. Zhang, H. Min, Y. Qi, G.J. Anderson, L. You, Y. Zhao, et al., An Extendable Star-Like Nanoplatform for Functional and Anatomical Imaging-Guided Photothermal Oncotherapy, ACS Nano. 13 (4) (2019) 4379–4391.
[220] W. Li, X. Chen, Gold nanoparticles for photoacoustic imaging, Nanomedicine (Lond). 10 (2) (2015) 299–320.
[221] B. Liu, G. Qiao, Y. Han, E. Shen, G. Alfranca, H. Tan, L. Wang, S. Pan, L. Ma, W. Xiong, et al., Targeted theranostics of lung cancer: PD-L1-guided delivery of gold nanoprisms with chlorin e6 for enhanced imaging and photothermal/photodynamic therapy, Acta Biomater. 117 (2020) 361–373.
[222] B. Li, L. Sun, T. Li, Y. Zhang, X. Niu, M. Xie, Z. You, Ultra-small gold nanoparticles self-assembled by gadolinium ions for enhanced photothermal/photodynamic liver cancer therapy, J Mater Chem B. 9 (4) (2021) 1138–1150.
[223] K. Yang, Y. Liu, Y. Wang, Q. Ren, H. Guo, J.B. Matson, X. Chen, Z. Nie, Enzyme-induced in vivo assembly of gold nanoparticles for imaging-guided synergistic chemo-photothermal therapy of tumor, Biomaterials. 223 (2019).
[224] C. Yang, M. Chang, M. Yuan, F. Jiang, B. Ding, Y. Zhao, P. Dang, Z. Cheng, A.A.A. Kheraif, P. Ma, et al., NIR-Triggered Multi-Mode Antitumor Therapy Based on Bi2 Se3 /Au Heterostructure with Enhanced Efficacy, Small. 17 (28) (2021) e2100961.
[225] Z. Yang, W. Fan, J. Zou, W. Tang, L. Li, L. He, Z. Shen, Z. Wang, O. Jacobson, M.A. Aronova, et al., Precision Cancer Theranostic Platform by In Situ Polymerization in Perylene Diimide-Hybridized Hollow Mesoporous Organosilica Nanoparticles, J Am Chem Soc. 141 (37) (2019) 14687–14698.
[226] D.F. Quail, J.A. Joyce, Microenvironmental regulation of tumor progression and metastasis, Nat Med. 19 (11) (2013) 1423–1437.
[227] C. Zhang, X. Wang, J. Du, Z. Gu, Y. Zhao, Reactive Oxygen Species-Regulating Strategies Based on Nanomaterials for Disease Treatment, Adv Sci (Weinh). 8 (3) (2021) 2002797.
[228] J. Van Loenhout, M. Peeters, A. Bogaerts, E. Smits, C. Deben, Oxidative Stress-Inducing Anticancer Therapies: Taking a Closer Look at Their Immunomodulating Effects, Antioxidants (Basel) 9 (12) (2020).
[229] N.V. Rao, H.S. Han, H. Lee, V.Q. Nguyen, S. Jeon, D.W. Jung, J. Lee, G.R. Yi, J.H. Park, ROS-responsive mesoporous silica nanoparticles for MR imaging-guided photodynamically maneuvered chemotherapy, Nanoscale. 10 (20) (2018) 9616–9627.
[230] Y. Feng, X. Xie, H. Zhang, Q. Su, G. Yang, X. Wei, N. Li, T. Li, X. Qin, S. Li, et al., Multistage-responsive nanovehicle to improve tumor penetration for dual-modality imaging-guided photodynamic-immunotherapy, Biomaterials. 275 (2021).
[231] W. Lin, M. Chen, L. Hong, H. Zhao, Q. Chen, Crosstalk Between PD-1/PD-L1 Blockade and Its Combinatorial Therapies in Tumor Immune Microenvironment: A Focus on HNSCC, Front Oncol. 8 (2018) 532.
[232] B.R. Smith, Z. Cheng, A. De, J. Rosenberg, S.S. Gambhir, Dynamic visualization of RGD-quantum dot binding to tumor neovasculature and extravasation in multiple living mouse models using intravital microscopy, Small. 6 (20) (2010) 2222–2229.
[233] H.M. Gil, T.W. Price, K. Chelani, J.G. Bouillard, S.D.J. Calaminus, G.J. Stasiuk, NIR-quantum dots in biomedical imaging and their future, iScience. 24 (3) (2021).
[234] C. Li, Y. Zhang, M. Wang, Y. Zhang, G. Chen, L. Li, D. Wu, Q. Wang, In vivo real-time visualization of tissue blood flow and angiogenesis using Ag2S quantum dots in the NIR-II window, Biomaterials. 35 (1) (2014) 393–400.
[235] L.D. Chen, J. Liu, X.F. Yu, M. He, X.F. Pei, Z.Y. Tang, Q.Q. Wang, D.W. Pang, Y. Li, The biocompatibility of quantum dot probes used for the targeted imaging of hepatocellular carcinoma metastasis, Biomaterials. 29 (31) (2008) 4170–4176.
[236] R. Savla, O. Taratula, O. Garbuzenko, T. Minko, Tumor targeted quantum dot-mucin 1 aptamer-doxorubicin conjugate for imaging and treatment of cancer, J Control Release. 153 (1) (2011) 16–22.
[237] M. Sun, G. Sundaresan, P. Jose, L. Yang, D. Hoffman, N. Lamichhane, J. Zweit, Highly stable intrinsically radiolabeled indium-111 quantum dots with multidentate zwitterionic surface coating: dual modality tool for biological imaging, J Mater Chem B. 2 (28) (2014) 4456–4466.
[238] L.D. Olerile, Y. Liu, B. Zhang, T. Wang, S. Mu, J. Zhang, L. Selotlegeng, N. Zhang, Near-infrared mediated quantum dots and paclitaxel co-loaded nanostructured lipid carriers for cancer theragnostic, Colloids Surf B Biointerfaces. 150 (2017) 121–130.
[239] X.W. Hua, Y.W. Bao, J. Zeng, F.G. Wu, Ultrasmall All-In-One Nanodots Formed via Carbon Dot-Mediated and Albumin-Based Synthesis: Multimodal Imaging-Guided and Mild Laser-Enhanced Cancer Therapy, ACS Appl Mater Interfaces. 10 (49) (2018) 42077–42087.
[240] T. Luo, Y. Nie, J. Lu, Q. Bi, Z. Cai, X. Song, H. Ai, R. Jin, Iron doped carbon dots based nanohybrids as a tetramodal imaging agent for gene delivery promotion and photothermal-chemodynamic cancer synergistic theranostics, Materials & Design. 208 (2021).
[241] X. Zhang, Q. Fu, H. Duan, J. Song, H. Yang, Janus Nanoparticles: From Fabrication to (Bio)Applications, ACS Nano. 15 (4) (2021) 6147–6191.
[242] X. Chen, X. Zhang, L. Zhang, Y. Gao, C. Wang, W. Hong, G. Zhao, L. Li, R. Liu, C. Wang, Amphiphilic Janus nanoparticles for imaging-guided synergistic chemo-photothermal hepatocellular carcinoma therapy in the second near-infrared window, Nanoscale. 13 (7) (2021) 3974–3982.
[243] L. Zhang, M. Zhang, L. Zhou, Q. Han, X. Chen, S. Li, L. Li, Z. Su, C. Wang, Dual drug delivery and sequential release by amphiphilic Janus nanoparticles for liver cancer theranostics, Biomaterials. 181 (2018) 113–125.
[244] Cavallo-Medved D, Moin K, Sloane B. Cathepsin B. AFCS Nat Mol Pages. 2011.
[245] M. Zhou, S. Liu, Y. Jiang, H. Ma, M. Shi, Q. Wang, W. Zhong, W. Liao, M.M.Q. Xing, Doxorubicin-Loaded Single Wall Nanotube Thermo-Sensitive Hydrogel for Gastric Cancer Chemo-Photothermal Therapy, Advanced Functional Materials. 25 (29) (2015) 4730–4739.
[246] M. Chaudhry, P. Lyon, C. Coussios, R. Carlisle, Thermosensitive liposomes: a promising step toward localised chemotherapy, Expert Opin Drug Deliv. 19 (8) (2022) 899–912.
[247] M.J. Mitchell, M.M. Billingsley, R.M. Haley, M.E. Wechsler, N.A. Peppas, R. Langer, Engineering precision nanoparticles for drug delivery, Nat Rev Drug Discov. 20 (2) (2021) 101–124.
[248] H. Maeda, M. Khatami, Analyses of repeated failures in cancer therapy for solid tumors: poor tumor-selective drug delivery, low therapeutic efficacy and unsustainable costs, Clin Transl Med. 7 (1) (2018) 11.
[249] A. Gabizon, R. Catane, B. Uziely, B. Kaufman, T. Safra, R. Cohen, F. Martin, A. Huang, Y. Barenholz, Prolonged circulation time and enhanced accumulation in malignant exudates of doxorubicin encapsulated in polyethylene-glycol coated liposomes, Cancer research. 54 (4) (1994) 987–992.
[250] A.L.B. Seynhaeve, B.M. Dicheva, S. Hoving, G.A. Koning, T.L.M. Ten Hagen, Intact Doxil is taken up intracellularly and released doxorubicin sequesters in the lysosome: evaluated by in vitro/in vivo live cell imaging, J Control Release. 172 (1) (2013) 330–340.
[251] D. Liu, F. Yang, F. Xiong, N. Gu, The Smart Drug Delivery System and Its Clinical Potential, Theranostics. 6 (9) (2016) 1306–1323.
[252] Hobbs SK, Monsky WL, Yuan F, Roberts WG, Griffith L, Torchilin VP, Jain RK. Regulation of transport pathways in tumor vessels: role of tumor type and microenvironment. Proceedings of the National Academy of Sciences. 1998;95(8):4607-12.
[253] S. Wilhelm, A.J. Tavares, Q. Dai, S. Ohta, J. Audet, H.F. Dvorak, W.C. Chan, Analysis of nanoparticle delivery to tumours, Nature reviews materials. 1 (2016) 1–12.
[254] G. Kong, R.D. Braun, M.W. Dewhirst, Hyperthermia Enables Tumor-specific Nanoparticle Delivery: Effect of Particle Size, Cancer Research. 60 (16) (2000) 4440–4445.
[255] R.M. Staruch, M. Ganguly, I.F. Tannock, K. Hynynen, R. Chopra, Enhanced drug delivery in rabbit VX2 tumours using thermosensitive liposomes and MRI-controlled focused ultrasound hyperthermia, Int J Hyperthermia. 28 (8) (2012) 776–787.
[256] L. Li, T.L. ten Hagen, M. Bolkestein, A. Gasselhuber, J. Yatvin, G.C. van Rhoon, A.M. Eggermont, D. Haemmerich, G.A. Koning, Improved intratumoral nanoparticle extravasation and penetration by mild hyperthermia, J Control Release. 167 (2) (2013) 130–137.
[257] S. Wang, I.V. Larina, High-resolution imaging techniques in tissue engineering. Monitoring and Evaluation of Biomaterials and their Performance, In Vivo (2017) 151–180.

[258] E. Najafzadeh, P. Farnia, A. Ahmadian, H. Ghadiri, Light-Emitting Diode Based Photoacoustic Imaging System, Frontiers in Biomedical Technologies. 7 (3) (2020) 201–205.
[259] C.S. Betz, V. Volgger, S.M. Silverman, M. Rubinstein, M. Kraft, C. Arens, B.J.F. Wong, Clinical optical coherence tomography in head and neck oncology: overview and outlook, Head Neck Oncol. 5 (3) (2013) 35–42.
[260] G.T. van Moolenbroek, T. Patiño, J. Llop, S. Sánchez, Engineering Intelligent Nanosystems for Enhanced Medical Imaging, Advanced Intelligent Systems. 2 (10) (2020).
[261] J.B. Vines, J.H. Yoon, N.E. Ryu, D.J. Lim, H. Park, Gold Nanoparticles for Photothermal Cancer Therapy, Front Chem. 7 (2019) 167.
[262] Y. Wu, M.R.K. Ali, K. Chen, N. Fang, M.A. El-Sayed, Gold nanoparticles in biological optical imaging, Nano Today. 24 (2019) 120–140.
[263] Aaron JT, S. Fluorescence Studies of Anti-Cancer Drugs – Analytical and Biomedical Applications. Current Drug Targets. 2006;7(9):1067-81.
[264] E.Y. Park, D. Oh, S. Park, W. Kim, C. Kim, New contrast agents for photoacoustic imaging and theranostics: Recent 5-year overview on phthalocyanine/naphthalocyanine-based nanoparticles, APL Bioeng. 5 (3) (2021).
[265] P. Frinking, T. Segers, Y. Luan, F. Tranquart, Three Decades of Ultrasound Contrast Agents: A Review of the Past, Present and Future Improvements, Ultrasound Med Biol. 46 (4) (2020) 892–908.